LINKING UV OPTICAL PROPERTIES AND PHOTOCHEMICAL RATES USING REMOTELY SENSED OCEAN COLOR

by

FANG CAO

(Under the Direction of William L. Miller)

ABSTRACT

Solar ultraviolet radiation (UVR) is a critical factor regulating photo processes in the ocean with the majority of UVR absorbed by chromophoric dissolved organic matter (CDOM). Accurate knowledge of UVR and CDOM distributions is desired to better model the UV–CDOM interactions that drive photochemistry. This dissertation contains four studies that develop optical techniques to model photochemistry and fluorescent components in the ocean.

First, a composite set of remote sensing algorithms was developed to retrieve UV attenuation coefficients (K_d(UV)) from remote sensing reflectance (R_{rs}), allowing improved estimates of UVR penetration in a variety of water types (e.g. mean relative error of 13% for K_d(340)).

Second, I used a suite of statistical approaches to develop a novel algorithm (Sea*CDOM*) for accurate, direct retrieval of fully resolved UV absorption spectra for CDOM, a_g(275-450), from $R_{rs,}$ obtaining a mean relative error of ~25%. It has the advantage of being free of the assumed CDOM exponential extrapolations from modeled visible wavelengths that have hampered previous work. This advance should provide new insight about the chemical composition, origins, transformation, and cycling pathways of CDOM in the surface ocean with a synoptic view.

Third, I introduced a new approach for calculating photochemical rates by blending the composite (K_d(UV) and Sea*CDOM* algorithms to examine carbon monoxide photoproduction using a single, high resolution coastal satellite image. This novel product demonstrates the complex spatial variability of depth-specific and depth-integrated photoproduction on an estuarine scale. This new capability for independent retrievals of a_g and K_d allows quantitative partitioning of UV photons between CDOM and other optical constituents, producing greatly improved estimates for photochemistry in complex waters.

Finally, I explored the spatial (0 to ~5000m) distribution and dynamics of DOM throughout the Gulf of Alaska using absorbance and fluorescence measurements. Biogeochemical and physical processes driving DOM optical property distributions are explored using multi-linear relationships, revealing significant control by both *in situ* production and mixing of water masses. Strong relationships between dissolved organic carbon (DOC) and protein-like fluorescent components, suggests a new tool to trace bulk dissolved organic carbon in the deep ocean, especially within the bio-refractory pool.

INDEX WORDS: Remote sensing reflectances; Ocean color; Algorithms; Diffuse attenuation coefficient; Ultraviolet radiation; Inshore waters; Global scale; Chromophoric dissolved organic matter (CDOM); Photochemistry; Deep ocean; PARAFAC;

LINKING UV OPTICAL PROPERTIES AND PHOTOCHEMICAL RATES USING REMOTELY SENSED OCEAN COLOR

by

FANG CAO

B.S., Qingdao University of Science & Technology, P. R. China, 2005

M.S., Ocean University of China, P. R. China, 2008

A Dissertation Submitted to the Graduate Faculty of The University of Georgia in Partial Fulfillment of the Requirements for the Degree

DOCTOR OF PHILOSOPHY

ATHENS, GEORGIA

2015

LINKING UV OPTICAL PROPERTIES AND PHOTOCHEMICAL RATES USING REMOTELY SENSED OCEAN COLOR

by

FANG CAO

Major Professor:	William Miller
Committee:	Adrian Burd
	Chuck Hopkinson
	Deepak Mishra
	Patricia Medeiros

Electronic Version Approved:

Julie Coffield
Interim Dean of the Graduate School
The University of Georgia
May 2015

DEDICATION

To my parents

for their love and support

ACKNOWLEDGEMENTS

This dissertation work would not have been possible without support from many individuals. Most importantly, I would express my deep sense of gratitude to my major professor, Dr. William L. Miller, for his efforts in getting me in before my official beginning of the graduate school, for his endless patience and encouragement throughout these six years, and for his strong recommendation for my postdoc application. He has been a great mentor, teaching me things about and beyond science, applauding my progress, and always keeping me motivated. I have continued to benefit from his scientific vision, knowledge, and inspiration.

I would also like to extend my gratitude to my committee members: Drs. Adrian Burd, Chuck Hopkinson, Deepak Mishra, Patricia Medeiros, and John Schalles, for thoughtful comments and informative discussions on each individual project towards the final completion. I deeply appreciate their time and efforts on my dissertation work.

I am grateful to other faculty members and staff in the Marsci Department. I thank Dr. Daniela Di Iorio for her patience answering my questions, being always available when I knock the door, sharing her physical oceanography knowledge with me and helping explain the data. I thank Dr. Renato Castelao for teaching me to make my very first figure in my career dealing with remote sensing when I was a newbie. I wish to thank Drs. Brian Binder and Christof Meile for offering teaching assistantship and travel funding to me. I also thank the ladies in the front offices and Sharon for keeping everything running smoothly over the years.

I am indebted to my labmates in Miller lab, Meg and Drs. Heather and Leanne, for their companionship in the office, sharing snacks, correcting my pronunciation, hanging out in town, and helping with lab and field work. I especially thank Dr. Cedric, who has no overlap with me during grad school but has been a great co-author and an inspiration to me.

I also owe my sincere gratitude to the folks who contribute to this dissertation work. Particularly, I would like to thank Dr. Bo-Cai Gao in the Naval Research Laboratory for his generous help with correcting the raw satellite image and facilitating the completion of my thesis story. I also thank Yuntao Wang and Qian Liu for their technical help and discussions on my thesis.

Finally, I would like to thank my family in China and in the States. I thank mom and dad for bringing me up and always encouraging me to pursue my dream. I thank my husband, for his incredible devotion and patience over these years.

TABLE OF CONTENTS

Page

CHAPTER

APPENDICES

LIST OF TABLES

Page

LIST OF FIGURES

Page

CHAPTER 1

INTRODUCTION AND LITERATURE REVIEW

1.1. Background and Motivation

1.1.1. Why study photochemistry of CDOM?

Solar ultraviolet radiation (UVR, with a wavelength range of 280–400 nm), is a critical factor regulating biogeochemical cycles in the ocean (Whitehead *et al.*, 2000; Williamson *et al.*, 2014). Most of UVR in the ocean is absorbed by the optically active fraction, known as chromophoric dissolved organic matter (CDOM) within the larger pool of dissolved organic carbon, especially in coastal and estuarine waters. Upon exposure to high–energy UVR, CDOM undergoes a variety of photochemical reactions, including formation of short-lived transit radicals (e.g., $\cdot HO$, $^1O_2$, O_2^-), as well as stable non-radical species that influence the global cycling of environmentally important trace gases (e.g., carbon monoxide (CO), carbon dioxide, etc.), the redox cycling of essential trace metals (e.g., Fe, Mn, Cu), and alter biological availability of organic carbon (Blough and Del Vecchio, 2002; Mopper and Kieber, 2000; Zepp *et al.*, 2007). Photochemical breakdown of CDOM, on the other hand, controls the underwater radiation field by influencing UVR penetration depth in the water column, and in turn affects phytoplankton and microbial productivity in marine ecosystems (Kirk, 1994). Furthermore, photodegradation of CDOM provides biologically labile organic substrates, supporting heterotrophic community and subsequent microbial food webs (Moran and Zepp, 1997). Given these significant processes, accurate knowledge of CDOM photochemistry is desired to better quantify its role in the global carbon cycle.

1.1.2. How to quantify CDOM photochemistry from ocean color?

The light-absorbing properties of CDOM allow a quantitative determination of its relevant photoprocesses in the surface ocean based on satellite ocean color observations, offering a synoptic view with high spatial and temporal coverage. Rigorous assessment of depth-specific photoproduction (Ψ(z), mol (photoproducts) m^{-3} s^{-1}, z = depth) with respect to CDOM requires accurate knowledge of three variables: 1) the photon flux available for CDOM at a specific depth z, represented by scalar irradiance ($E_0(\lambda, z)$, mol (photons) m^{-2} s^{-1} nm^{-1}), 2) the fraction of photons available that is absorbed by CDOM, quantified as the CDOM absorption coefficient (a_g, m^{-1}), and 3) the efficiency with which each absorbed photon creates a photochemical reaction (product production or loss). In this dissertation, I incorporate the photochemical efficiency of CO production from CDOM, ϕ_{CO}, mol (CO) mol (photons) $^{-1}$ in the general photochemical rate expression shown in Equation (1) (Toole *et al.*, 2003)

$$\Psi_{co}(t,z) = \int_{\lambda_1}^{\lambda_2} E_0(\lambda, \mathrm{z}, \mathrm{t}) \times a_{\mathrm{g}}(\lambda) \times \phi_{\mathrm{CO}}(\lambda) \mathrm{d}\lambda \qquad (1)$$

where Ψ_{CO}(t, z)) is CO photoproduction rate at time t and depth z; λ_1 and λ_2 represent the integration limits of the photoreactive wavelengths, $E_0(\lambda, z, t)$ denotes the irradiance at wavelength λ at time *t*; $a_g(\lambda)$ and $\phi_{CO}(\lambda)$ are the CDOM absorption coefficient and CO photoproduction efficiency at wavelength λ, respectively. A short discussion of each of these three components (as they relate to remote sensing ocean color where possible) is presented in the following text.

Incident radiation in the water column and Diffuse attenuation coefficient

Solar scalar irradiance just below the water surface ($E_0(\lambda, 0^-)$) is the radiant energy available for CDOM photochemistry and represents the integration of all radiant flux at a single point incident over all directions (Kirk, 1994). In the simplified photochemical model described in Fichot and Miller (2010), $E_0(\lambda, 0^-)$ can be estimated from observations of downwelling irradiance right beneath the water surface ($E_d(\lambda, 0^-)$) by ignoring the upwelling irradiance which is minor and consequently negligible. In natural waters, the absorption and scattering of solar irradiation by seawater and optically active constituents therein (phytoplankton, CDOM, non-algal particles, and detritus) affects the underwater radiation field, which in turn impacts photochemical reactions. The most commonly used parameter to describe the loss of radiation intensity in the water column is the downwelling diffuse attenuation coefficient ($K_d(\lambda)$), defined as the fractional rate of decay of downwelling spectral irradiance ($E_d(\lambda, z)$) with depth z. $E_d(\lambda)$ diminishes in an exponential manner with physical depth and can be expressed as in Equation (2),

$$E_d(\lambda, z) = E_d(\lambda, 0^-) \times \exp(-K_d(\lambda) \times z) \quad . \qquad (2)$$

With the knowledge of $K_d(\lambda)$ and surface irradiance, $E_d(\lambda, 0^-)$, we are able to describe the downwelling irradiance $E_d(\lambda, z)$ at any desired depth z. K_d is typically measured with an optical profiling system that measures in-water downwelling irradiance continuously as it passes through the water column. K_d is subsequently calculated as shown below.

$$K_d(\lambda) = -\frac{d\, ln(E_d)}{d\, z} = -\frac{1}{E_d} \times \frac{dE_d}{dz} \qquad (3)$$

K_d not only depends on the inherent optical properties, but also varies as a function of the geometric structure of incident radiation (sun elevation, water surface and sky conditions, etc.) (Morel and Maritorena, 2001). It demonstrates great spatial variability with values ranging over three orders of magnitude from the clearest open ocean (e.g., Lee *et al.*, 2013) to very dark oligotrophic lakes (e.g., Kjeldstad *et al.*, 2003). A proven approach to estimate K_d over large spatial scales is with satellite imagery of ocean color. A common K_d wavelength reported in the literature is 490 nm (K_d(490)) which has long been used to describe water clarity (Austin and Petzold, 1981; Wang *et al.*, 2009) and has shaped standard NASA K_d(490) product (Werdell, 2009).

There have been far fewer studies on K_d(UV) retrieval from ocean color, especially in turbid estuaries and coastal oceans, probably due to technical challenges of accurately measuring UV attenuation in these waters and because the more common bio-optical research focuses on domains other than UV radiation. Johannessen *et al*. (2003) formulated an empirical linear relationship between K_d(UV) (λ=323, 338, and 380 nm) using a blue-green ratio of visible remote sensing reflectance (R_{rs}, $R_{rs}(412)/R_{rs}(555)$) to retrieve K_d(UV) from ocean color. Fichot *et al.* (2008) developed the Sea*UV*/Sea*UV*c algorithms using multivariate statistical approaches to estimate K_d in the UV and blue wavelengths directly from R_{rs}. These algorithms, developed and validated with a larger coastal and open ocean data set provided improved accuracy over a simple ratio approach of Johannessen *et al.* (2003). However, as shown later (Chapter 2) in this dissertation, when applied to optically complex inshore waters, the original Sea*UV*/Sea*UV*c algorithms severely underestimate K_d and refinements were required to retrieve accurate K_d estimates for inshore waters.

CDOM absorption of UVR

CDOM, also traditionally known as yellow substance or gelbstoff, contains the optically active fraction of the dissolved organic matter pool. CDOM absorbs light mainly in the UV and blue spectral domains and drives marine photochemistry, thereby playing an essential role in carbon biogeochemical cycling. CDOM in natural waters is an operational value defined by measuring the spectrally resolved absorption spectrum of 0.2 μm filtered water samples over UV and visible wavelengths. Absorption spectra for CDOM typically exhibit a featureless, monotonically decreasing trend with increasing wavelength. For seawater samples, the measured CDOM spectrum obtained from a spectrophotometer must be corrected for refractive index effects between salt water and pure water when the later is used as a reference. CDOM in the ocean is described by its absorption coefficient at a specific wavelength, calculated as shown in Equation (4)

$$a_g(\lambda) = \ln(10) \times A(\lambda)/L, \tag{4}$$

where $a_g(\lambda)$ (m^{-1}) is the Napierian absorption coefficient of CDOM at wavelength λ, $A(\lambda)$ (unitless) is the blank corrected CDOM absorbance at λ, and L (m) is the path length of the spectrophotometric cell.

The optical significance of CDOM allows its remote retrieval from satellite ocean color platforms. Prediction of a_g from R_{rs} via a variety of algorithms, either semi-analytical or empirical, has been routinely made in the visible regime (typically at 412 and 443 nm) and mainly restricted to the determination of a_g at individual wavelengths. Based on radiative transfer theory, semi-analytical algorithms relate the ratio between backscattering and absorption of constituents in the water to R_{rs} and simultaneously derive a suite of inherent optical properties (IOPs), including absorption by chlorophyll and colored detrital material (e.g., quantified using $a_{dg}(443)$, for more details, see Chapter 3), as well as the backscattering coefficient of particles (b_{bp}) (e.g., Garver and Siegel, 1997; Lee *et al.*, 2002; Maritorena *et al.*, 2002). Empirical algorithms have been used to statistically correlate various R_{rs} ratios to a_g at specific visible wavelengths (e.g., $a_g(412)$), obtained either from *in situ* IOP profile observations or spectrophotometric measurements (e.g., Del Castillo and Miller, 2008; Mannino *et al.*, 2008). Additionally, a_g has been estimated by relating R_{rs} to an intermediate parameter (i.e., K_d), and subsequently using this to derive a_g based on an empirical relation between K_d and a_g (Fichot and Miller, 2010; Johannessen *et al*, 2003) Satellite derived estimates of $a_{dg}(443)$ or $a_g(412)$ are in turn used to model the UV absorption of CDOM by assuming an exponential spectral slope coefficient (S, nm^{-1}) modeled as

$$a_g(\lambda) = a_g(\lambda_o) \times e^{-S(\lambda-\lambda_o)}, \tag{5}$$

where $a_g(\lambda)$ is the desired absorption coefficient (m^{-1}) of CDOM at wavelength λ, and λ_o is the reference wavelength (nm) (e.g., Bricaud *et al.*, 1981; Twardowski *et al.*, 2004). Changes of S have been reported to provide information about CDOM characteristics (sources, molecular weight, etc.) and may be used to trace changes in the CDOM pool such as photobleaching (Twardowski et al., 2004). However, the values assigned to S are largely dependent on the wavelength interval chosen for fitting, making published spectral slope coefficients variable and often contradictory (Carder et al., 1989; Twardowski et al., 2004).

To fully evaluate the critical role of UV wavelengths in CDOM photoprocesses, its full spectral absorbance in the UV is desired. However, most efforts have modeled a_g at UV wavelengths by extrapolation from visible a_g estimates either using a predefined S value (Stedmon *et al.*, 2000), or based on the functional relationship between $a_{dg}(443)$ and S (Swan *et al.*, 2013). Unfortunately, field studies have shown that S varies significantly with CDOM source material and biogeochemical processes. In this sense, current algorithms for retrieving CDOM spectra from ocean color can suffer large errors arising from the assumption of a single exponential spectral slope and its extrapolation from visible to UV wavelengths. Also, there have been few studies attempting to retrieve S from remote sensing (Carder *et al.*, 1989; Fichot *et al.*, 2013; Fichot *et al.*, 2014; Vähätalo and Wetzel, 2004), which can potentially be used as a tracer for photochemical modification of terrestrial dissolved organic carbon in river-dominated coastal margins (Fichot and Benner, 2012; Fichot *et al.*, 2013). Other studies have also shown that the ratio between S values determined over different wavelength intervals (S_R, calculated as the ratio of $S_{275-295}$ to $S_{350-400}$), is informative and may reveal additional DOM chemical characteristics. Helms *et al.* (2008) proposed S_R as a proxy for DOM molecular weight (MW), with changes indicating photochemical MW alteration of the DOC pool. Although S_R has been used to study the dynamics of DOM in samples taken from natural waters (Helms *et al.*, 2013; Stubbins *et al.*, 2012; Yamashita *et al.*, 2013), synoptic assessment of S_R has not yet been made from remote sensing.

Photoproduction efficiency

The efficiency of photochemical production for any product arising from photon absorption by CDOM is described using an apparent quantum yield (AQY), which equals the ratio of moles of desired photoproduct generated (in this dissertation, CO) and moles of photons absorbed by CDOM. The term “apparent” here accounts for the fact that the specific chromophores involved in the photochemical reactions leading to production are unknown, due to the complex nature of CDOM. Consequently, AQY is determined as a function of wavelength and the absorption coefficient of the entire CDOM pool. Determination of AQY spectra can only be done by laboratory measurements and are not directly related to ocean color.

Compared to the open ocean where CO photochemical efficiencies are relatively well constrained (Zafiriou *et al.*, 2003; Ziolkowski and Miller, 2007), AQY for CO in the coastal and inshore waters remain variable and difficult to assign (Powers and Miller, 2015). This is largely due to the complex nature of CDOM in terrestrially influenced areas and elusive mechanisms by which chromophores participate in photolysis reactions (Gao and Zepp, 1998). AQY uncertainties pose a considerable challenge when seeking a synoptic assessment of photoproduction using traditional passive satellite observations with relatively coarse spatial resolution (e.g., ~1.1 km of the Sea-Viewing Wide Field-of-View Sensor (SeaWiFS).

Modeling depth-specific photoproduction rates of CO

Knowing the three critical components for photoproduction described above, depth-specific photochemical production rates for CO generated by photons absorbed over the entire photoreactive spectrum can be modeled as shown in Equation (6)

$$\mathit{\Psi}_{\mathrm{co}}(z) = \int_{\lambda_{min}}^{\lambda_{max}} E_{0\mathrm{d}}(\lambda, 0^{-}) \times \exp(-K_{\mathrm{d}}(\lambda) \times z) \times a_{\mathrm{g}}(\lambda, z) \times \phi_{\mathrm{CO}}(\lambda, z)\mathrm{d}\lambda \qquad (6)$$

where $\mathit{\Psi}_{\mathrm{CO}}(z)$ (mol (CO) m^{-3} s^{-1}) is CO photoproduction rate at depth z (m), and λ_{min} and λ_{max} are the minimal and maximal wavelengths respectively that are considered significant in CO production. Assuming homogeneity within the photic zone for each ocean color pixel, $\mathit{\Psi}_{\mathrm{CO}}(z)$ is fundamentally a function of optical (K_{d}, a_{g}) and photochemical (ϕ_{CO}) properties, with the first two variables being retrievable from remote sensing and the latter typically modeled based on laboratory determinations of field samples. Hence, a robust retrieval of these UV optical parameters is critical to obtain accurate quantification of marine photochemical fluxes based on ocean color.

1.1.3. Fluorescent dissolved organic matter (FDOM)

The absorption of photons by CDOM not only causes photochemical reactions, but also creates photophysical processes, including fluorescence. The fraction of fluorescent DOM within the CDOM pool is referred to as “FDOM”. Similar to CDOM, FDOM in the aquatic system is a complex mixture of fluorophores that originate from various sources and are subject to various degradation and removal processes. In natural waters, FDOM can be classified into two general categories: the humic-like components (hereafter $\mathrm{FDOM_H}$) and the protein-like components (hereafter $\mathrm{FDOM_P}$). $\mathrm{FDOM_H}$ generally produces broad emission peaks at longer wavelength (>

400 nm) than $FDOM_P$ which is characterized by narrower fluorescence emission peak at wavelengths shorter than 400 nm. $FDOM_H$ is ubiquitous in aquatic environments and has long been used to trace terrestrial organic material (Coble, 1996) and describe the dynamics of DOM (Stedmon and Markager, 2005; Yamashita *et al.*, 2008), to fingerprint water masses (Walker *et al.*, 2009), and to estimate DOC fluxes from land to the ocean (Amon *et al.*, 2003). $FDOM_P$ is considered to be associated with *in situ* biological activities (Yamashita and Tanoue, 2003), and bound in protein molecular structure (Kowalczuk *et al.*, 2009). In the open ocean, $FDOM_H$ shows reduced values in the surface water, resulting from photodegradation and gradually increases with depth as "humic" material is regenerated from sinking particles and accumulates in the remineralization zone (Chen and Bada, 1992; Yamashita *et al.*, 2010). Conversely, $FDOM_P$ is found to be high in the surface ocean presumably related to biological production, and decreases with depth in the water column.

In the past 20 years, 3D scanning of fluorescence from DOM has been widely used to distinguish different sources of DOM in the ocean. Excitation-emission matrix spectra (EEMs) are generated by acquiring the complete emission spectrum at a series of successively increasing excitation wavelengths. It provides a more complete picture of the excitation and emission properties of fluorophores within the sample (terrestrial, marine, microbial, etc.), with source material distinguished based on their different excitation/emission maxima (Coble, 1996). The early application of EEMs to discriminate sources of DOM was basically a "peak-picking" technique (e.g., Coble, 1996) and since the EEMs of DOM are composed of overlapping fluorophores, it was difficult to properly assess the specific dynamics of DOM based solely on the EEMs technique (Yamashita et al., 2008).

Resolving FDOM compositions has been greatly benefited from development of statistical methods. Stedmon et al. (2003) proposed a new statistical approach (parallel factor analysis; PARAFAC) to interpret the multi-dimensional nature of the EEMs data. The PARAFAC technique statistically decomposes the complicated 3D fluorescence data matrix into a set of three linear terms and a residual array as shown in Equation (7) (Stedmon *et al.*, 2003),

$$x_{ijk} = \sum_{f=1}^{F} a_{if} b_{jf} c_{kf} + e_{ijk}, i = 1, \cdots, I; j = 1, \cdots, J; k = 1, \cdots, K; \qquad (7)$$

where x_{ijk} is the fluorescence intensity of the ith sample at emission wavelength j and excitation wavelength k; a_{if} is directly proportional to the abundance of the fth analyte in the ith sample. b_{jf} and c_{kf} are linearly related to emission and excitation wavelength j and k of the fth analyte, respectively. Residual matrix e_{ijk} contains variability that cannot be explained by the trilinear model. F defines the number of components that can be resolved by the model.

PARAFAC allows statistical identification and quantification of different fluorophores and helps to trace changes of relative concentrations of independent components in the environment (Jørgensen *et al.*, 2011). The use of EEMs-PARAFAC techniques has shown great potential to distinguish DOM sources and to trace DOM dynamics in various aquatic environments, including rivers, estuarine systems, and open ocean.

1.2. Objectives and Chapter Overview

The main focus of this dissertation is to better estimate UV optical properties (K_d, a_g) from remotely sensed ocean color (R_rs) in visible wavelengths and thereby potentially provide better models for photochemistry driven by UV–CDOM interactions. This dissertation work covers a broad spectrum of optics, from basic oceanographic survey sampling and laboratory photochemical analysis to ocean color algorithm development and remote sensing applications. In the chapters that follow, I aim to address each of the two optical variables described in

Equation (6) using remote sensing techniques and introduce a new approach to estimate photochemical fluxes in a dynamic near-shore environment from a high-resolution satellite image.

The first data chapter (Chapter 2) is dedicated to improving performance for retrieval of K_d(UV) from R_{rs}. Previous Sea*UV*/Sea*UV*c algorithms (Fichot *et al.,* 2008) have shown limitations in near-shore, optically complex environments due to a lack of darker inshore samples in its training data set. We collected field optical data in coastal Georgia, pooled it with the original training and external validation data sets to develop a composite product of Sea*UV*/Sea*UV*c algorithms that is universally applicable to a variety of water types. A detailed, step-by-step description of implementing the composite algorithms, including intermediate steps toward the final product are given in Appendix A and B respectively.

In Chapter 3, I present a novel algorithm (Sea*CDOM*) that allows direct retrieval of a fully resolved CDOM absorption spectrum over UV wavelengths from visible R_{rs}. I developed this algorithm using a suite of statistical approaches and obtained good accuracy for a_g retrieval, with a mean absolute percent difference for a_g in the UV of ~25%. This new algorithm contributes to improved accuracy for photochemical and photobiological rate calculations from ocean color. One of its advantages is that no prior assumptions of CDOM absorption spectral shape is required, making it free of spectral slope extrapolations from visible wavelengths that have hampered previous models. This has potential to provide insights about the chemical composition (e.g., molecular weight and aromaticity), origins, transformation and cycling pathways of CDOM on global as well as regional scales. I provide a description of implementing the SeaCDOM algorithms in Appendix C.

In Chapter 4, I introduce a new approach to the calculation of photochemical rates by blending the two distinct algorithms developed in Chapter 2 and 3 (composite Sea*UV* and Sea*CDOM* algorithms) and apply this to a single coastal HICO image centered on Sapelo Island, GA, USA, to estimate CO photoproduction as an example. I demonstrate the high spatial variability of depth-specific, as well as depth-integrated photoproduction rates of CO on a small estuarine scale. With the new capability of independent retrievals for a_g and K_d, I am able to reveal the underlying optical principle that governs the distribution of depth-integrated photochemistry in the UV from ocean color.

Finally, Chapter 5 explores the distribution and dynamics of DOM using absorbance and fluorescence techniques on samples collected in the Gulf of Alaska during a high resolution field campaign. I assess potential biogeochemical and physical processes driving the distributions of these optical properties and attempt to develop a multi-linear relationship between DOC and protein-like fluorescent components, exploring the potential of using fluorescent information to trace bulk DOC in the ocean, especially the refractory fraction of DOM.

References

Amon, R.M.W., Budéus, G., Meon, B., 2003. Dissolved organic carbon distribution and origin in the Nordic Seas: Exchanges with the Arctic Ocean and the North Atlantic. Journal of Geophysical Research: Oceans (1978–2012) 108 (C7).

Austin, R.W., Petzold, T.J., 1981. The determination of the diffuse attenuation coefficient of sea water using the Coastal Zone Color Scanner. Oceanography from space. Springer, pp. 239-256.

Blough, N.V., Del Vecchio, R., 2002. Chromophoric DOM in the coastal environment. Biogeochemistry of marine dissolved organic matter, 509-546.

Bricaud, A., Morel, A., Prieur, L., 1981. Absorption by dissolved organic matter of the sea (yellow substance) in the UV and visible domains. Limnology and Oceanography 26 (1), 43-53.

Carder, K.L., Steward, R.G., Harvey, G.R., Ortner, P.B., 1989. Marine humic and fulvic acids: Their effects on remote sensing of ocean chlorophyll Limnology and Oceanography 34 (1), 68-81.

Chen, R.F., Bada, J.L., 1992. The fluorescence of dissolved organic matter in seawater. Marine chemistry 37 (3), 191-221.

Coble, P.G., 1996. Characterization of marine and terrestrial DOM in seawater using excitation-emission matrix spectroscopy. Marine chemistry 51 (4), 325-346.

Del Castillo, C.E., Miller, R.L., 2008. On the use of ocean color remote sensing to measure the transport of dissolved organic carbon by the Mississippi River Plume. Remote Sensing of Environment 112 (3), 836-844.

Fichot, C.G., Benner, R., 2012. The spectral slope coefficient of chromophoric dissolved organic matter (S275-295) as a tracer of terrigenous dissolved organic carbon in river-influenced ocean margins. Limnology and Oceanography 57 (5), 1453-1466.

Fichot, C.G., Kaiser, K., Hooker, S.B., Amon, R.M.W., Babin, M., Belanger, S., Walker, S.A., Benner, R., 2013. Pan-Arctic distributions of continental runoff in the Arctic Ocean. Scientific Reports 3.

Fichot, C.G., Lohrenz, S.E., Benner, R., 2014. Pulsed, cross- shelf export of terrigenous dissolved organic carbon to the Gulf of Mexico. Journal of Geophysical Research: Oceans 119 (2), 1176-1194.

Fichot, C.G., Miller, W.L., 2010. An approach to quantify depth-resolved marine photochemical fluxes using remote sensing: Application to carbon monoxide (CO) photoproduction. Remote Sensing of Environment 114 (7), 1363-1377.

Fichot, C.G., Sathyendranath, S., Miller, W.L., 2008. SeaUV and SeaUV C: Algorithms for the retrieval of UV/Visible diffuse attenuation coefficients from ocean color. Remote Sensing of Environment 112 (4), 1584-1602.

Gao, H., Zepp, R.G., 1998. Factors influencing photoreactions of dissolved organic matter in a coastal river of the southeastern United States. Environmental Science & Technology 32 (19), 2940-2946.

Garver, S.A., Siegel, D.A., 1997. Inherent optical property inversion of ocean color spectra and its biogeochemical interpretation .1. Time series from the Sargasso Sea. Journal of Geophysical Research-Oceans 102 (C8), 18607-18625.

Helms, J.R., Stubbins, A., Perdue, E.M., Green, N.W., Chen, H., Mopper, K., 2013. Photochemical bleaching of oceanic dissolved organic matter and its effect on absorption spectral slope and fluorescence. Marine Chemistry 155, 81-91.

Helms, J.R., Stubbins, A., Ritchie, J.D., Minor, E.C., Kieber, D.J., Mopper, K., 2008. Absorption spectral slopes and slope ratios as indicators of molecular weight, source, and photobleaching of chromophoric dissolved organic matter. Limnology and Oceanography 53 (3), 955-969.

Johannessen, S.C., Miller, W.L., Cullen, J.J., 2003. Calculation of UV attenuation and colored dissolved organic matter absorption spectra from measurements of ocean color. Journal of Geophysical Research: Oceans (1978–2012) 108 (C9).

Jørgensen, L., Stedmon, C.A., Kragh, T., Markager, S., Middelboe, M., Søndergaard, M., 2011. Global trends in the fluorescence characteristics and distribution of marine dissolved organic matter. Marine chemistry 126 (1), 139-148.

Kirk, J.T., 1994. Light and photosynthesis in aquatic ecosystems. Cambridge university press.

Kjeldstad, B., Frette, Ø., Erga, S.R., Browman, H.I., Kuhn, P.S., Davis, R.F., Miller, W., Stamnes, J.J., 2003. UV (280 to 400 nm) optical properties in a Norwegian fjord system and an intercomparison of underwater radiometers.

Kowalczuk, P., Durako, M.J., Young, H., Kahn, A.E., Cooper, W.J., Gonsior, M., 2009. Characterization of dissolved organic matter fluorescence in the South Atlantic Bight with use of PARAFAC model: Interannual variability. Marine chemistry 113 (3), 182-196.

Lee, Z., Hu, C., Shang, S., Du, K., Lewis, M., Arnone, R., Brewin, R., 2013. Penetration of UV- visible solar radiation in the global oceans: Insights from ocean color remote sensing. Journal of Geophysical Research: Oceans 118 (9), 4241-4255.

Lee, Z.P., Carder, K.L., Arnone, R.A., 2002. Deriving inherent optical properties from water color: a multiband quasi-analytical algorithm for optically deep waters. Applied Optics 41 (27), 5755-5772.

Mannino, A., Russ, M.E., Hooker, S.B., 2008. Algorithm development and validation for satellite-derived distributions of DOC and CDOM in the US Middle Atlantic Bight. J. Geophys. Res 113 (C07051).

Maritorena, S., Siegel, D.A., Peterson, A.R., 2002. Optimization of a semianalytical ocean color model for global-scale applications. Applied Optics 41 (15), 2705-2714.

Mopper, K., Kieber, D.J., 2000. Marine photochemistry and its impact on carbon cycling. The effects of UV radiation in the marine environment 10, 101-129.

Moran, M.A., Zepp, R.G., 1997. Role of photoreactions in the formation of biologically labile compounds from dissolved organic matter. Limnology and Oceanography 42 (6), 1307-1316.

Morel, A., Maritorena, S., 2001. Bio- optical properties of oceanic waters: A reappraisal. Journal of Geophysical Research: Oceans (1978–2012) 106 (C4), 7163-7180.

Powers, L.C., Miller, W.L., 2015. Photochemical production of CO and CO 2 in the Northern Gulf of Mexico: Estimates and challenges for quantifying the impact of photochemistry on carbon cycles. Marine chemistry 171, 21-35.

Stedmon, C.A., Markager, S., 2005. Resolving the variability in dissolved organic matter fluorescence in a temperate estuary and its catchment using PARAFAC analysis. Limnology and Oceanography 50 (2), 686-697.

Stedmon, C.A., Markager, S., Bro, R., 2003. Tracing dissolved organic matter in aquatic environments using a new approach to fluorescence spectroscopy. Marine Chemistry 82 (3), 239-254.

Stedmon, C.A., Markager, S., Kaas, H., 2000. Optical Properties and Signatures of Chromophoric Dissolved Organic Matter (CDOM) in Danish Coastal Waters. Estuarine, Coastal and Shelf Science 51 (2), 267-278.

Stubbins, A., Niggemann, J., Dittmar, T., 2012. Photo-lability of deep ocean dissolved black carbon. Biogeosciences 9 (5), 1661-1670.

Swan, C.M., Nelson, N.B., Siegel, D.A., Fields, E.A., 2013. A model for remote estimation of ultraviolet absorption by chromophoric dissolved organic matter based on the global distribution of spectral slope. Remote Sensing of Environment 136, 277-285.

Toole, D.A., Kieber, D.J., Kiene, R.P., Siegel, D.A., Nelson, N.B., 2003. Photolysis and the dimethylsulfide (DMS) summer paradox in the Sargasso Sea. Limnology and Oceanography 48 (3), 1088-1100.

Twardowski, M.S., Boss, E., Sullivan, J.M., Donaghay, P.L., 2004. Modeling the spectral shape of absorption by chromophoric dissolved organic matter. Marine Chemistry 89 (1-4), 69-88.

Vähätalo, A.V., Wetzel, R.G., 2004. Photochemical and microbial decomposition of chromophoric dissolved organic matter during long (months-years) exposures. Marine Chemistry 89 (1-4), 313-326.

Walker, S.A., Amon, R.M.W., Stedmon, C., Duan, S., Louchouarn, P., 2009. The use of PARAFAC modeling to trace terrestrial dissolved organic matter and fingerprint water masses in coastal Canadian Arctic surface waters. Journal of Geophysical Research: Biogeosciences (2005–2012) 114 (G4).

Wang, M., Son, S., Harding, L.W., 2009. Retrieval of diffuse attenuation coefficient in the Chesapeake Bay and turbid ocean regions for satellite ocean color applications. Journal of Geophysical Research: Oceans (1978–2012) 114 (C10).

Werdell, P. J. (2009). Diffuse attenuation coefficient (K_d) for downwelling irradiance at 490-nm. http://oceancolor.gsfc.nasa.gov/REPROCESSING/R2009/kdv4/.

Whitehead, R.F., de Mora, S.J., Demers, S., 2000. Enhanced UV radiation—a new problem for the marine environment. The effects of UV radiation in the marine environment 10, 1-34.

Williamson, C.E., Zepp, R.G., Lucas, R.M., Madronich, S., Austin, A.T., Ballaré, C.L., Norval, M., Sulzberger, B., Bais, A.F., McKenzie, R.L., 2014. Solar ultraviolet radiation in a changing climate. Nature Climate Change 4 (6), 434-441.

Yamashita, Y., Cory, R.M., Nishioka, J., Kuma, K., Tanoue, E., Jaffé, R., 2010. Fluorescence characteristics of dissolved organic matter in the deep waters of the Okhotsk Sea and the northwestern North Pacific Ocean. Deep Sea Research Part II: Topical Studies in Oceanography 57 (16), 1478-1485.

Yamashita, Y., Jaffé, R., Maie, N., Tanoue, E., 2008. Assessing the dynamics of dissolved organic matter (DOM) in coastal environments by excitation emission matrix fluorescence and parallel factor analysis (EEM- PARAFAC). Limnology and Oceanography 53 (5), 1900-1908.

Yamashita, Y., Nosaka, Y., Suzuki, K., Ogawa, H., Takahashi, K., Saito, H., 2013. Photobleaching as a factor controlling spectral characteristics of chromophoric dissolved organic matter in open ocean. Biogeosciences 10 (11), 7207-7217.

Yamashita, Y., Tanoue, E., 2003. Chemical characterization of protein-like fluorophores in DOM in relation to aromatic amino acids. Marine chemistry 82 (3), 255-271.

Zafiriou, O.C., Andrews, S.S., Wang, W., 2003. Concordant estimates of oceanic carbon monoxide source and sink processes in the Pacific yield a balanced global “blue- water” CO budget. Global Biogeochemical Cycles 17 (1).

Zepp, R.G., Erickson Iii, D.J., Paul, N.D., Sulzberger, B., 2007. Interactive effects of solar UV radiation and climate change on biogeochemical cycling. Photochemical & Photobiological Sciences 6 (3), 286-300.

Ziolkowski, L.A., Miller, W.L., 2007. Variability of the apparent quantum efficiency of CO photoproduction in the Gulf of Maine and Northwest Atlantic. Marine chemistry 105 (3), 258-270.

CHAPTER 2

IMPROVED ALGORITHMS FOR ACCURATE RETRIEVAL OF UV/VISIBLE DIFFUSE ATTENUATION COEFFICIENTS IN OPTICALLY COMPLEX, INSHORE WATERS[1,2]

---

[1] Cao, F., Fichot, C. G., Hooker, S. B., & Miller, W. L. (2014). *Remote Sensing of Environment*, *144*, 11-27, doi:10.1016/j.rse.2014.01.003; Reprinted here with permission of the publisher.

[2] Per the dissertation committee's request, minimal edits were made to this chapter.

Abstract

Photochemical processes driven by high-energy ultraviolet radiation (UVR) in inshore, estuarine, and coastal waters play an important role in global biogeochemical cycles and biological systems. A key to modeling photochemical processes in these optically complex waters is an accurate description of the vertical distribution of UVR in the water column which can be obtained using the diffuse attenuation coefficients of downwelling irradiance ($K_d(\lambda)$). The Sea*UV*/Sea*UVc* algorithms (Fichot et al., 2008) can accurately retrieve K_d (λ = 320, 340, 380, 412, 443 and 490 nm) in oceanic and coastal waters using multispectral remote sensing reflectances ($R_{rs}(\lambda)$, SeaWiFS bands). However, Sea*UV*/Sea*UVc* algorithms are currently not optimized for use in optically complex, inshore waters, where they tend to severely underestimate $K_d(\lambda)$. Here, a new training data set of optical properties collected in optically complex, inshore waters was used to re-parameterize the original Sea*UV*/Sea*UVc* algorithms, resulting in improved $K_d(\lambda)$ retrievals for turbid, estuarine waters. Although the updated Sea*UV*/Sea*UVc* algorithms perform best in optically complex waters, the original Sea*UV*/Sea*UVc* models still perform well in most coastal and oceanic waters. Therefore, we propose a composite set of Sea*UV*/Sea*UVc* algorithms, optimized for $K_d(\lambda)$ retrieval in almost all marine systems, ranging from oceanic to inshore waters. The composite algorithm set can retrieve K_d from ocean color with good accuracy across this wide range of water types (e.g., within a mean relative error of 13% for $K_d(340)$). A validation step using three independent, *in situ* data sets indicates that the composite Sea*UV*/Sea*UVc* can generate accurate $K_d(\lambda)$ values at λ = 320 – 490 nm from ocean color on a global scale. Taking advantage of the inherent benefits of our statistical methods, we pooled the validation data with the training set, obtaining an optimized composite model for estimating $K_d(\lambda)$ in UV wavelengths for almost all marine

waters. This “optimized composite” set of Sea*UV*/Sea*UVc* algorithms will provide the optical community with improved ability to quantify the role of solar UV radiation in photochemical and photobiological processes in the ocean.

1. Introduction

Solar ultraviolet radiation (UVR; 280-400 nm) is a critical factor in regulating the biogeochemical cycles in the ocean (Whitehead et al., 2000). High-energy UVR is the driving factor for the photooxidation of colored dissolved organic matter (CDOM), the dominant UVR-absorbing component within the larger pool of dissolved organic carbon (DOC), especially in coastal areas and estuaries (Mopper and Kieber, 2000). The photochemical degradation and mineralization of CDOM can therefore have an important effect on biogeochemical carbon cycling in the ocean. UVR also impacts bacterial and photosynthetic activity through DNA damage and repair processes in natural waters (Sinha and Häder, 2002; Tedetti and Sempéré, 2006).

Quantitative assessment of in situ photochemical and photobiological processes can benefit from knowledge of the vertical distribution of UV and visible radiation in natural waters (Fichot and Miller, 2010). The diffuse attenuation coefficient, $K_d(\lambda)$, is defined as the fractional rate of decay of downwelling spectral irradiance with depth and can be used to calculate vertical profiles of irradiance in the water column from measurements of surface irradiance (Kirk, 1994a). The diffuse attenuation coefficient depends not only on the optically active water constituents, but also on the distribution of the ambient light field (solar zenith angle, surface and sky conditions, etc.) (Lee et al., 2005). K_d spans several orders of magnitude between the clearest oceanic waters (e.g., surface subtropical gyres, $K_d(340) = 0.035\ m^{-1}$) (Morel et al., 2007a, 2007b) and the darkest inshore waters (e.g., dark oligotrophic lakes, $K_d(340) = 3.8\ m^{-1}$) (Booth et al., 1997; Kjeldstad et al., 2003). Satellite imagery could therefore facilitate the quantification of K_d over large temporal and spatial scales.

The determination of K_d is amenable to the remote sensing of ocean color. Austin and Petzold (1981) first proposed an empirical relationship between K_d and a blue-green ratio of water-leaving radiance ($L_w(443)/ L_w(555)$) in order to facilitate the retrieval of $K_d(490)$ from ocean-color remote sensing. Previous efforts of K_d retrieval for Case 1 and Case 2 waters generally included only visible bands, and were based on either empirical or semi-analytical methods (Kuhn et al., 1999; Jamet et al., 2012; Johannessen et al., 2003; Mueller, 2000). However, few studies have focused on the retrieval of K_d in the UV domain, especially in turbid estuaries. Fichot et al. (2008) recently developed the Sea*UV* and Sea*UVc* algorithms for the retrieval of $K_d(\lambda)$ (λ = 320–490 nm) from multispectral remote-sensing reflectances (λ = 412–670 nm) in the ocean. These algorithms were developed and validated for coastal and open ocean waters. However, these algorithms can severely underestimate K_d retrievals in the UV when applied to inshore waters (as shown later in Section 3.1). This clearly calls for a refined approach and tuning of the original model for improved accuracy of $K_d(\lambda)$ retrievals in optically complex inshore waters.

In this study, *in situ* measurements of optical properties collected in turbid, CDOM-rich coastal and inshore areas are used to enhance the applicability of Sea*UV* and Sea*UVc* algorithms in optically complex waters. This new data set is used along with the original training data set of Fichot et al. (2008) to develop and validate a "composite Sea*UV* and Sea*UVc*" algorithm set optimized for water types ranging from blue oceanic to highly productive, turbid inshore waters (see Table 2.1). This new algorithm set will enhance our capability to monitor the *in situ* attenuation of solar radiation (UV-visible) and quantify photochemical and photobiological processes in most natural waters.

2. Data and Approach

2.1. Background of current Sea*UV* algorithms

The Sea*UV*/Sea*UVc* algorithms can be used to retrieve $K_d(\lambda)$ at λ = 320, 340, 380, 412, 443 and 490 nm from spectral remote-sensing reflectance ($R_{rs}(\lambda)$) in the visible range. The basic approach uses a principal component analysis (PCA) to collapse $R_{rs}(\lambda)$ spectra (λ = 412, 443, 490, 510, 555 and 670 nm) into four principal components (PCs). Multi-linear regressions were then parameterized between measured *in situ* $K_d(\lambda)$ and the four PCs, resulting in a model named Sea*UV*. In Sea*UVc*, a cluster analysis was applied to the first two PC scores in order to divide the ocean color data set into distinct ocean color domains based on the $R_{rs}(\lambda)$ spectral characteristics. This classification allowed the derivation of ocean color domain-specific multi-linear parameters. The use of PCs in Sea*UV* and Sea*UV*c resulted in a more complete utilization of the multispectral information contained in $R_{rs}(\lambda)$ spectra, and provided more accurate $K_d(\lambda)$ retrievals compared to traditional band-ratio methods that only use R_{rs} at two wavelengths (Fichot et al., 2008). In the rest of this manuscript, the Fichot et al. (2008) algorithms are referred to as the "original" Sea*UV*/Sea*UVc* model.

2.2. Study area and data collection

Sampling was conducted in three distinct estuarine systems along the Southeastern coast of the U.S. (Altamaha, Doboy and Sapelo sounds in Georgia) (Figure 2.1). A total set of 74 *in situ*, simultaneous measurements of $R_{rs}(\lambda)$ and $K_d(\lambda)$ were collected in June 2006, February 2007, August 2009, July 2010, March 2011, and June 2011. The three sampled estuarine systems had distinct hydrological settings. The Altamaha Sound is a river-dominated site and receives freshwater inputs and large amounts of suspended particles from the Altamaha River. It is generally characterized by high loadings (~ 30 mg/l) of total suspend solids (TSS) (Witte et al., 1982). The optical properties of the Altamaha Sound are further complicated by the organic matter accumulation promoted by freshwater input from the Altamaha River (Craft, 2007). Doboy Sound is located to the north of Altamaha Sound and is a tidal marsh-dominated site. It can receive significant riverine input from the Altamaha River during high flow seasons (usually February to April). Sapelo Sound is the northernmost site sampled and is a coastal, marine-dominated site, comparatively more saline and experiencing less hydrological variation than its neighboring estuaries to the south (Richardson and LeDrew, 2006). The study area spanning the three estuarine systems is characterized as a CDOM-rich ($a_{CDOM}(300)$ up to 13 m^{-1}) and highly dynamic system with periodic heavy loads of suspended particles.

Two optical instruments were deployed at each sampling station and all measurements were taken within 2 h of solar noon (solar zenith angle (SZA) varied in the range of 15º ~ 35º) in order to preserve the quasi-inherent property of the diffuse attenuation coefficient (Gordon, 1989). A Satlantic® multispectral profiling radiometer (MicroPRO, with wavebands centered at λ = 305, 325, 340, 380, 412, 443, 490, 555 nm) was deployed three or more times at each station to measure profiles of spectral downwelling irradiance ($E_d(\lambda, z)$, $\mu W\ cm^{-2}\ nm^{-1}$). The MicroPRO was either lowered slowly by hand on the sunny side of a small vessel or floated away and used in free-fall mode depending on data density and orientation requirements. Data with instrument tilt greater than 5º was removed before algorithm development. The optical depth, $\zeta(\lambda, z)$, was calculated as in Eq. (1):

$$\zeta(\lambda, z) = -\ln\left(E_d(\lambda, z)/E_d(\lambda, 0^-)\right) \qquad (1)$$

where $E_d(\lambda, 0^-) \approx E_d(\lambda, 0^+)/1.04$, (Austin, 1974; Kirk, 1994a).

The diffuse attenuation coefficient, $K_d(\lambda)$, was calculated as in Eq. (2):

$$K_d(\lambda) = \zeta(\lambda, z)/z \quad (2)$$

where z is the water depth at which the detection limit of the instrument is reached. Typical z values were < 0.5 m for K_d (340) and no optical stratification was noted over this depth.

Paired Satlantic® multispectral OCR507 radiometers mounted on a buoy were used to measure above-surface remote-sensing reflectance ($R_{rs}(\lambda, 0^+)$, sr^{-1}) at λ = 305, 325, 340, 380, 412, 443, 490, 510, 555, 670, and 683 nm. The OCR system was deployed on the sunny side of the boat, and at the same time as the MicroPRO in order to obtain simultaneous measurements of $K_d(\lambda)$ and $Rrs(\lambda)$. The OCR system measured simultaneously above-surface downwelling irradiance ($E_d(\lambda, 0^+)$, µW cm^{-2} nm^{-1}) and just-below-surface (~2–3 cm) upwelling radiance ($L_u(\lambda, 0^-)$, µW cm^{-2} nm^{-1} sr^{-1}). Water-leaving radiance, $L_w(\lambda)$, was then derived from $L_u(\lambda, 0^-)$ using the approximation $L_W(\lambda) \approx 0.54 * L_u(\lambda, 0^-)$ of Austin (1974). The $R_{rs}(\lambda, 0^+)$ was then calculated as the ratio of $L_w(\lambda)$ over $E_d(\lambda, 0^+)$ for the following wavelengths: λ = 412, 443, 490, 510, 555 and 670 nm. Due to high levels of CDOM and turbidity, the study area is considered to be optically deep and bottom effects on the determination on R_{rs} can be neglected. The MicroPRO and OCR were re-calibrated annually by Satlantic, Inc. Uncertainties (such as sun elevation, surface extrapolations, etc.) associated with R_{rs} and K_d measurements are detailed in Fichot et al. (2008).

2.3. Optimization of original Sea*UV* algorithms for optically complex, inshore waters

In a first attempt to optimize the algorithms, the inshore-water data set collected in this study (N = 74) was pooled into the original training data set of Fichot et al. (2008), and the models were re-parameterized using the exact same approach as the one used in Fichot et al. (2008). However, simple re-parameterization using this updated data set (N = 438) did not achieve better overall performance (see Appendix B). To better estimate K_d in inshore waters and maintain the good performance of original algorithms of K_d retrieval in open ocean waters as well, the original approach used by Fichot et al. (2008) was therefore modified to optimize the performance of the algorithms from open ocean waters to optically complex inshore waters.

2.3.1. Determination of the cutoff point for inshore waters

The new approach to improve the performance of the original Sea*UV*/Sea*UVc* algorithms for inshore waters was developed by re-parameterizing the multi-linear equations with a re-defined, inshore water training data set split from the complete data set. In the rest of this manuscript, the models developed with this new approach are referred to as “inshore-water optimized” Sea*UV*/Sea*UVc*. A cutoff value based on $K_d(490)$ was defined to distinguish inshore waters for which Sea*UV*/Sea*UVc* should be optimized. $K_d(490)$ was chosen to distinguish inshore waters from other water types for two reasons. First, $K_d(490)$ gave the least accurate retrieval when the original Sea*UV*/Sea*UVc* was applied to our new inshore water data (as shown later in Section 3.2). Second, $K_d(490)$ is a standard NASA product from SeaWiFS data that allows a determination of water type with AOP's external to the Sea*UV*/Sea*UVc* implementation. This eliminates potential internal bias when applying our new approach to remotely sensed ocean color.

To determine the cutoff point, we first sorted the measured *in situ* $K_d(490)$ in ascending order and then applied a five–point moving-average smoothing function to both the measured *in situ* $K_d(490)$ and estimated $K_d(490)$ values retrieved from the latest NASA $K_d(490)$ product (Werdell, 2009). Figure 2.2 (a) displays the performance of the $K_d(490)$ product on our complete data set. The cutoff point was chosen to be at the point where the measured $K_d(490)$ began to diverge from the estimated values in the $K_d(490)$ product. By examining the smoothed curve in Figure 2.2 (b), the cutoff point was determined to be 0.32 m^{-1} for $K_d(490)$. Any measured

K_d(490) values in the combined data set which was greater than 0.32 m^{-1} was considered as optically complex inshore water, giving a total of 119 points to be included in the inshore water training data used to derive the new parameters for the inshore-water optimized *SeaUV* algorithms.

2.3.2. Optimization of Sea*UV*/Sea*UVc* algorithms for inshore waters

The inshore water training data set (N = 119) was first log-transformed and then re-standardized following Equation (2) in Fichot et al. (2008). To optimize the Sea*UV* algorithms for inshore waters, the re-standardized $R_{rs}(\lambda)$ data of the inshore water training data set (N = 119) were combined into four principal components, and regression coefficients were generated by fitting a multi-linear relationship between the four PC scores and the measured K_d values. A fuzzy c-means cluster analysis (FCM) was then applied to the two-dimensional (2-D) data set spanned by the first two PC scores generated in the inshore-water optimized Sea*UV*. We used the c-means function in the R software package (http://www.r-project.org/) to carry out the cluster analysis. The algorithms are based on minimizing the objective function defined as follows in Eq. (3):

$$J_m = \sum_{i=1}^{N} \sum_{j=1}^{C} \mu_{ij}^{m} \left\| x_i - c_j \right\|^2 \qquad (3)$$

where m is the weighting component; x_i is the ith observation in the 2D dataset spanned by the first two PCs; c_j defines the cluster centers in the 2D dataset; μ_{ij} is the degree of membership of x_i to the cluster j, and $\left\| x_i - c_j \right\|$ is the Euclidean norm which represents the similarity between the measured data and the cluster centers (Moore et al., 2009). Evaluated by multiple fuzzy cluster indexes (e.g. partition coefficient, partition entropy, etc.), four representative dark water ocean color domains (DWDs) were defined and the cluster centers were determined when the optimization criteria were satisfied (Moore et al., 2001). This use of FCM (also known as the soft

K-means clustering method) is the only difference between the current approach and the original Fichot et al. (2008) method, which applied a hard *K*-means clustering method. Through the membership assignment of every data point to different clusters, FCM provides more robust estimation of cluster centers than the hard *K*-means method, where cluster centers must be optimized through many trials. Another advantage of applying FCM over the conventional hard *K*-means method is that the number of clusters can be optimized and validated through multiple validity indexes, a more objective and convincing method than the pre-specified cluster numbers from hard *K*-means method. Figure 2.3 shows the $R_{rs}(\lambda)$ spectra for the four dark water domains. The number of samples assigned to each of the four DWDs are 20, 31, 31 and 37, respectively.

2.4. Development of composite Sea*UV*/Sea*UVc* algorithms

The original Sea*UV* algorithms still performed best in open ocean and coastal waters, where $K_d(490) < 0.32$ m^{-1}. In order to optimize the overall performance of the algorithms in the full range of natural water types, we assembled and tested a composite version of the algorithms. This composite algorithm uses the original Sea*UV*/Sea*UVc* for open ocean and coastal waters (where $K_d(490) < 0.32$ m^{-1}), and the inshore-water optimized Sea*UV*/Sea*UVc* for optically complex waters (where $K_d(490) \geq 0.32$ m^{-1}).

2.5. Accuracy assessment

The mean relative error (MRE(λ)) was calculated in order to evaluate the accuracy of $K_d(\lambda)$ retrievals and the overall performance of the original, inshore-water optimized, and composite Sea*UV*/Sea*UVc* algorithms. The MRE(λ)) is defined in Eq. (4) as follows:

$$MRE(|\bar{\varepsilon}|, \lambda) = \frac{1}{N}\sum_{i=1}^{N}|\varepsilon_i|\,(\lambda) \tag{4a}$$

where $$\varepsilon_i = 100 * \frac{K_d(\lambda)^{estimated} - K_d(\lambda)^{measured}}{K_d(\lambda)^{measured}} \tag{4b}$$

and where i is the index number, and N is the number of observations. Note that $K_d(\lambda)$ values measured at $\lambda = 325$ and $\lambda = 340$ nm were linearly extrapolated to calculate the $K_d(\lambda)$ value at $\lambda = 320$ nm to allow direct accuracy comparison to the original Sea*UV*/Sea*UVc* results.

3. Results and Discussion

3.1. Evaluation of original Sea*UV* algorithms for inshore waters

The original Sea*UV* algorithms were first implemented using the complete data set of $R_{rs}(\lambda)$ spectra that includes our new inshore-water stations. As shown in Figures 2.4, 2.5 and 2.6, the $K_d(\lambda)$ values derived in inshore waters using the original Sea*UV* algorithms are underestimated relative to the measured *in situ* $K_d(\lambda)$. The bias increases as values for $K_d(\lambda)$ increase and the underestimation is more distinct when the original Sea*UVc* was applied to the inshore water data set alone. For example, in Figure 2.6, the original Sea*UVc* generates higher biases and performs more poorly for $K_d(320)$ than Sea*UV*. The accuracy of $K_d(490)$ estimated in inshore waters using the original Sea*UVc* shows slightly better performance than Sea*UV*, but remains low. The severe underestimation of estimated K_d values in inshore waters reflects the fact that the original Sea*UV*/Sea*UVc* algorithms were parameterized for coastal and open ocean water. In optically complex inshore waters, K_d values are higher (e.g. at Altamaha Sound, with $K_d(340) \sim 18.7\ \mathrm{m}^{-1}$) and extend out of the range for which the model was originally developed, most likely contributing to its inability to accurately predict K_d in the new inshore water data set.

3.2. Performance assessment of inshore-water optimized Sea*UV*/Sea*UVc* algorithms

Instead of simply re-parameterizing the original model with an expanded data set that included an extended K_d range, our cutoff point ($K_d(490) = 0.32\ \mathrm{m}^{-1}$) was applied for the inshore-water optimized algorithms to distinguish optically complex inshore waters from the other water types. Data with $K_d(490)$ values above the cutoff point were classified as optically complex ($N =$

119) and were used as a separate training data set for parameterizing the inshore-water optimized algorithms. MRE values derived from the inshore-water optimized algorithms are significantly reduced compared to those derived using the original Sea*UV* algorithms (e.g. for $K_d(380)$, MRE = 17.6% from inshore-water optimized algorithms, compared to MRE = 42.9% from original Sea*UV*, error distribution and fitting parameters as shown in the supplementary material).

While K_d in inshore waters is generally retrieved with good accuracy at most wavelengths after optimization, retrieval of $K_d(320)$ using the inshore-water optimized Sea*UV* algorithms yields higher errors compared to the K_d estimates at longer wavelengths (MRE for $K_d(320)$ = 21.4%, compared to MRE = 15% for $K_d(412)$). This higher error for $K_d(320)$ could be related to the difficulty of measuring K_d at UV wavelengths in highly colored waters. Since most of the apparent optical properties (AOPs) in the optically complex water training data set used to parameterize the inshore-water optimized Sea*UV* algorithms were collected in coastal Georgia waters (high CDOM and particulate load), measurements of downward UV irradiance generally rapidly falls below the detection limits of the instrument during profiling. The measured *in situ* $K_d(320)$ data likely contained more inaccuracy than longer wavelengths when parameterizing of the algorithms. In addition, the strong attenuation of UV radiation in dark water requires K_d measurements to be made very close to the water surface where wave-induced fluctuations may contribute larger variations to the spectral irradiance measurement (Markager and Vincent, 2000; Laurion et al., 1997; Tedetti et al., 2007). These challenges of K_d measurements at shorter UV wavelengths in optically complex waters could explain the increasing uncertainty of K_d values observed at shorter wavelengths.

3.3. Evaluation of composite Sea*UV* algorithms

The composite Sea*UV* algorithms improved the accuracy of retrieved K_d in inshore waters. Figures 2.4, 2.5 and 2.6 display the K_d retrievals with their relative error distributions that result from use of the composite Sea*UV*/Sea*UVc* algorithms applied to the entire training data set (N = 438). The good agreement between measured and retrieved K_d values demonstrates the improved overall performance of the composite Sea*UV*/Sea*UVc* algorithms (e.g. for K_d(380), MRE = 16% from composite Sea*UV*, compared with MRE = 21% from original Sea*UV*).

The approach used in the composite Sea*UV* algorithms is similar to the merged K_d(490) product for Chesapeake Bay developed by Wang et al. (2009), which combines two separate empirical algorithms for K_d(490) retrieval of open ocean and turbid coastal waters to derive K_d(490) from satellite measurements. Good results for K_d retrieval using our composite algorithms result partly from accurate determination of the cutoff point (K_d (490) = 0.32 m^{-1}) used to separate the fitting parameters for the composite algorithms. In the merged K_d(490) product generated by Wang et al. (2009), using a completely separate data set, the same cutoff point of K_d(490) = 0.3 m^{-1} was proposed to distinguish the open ocean water with turbid coastal water. The combination of the two individual parts in the composite algorithms, with each part applicable to different water types, maximizes our ability to accurately predict K_d through the UV wavelength range in both open ocean and turbid inshore waters.

3.4. Sensitivity analysis of the cutoff point

By using the latest NASA K_d(490) product to determine the switch point between different parts in the composite Sea*UV*/Sea*UVc* algorithms, it is possible that the error (~25%) in determining K_d(490) for our training dataset, particularly for open ocean water (K_d(490) < 0.32 m^{-1}), could translate to increased error in our ability to choose the K_d(490) value that will prompt a switch between algorithms. We investigated the sensitivity of our retrieval accuracy using the composite Sea*UV* algorithms, by varying the cutoff point over the range between 0.16 and 0.36 m^{-1} for $K_d(490)$, corresponding to the ±25% error limits of the cutoff point derived from the $K_d(490)$ product. The estimated K_d (λ, λ = 320, 340, 380, 412, 443 and 490 nm) for our training dataset obtained by varying the cutoff point ±25% showed no statistically significant differences from the calculated $K_d(\lambda)$ values obtained with the cutoff point value set at $K_d(490) = 0.32$ m^{-1} (*t*-tests, with p-value > 0. 05 for $K_d(\lambda)$ at each wavelength, $N = 438$). Hence, the use of our $K_d(490) = 0.32$ m^{-1} switch point between clear and dark algorithms is not sensitive to the error associated implicitly with retrieval of the $K_d(490)$ product.

3.5. Validation of the composite Sea*UV* algorithms

Three independent sets of *in situ* AOPs were used to test the applicability of the composite Sea*UV*/Sea*UVc* algorithms. Paired measurements of $R_{rs}(\lambda)$ and $K_d(\lambda)$ were collected seasonally in the northern Gulf of Mexico (GulfCarbon cruises, 2009–2010), around the Mackenzie River outflow (MALINA cruise, August 2009), and the Gulf of Maine in 2008 (Figure 2.7). The measured *in situ* $K_d(\lambda)$ in the validation data set cover different water types and span almost the same wide range as the data used to parameterize the composite algorithms (e.g. for $K_d(380)$, the measured values span from 0.04 m^{-1} to 11.22 m^{-1}).

The validation procedure for the composite algorithms was carried out in two steps. First, the original Sea*UV*/Sea*UVc* set was implemented on the $R_{rs}(\lambda)$ of samples with *in situ* $K_d(490) <$ 0.32 m^{-1}. The inshore-water optimized Sea*UV*/Sea*UVc* set was then implemented on the $R_{rs}(\lambda)$ of waters defined as optically complex, that is with *in situ* $K_d(490) > 0.32$ m^{-1}. The $R_{rs}(\lambda)$ data were used as input for the composite Sea*UV*/Sea*UVc* algorithms and the calculated K_d values were then compared with measured K_d values for performance assessment.

Figure 2.8 shows the results for comparisons between calculated K_d derived from the composite Sea*UV*/Sea*UVc* algorithms and measured *in situ* K_d at $\lambda = 340$, 380 and 412 nm for the validation data set. Figure 2.9 shows the error analysis for our K_d retrievals associated with the composite Sea*UV*/Sea*UVc* algorithms, indicating good performance at all wavelengths for the validation data set. For $K_d(412)$, the mean relative error derived from the composite Sea*UVc* model is 16% for the validation data set, compared with 16.4% for our complete training data set. The consistent error distribution between the validation and training data set further confirms that the inshore-water optimized Sea*UV*/Sea*UVc* algorithms were well parameterized for higher K_d retrieval in optically complex inshore waters. It is important to note that while the inshore-water optimized Sea*UV*/Sea*UVc* model was developed using AOPs collected along coastal Georgia, these calculations also performed well for K_d retrieval in other inshore waters from diverse locations. The results from the independent *in situ* validation data set demonstrate that inshore-water optimized Sea*UV*/Sea*UVc* may be relatively insensitive to the spatial variation of optical properties. It should also be noted here that the attenuation values for the validation data fall within the range used to parameterize the inshore-water optimized Sea*UV*/Sea*UVc* algorithms (e.g. the western branch of the Mackenzie River and Gulf of Maine, with $K_d(340) \sim 17.0\ \mathrm{m}^{-1}$). The good performance for calculations of optically complex water K_d, together with the fact that composite algorithms were parameterized based on a complete training data set that covered an extremely wide range of K_d values, indicate the potential for use of the composite algorithms in K_d retrieval varying from open ocean waters to optically complex inshore waters on a global scale.

3.6. Optimized composite Sea*UV* algorithms

In light of the empirical nature of the composite Sea*UV*/Sea*UVc* algorithms, the composite algorithms can always be updated using additional data in order to further improve the accuracy of K_d retrievals. Here, the original training and *in situ* validation data sets used by Fichot et al. (2008), and the inshore-water and *in situ* validation data sets compiled for this study were pooled together and used to parameterize a final set of Sea*UV*/Sea*UVc* algorithms. This final set of Sea*UV* algorithms is referred to here as the "optimized composite Sea*UV* algorithms". The parameters associated with this set of algorithms were derived from a data set that covers water types ranging from very oligotrophic open ocean water to optically complex inshore locations (N = 563). As shown in Figures 2.10 and 2.11, the optimized composite algorithms performed very well at all wavelengths and performed even better than the algorithms derived from the smaller training data set (N = 438). The optimized result obtained by adding the validation data set to the final pool used to derive the composite algorithms also eliminated the biases that occurred in the earlier validation step. Thus, this final optimization of the composite Sea*UV*/Sea*UVc* model parameters is the best product we can provide for the optical community using this approach. A complete scheme of how the optimized composite algorithms should be implemented is provided in Appendix A.

3.7. Application to SeaWiFS satellite imagery

The optimized composite Sea*UV* algorithm was implemented using SeaWiFS R_{rs} in order to test its applicability with satellite imagery. The monthly climatology of SeaWiFS *Rrs* over the Northern Gulf of Mexico (nGoM) for April 1998-2010 (Level-3, binned 9 x9 km spatial resolution) were acquired from the NASA ocean color project website (http://oceancolor.gsfc.nasa.gov) and used in this application. The nGoM was chosen because it encompasses oligotrophic waters as well as turbid, high CDOM waters influenced by the

Mississippi/Atchafalaya River plumes (Lohrenz et al., 1999), thus making it a suitable area to demonstrate the overall performance of the optimized composite Sea*UV* algorithms over a wide range of K_d values. Both the original and final optimized composite Sea*UV* algorithms were applied to the SeaWiFS climatological R_{rs} data to derive K_d (noted as $K_d^{original}$ and $K_d^{composite}$ respectively in the following text). For additional comparison, we applied the Jamet et al. (2012) neural network inversion algorithms (hereafter K_d^{NN}), also tuned for retrieving K_d (K_d^{NN}) in both open ocean and optically complex waters, to the same SeaWiFS *Rrs*.

Figure 2.12 shows the climatology images for comparison. As expected, K_d derived with the original Sea*UV* algorithm (Figures 2.12 (a) & (d)) displays less variability between the clear offshore Gulf water and waters near the river mouth. However, the images derived using the optimized composite Sea*UV* algorithm (Figures 2.12 (b) & (e)) show distinct K_d characteristics when applied to different water types, especially in nearshore areas. For $K_d(320)$, the difference in the images derived using original and optimized composite Sea*UV* algorithms can be as large as 100% (Figure 2.12 (c)). Because K_d^{NN}can only be retrieved at visible wavelengths, we generated images at $K_d(412)$ for $K_d^{composite}$ and K_d^{NN} (Figure 2.12 (f)) for comparison. $K_d^{NN}(412)$ showed similar patterns overall, but generated slightly higher values than $K_d^{composite}(412)$ for nearshore waters. While $K_d(412)$ is somewhat useful for examining waters with high CDOM content, the distinct advantage of our composite Sea*UV* algorithms is its ability to retrieve K_d in the UV directly from R_{rs}, and in doing so provide essential data for evaluating photochemical production and photobiological reactions in the surface ocean.

4. Summary and Conclusions

This study makes two contributions to the ocean optical community with by providing improved capacity to retrieve K_d from the most oligotrophic open ocean waters to dynamic inshore systems. First, it re-parameterized the original Sea*UV*/Sea*UVc* algorithms by pooling a new training data set collected in optically complex waters to achieve greatly improved accuracy of $K_d(\lambda)$ retrieval at λ = 320, 340, 380, 412, 443 and 490 nm for turbid coastal waters from ocean color ($R_{rs}(\lambda)$ at SeaWiFS bands, with wavebands centered at λ = 412, 443, 490, 510, 555 and 670 nm). Second, it updated the parameters defined and reported in the original Sea*UV*/Sea*UVc* by using an expanded training data set. The optimization of the original algorithm further enhanced the K_d retrieval accuracy in almost all oceanic and coastal waters. The utilization of such a large training data set that includes an extensive range of K_d values, together with the inherent advantage of the statistical methods employed in developing these algorithms, results in a final Sea*UV*/Sea*UVc* product (namely, the "optimized composite Sea*UV*/Sea*UVc* algorithms") that is suitable for retrieval of K_d over large spatial scales, and in almost any water type.

While good accuracy in retrieving K_d was obtained using optimized composite algorithms, several cautionary notes regarding the shortcomings associated with the methodologies should be made for readers who wish to apply these algorithms on ocean color data. First, as mentioned earlier, PCA and cluster analysis are purely statistical (empirical) approaches, thus, neither categorizes water types beforehand nor excludes samples from non-ideal situations (i.e. bottom reflectance, turbidity, algal blooms, etc.), Sea*UV*/Sea*UVc* is designed only to retrieve K_d in the UV based on PCA and cluster analysis. Neither of these statistical approaches requires or, in fact allows underlying assumptions on the spectral data used for the analysis. Interpreting the resulting PC curves or optical domains beyond the design of the model requires speculation that we do not always have auxiliary data to support. Although the training data set (N = 563) used to derive the algorithm parameters accommodated as much spatial and temporal variations, in waters where ocean color variability had not been incorporated yet, uncertainties may likely increase. For example, without including data in our training model such as that from the Biogeochemistry and Optics South Pacific Experiment (BIOSOPE) which described the clearest oceanic water in the South Pacific subtropical gyre (Morel et al., 2007a, 2007b), our model may underperform in this specific area. Second, it should be noted that the PCs, although together can best describe the original data, each PC may not necessarily be linearly correlated to one specific inherent optical property (IOP), as pointed out by Toole and Siegel (2001). In the framework of linear algebra, PCA *per se*, only retains the linearity in the training data set, and may not rigorously describe the physical relationship between R_{rs} and IOPs (Morel, 1998; Mueller, 1976). It remains unknown on the predictability of Sea*UV*/Sea*UVc* algorithms of non-linearities between ocean color and IOPs. Third, readers should be aware that K_d is one of the AOPs and varies with sun elevation, and this variation was captured implicitly by PCA. Most of the data in the training data set were collected with SZA between 0º and 45º, with a few cases occurred with SZA greater than 60º. Sea*UV*/Sea*UVc* should be used with caution when SZA falls beyond this range.

With the advent of new remote-sensing technologies and the focus on coastal ocean processes, the composite Sea*UV*/Sea*UVc* algorithms will find applicability for the retrieval of K_d in turbid coastal waters using instruments such as the Hyperspectral Imager for the Coastal Ocean (HICO) (Gitelson et al., 2011; Lucke et al., 2011), the Visible Infrared Imager Radiometer Suite (VIIRS), or the Portable Remote Image Spectrometer (PRISM). Accurate K_d estimates from ocean color can provide better UV data for calculation of photochemical fluxes in coastal waters and address the role of estuarine and coastal waters in photochemical and biogeochemical processes. In addition, spectral UV distribution in the water column can also be modeled using accurate values of K_d by assuming an exponential decrease of K_d values over increasing wavelengths if surface downwelling irradiance is known (Markager et al., 2000; Kjeldstad et al., 2003). These depth profiles are important for quantitative evaluation of UVR inhibition of photosynthesis, bacterial production (Ogbebo and Ochs, 2008) and viral growth (Fuhrman and Noble, 1995) in ecological studies. These algorithms can help to clarify and assess possible effects of UVR in different trophic levels (Yuan et al., 2011) and in important biogeochemical processes occurring in optically complex waters.

Acknowledgements

This work was funded by grants from the Office of Naval Research (N00140610219), NASA (NNX07AD85G) and Georgia Sea Grant (R/SD-5) awarded to Dr. W. L. Miller. Validation data from the Gulf of Mexico were collected by C. Fichot and S. Lohrenz during the GulfCarbon cruises (2009-2010), funded by NSF (OCE- 0752254), and an NSF award to Drs. R. Benner and W. L. Miller (OCE-0850677). We thank Leanne Powers and Joanna Green, as well as Ike Sellers, Mary Price, and Jason Johnson (UGA Marine Institute) for assistant with sampling aboard the R/V Mud Minnow in coastal Georgia. We thank NASA for providing access to SeaWiFS data. SeaWiFS data were used in accordance with the SeaWiFS data access authorization policy. We also thank Dr. Adrian Burd for valuable suggestions on earlier versions of the draft. Finally, we thank three anonymous reviewers for careful reviews of this manuscript.

References

Austin, R. W. (1974). The Remote Sensing of Spectral Radiance from below the Ocean Surface. In N. G. Jerlov (Ed.) *Optical aspects of oceanography* (pp. 317-344). London, Academic Press.

Austin, R. W., & Petzold, T. J. (1981). The determination of the diffuse attenuation coefficient of sea water using the Coastal Zone Color Scanner. In J. F. R. Grower (Ed.), *Oceanography from space* (pp. 239-256). New York: Plenum Press.

Booth, C. R., & Morrow, J. H. (1997). The penetration of UV into natural waters. Photochemistry and Photobiology, 65(2), 254-257.

Craft, C. (2007). Freshwater input structures soil properties, vertical accretion, and nutrient accumulation of Georgia and US tidal marshes. Limnology and Oceanography, 52(3), 1220-1230.

Fichot, C. G., Sathyendranath, S., & Miller, W. L. (2008). SeaUV and SeaUVc: Algorithms for the retrieval of UV/Visible diffuse attenuation coefficients from ocean color. *Remote Sensing of Environment*, *112*(4), 1584-1602.

Fichot, C. G., & Miller, W. L. (2010). An approach to quantify depth-resolved marine photochemical fluxes using remote sensing: application to carbon monoxide (CO) photoproduction. *Remote Sensing of Environment*, *114*(7), 1363-1377.

Fuhrman, J. A., & Noble, R. T. (1995). Viruses and protists cause similar bacterial mortality in coastal seawater. *Limnology and Oceanography*, *40*(7), 1236-1242.

Gitelson, A. A., Gao, B. C., Li, R. R., Berdnikov, S., & Saprygin, V. (2011). Estimation of chlorophyll-a concentration in productive turbid waters using a Hyperspectral Imager for the Coastal Ocean—the Azov Sea case study. *Environmental Research Letters*, *6*(2), 024023.

Gordon, H. R. (1989). Can the Lambert-Beer law be applied to the diffuse attenuation coefficient of ocean water? *Limnology and Oceanography*, *34*(8), 1389-1409.

Jamet, C., Loisel, H., & Dessailly, D. (2012). Retrieval of the spectral diffuse attenuation coefficient $K_d(\lambda)$ in open and coastal ocean waters using a neural network inversion. *Journal of Geophysical Research*, *117*, C10023, doi: 10.1029/ 2012JC008076.

Johannessen, S. C., Miller, W. L., & Cullen, J. J. (2003). Calculation of UV attenuation and colored dissolved organic matter absorption spectra from measurements of ocean color. *Journal of Geophysical Research*, *108*(C9), 3301, doi: 10.1029/2000JC000514.

Kirk, J. T. O. (1994a). *Light and photosynthesis in aquatic ecosystems*, 2nd Edition. New York, NY, USA: Cambridge University Press.

Kjeldstad, B., Frette, Ø., Erga, S. R., Browman, H. I., Kuhn, P., Davis, R., Miller, W. L., & Stamnes, J. J. (2003). UV (280 to 400 nm) optical properties in a Norwegian fjord system and an intercomparison of underwater radiometers. *Marine Ecology Progress Series*, *256*, 1-11.

Kuhn, P., Browman, H., McArthur, B., & St-Pierre, J. F. (1999). Penetration of ultraviolet radiation in the waters of the estuary and Gulf of St. Lawrence. *Limnology and Oceanography*, *44*(3), 710-716.

Laurion, I., Vincent, W. F., & Lean, D. R. (1997). Underwater ultraviolet radiation: Development of spectral models for northern high latitude lakes. *Photochemistry and Photobiology*, *65*(1), 107-114.

Lee, Z., Du, K., Arnone, R., Liew, S., & Penta, B. (2005). Penetration of solar radiation in the upper ocean: A numerical model for oceanic and coastal waters. *Journal of Geophysical Research, 110*, C09019. doi:10.1029/2004JC002780.

Lohrenz, S. E., Fahnenstiel, G. L., Redalje, D. G., Lang, G. A., Dagg, M. J., Whitledge, T. E., & Dortch, Q. (1999). Nutrients, irradiance, and mixing as factors regulating primary production in coastal waters impacted by the Mississippi River plume. *Continental Shelf Research*, *19*(9), 1113-1141.

Lucke, R. L., Corson, M., McGlothlin, N. R., Butcher, S. D., Wood, D. L., Korwan, D. R., Li, R. R., Snyder, W. A., Davis C. O., & Chen, D. T. (2011). Hyperspectral Imager for the Coastal Ocean: instrument description and first images. *Applied Optics*, *50*(11), 1501-1516.

Markager, S., & Vincent, W. F. (2000). Spectral light attenuation and the absorption of UV and blue light in natural waters. *Limnology and Oceanography*, *45*(3), 642-650.

Moore, T. S., Campbell, J. W., & Feng, H. (2001). A fuzzy logic classification scheme for selecting and blending satellite ocean color algorithms. *IEEE Transactions on Geoscience and Remote Sensing*, *39*(8), 1764-1776.

Moore, T. S., Campbell, J. W., & Dowell, M. D. (2009). A class-based approach to characterizing and mapping the uncertainty of the MODIS ocean chlorophyll product. *Remote Sensing of Environment*, *113*(11), 2424-2430.

Mopper, K., & Kieber, D. J. (2000). Marine photochemistry and its impact on carbon cycling. *The effects of UV radiation in the marine environment*. In S. de Mora, S. Demers & M. Vernet (Eds.), *The Effects of UV Radiation in the Marine Environment* (pp. 101-129). Cambridge University Press, Cambridge, UK.

Morel, A. (1998). Minimum requirements for an operational ocean-colour sensor for the open ocean. *IOCCG Report, Vol. 1*. Dartmouth, Nova Scotia: IOCCG Project Office, 46 pp.

Morel, A., Claustre, H., Antoine, D., & Gentili, B. (2007a). Natural variability of bio-optical properties in Case 1 waters: attenuation and reflectance within the visible and near-UV spectral domains, as observed in South Pacific and Mediterranean waters. *Biogeosciences Discussions, 4*(4), 2147-2178.

Morel, A., Gentili, B., Claustre, H., Babin, M., Bricaud, A., Ras, J., & Tieche, F. (2007b). Optical properties of the" clearest" natural waters. *Limnology and Oceanography, 52*(1), 217-229.

Mueller, J. L. (1976). Ocean color spectra measured off the Oregon coast: characteristic vectors. *Applied Optics, 15*(2), 394-402.

Mueller, J. L. (2000). SeaWiFS algorithm for the diffuse attenuation coefficient, K(490), using water-leaving radiances at 490 and 555 nm. In S. B. Hooker & E. R. Firestone (Eds.), SeaWiFS postlaunch calibration and validation analysis: Part 3. *NASA Tech. Memo. 2000-206892, Vol. 11* (pp. 24−27) Greenbelt, Maryland: NASA Goddard Space Flight Center.

Ogbebo, F. E., & Ochs, C. (2008). Bacterioplankton and phytoplankton production rates compared at different levels of solar ultraviolet radiation and limiting nutrient ratios. *Journal of Plankton Research, 30*(11), 1271-1284.

Richardson, L. L., & LeDrew, E. F. (Eds.). (2006). *Remote sensing of aquatic coastal ecosystem processes: science and management applications* (*Vol. 9. Remote sensing and digital image processing)*. Dordrecht, Springer. (pp. 57).

Sinha, R. P., & Häder, D. P. (2002). UV-induced DNA damage and repair: a review. *Photochemical & Photobiological Sciences, 1*(4), 225-236.

Tedetti, M., & Sempéré, R. (2006). Penetration of ultraviolet radiation in the marine environment. A review. *Photochemistry and Photobiology, 82*(2), 389-397.

Tedetti, M., Sempéré, R., Vasilkov, A., Charrière, B., Nérini, D., Miller, W. L., Kawamura, K., & Raimbault, P. (2007). High penetration of ultraviolet radiation in the south east Pacific waters. *Geophysical Research Letters, 34*, L12610, doi:10.1029/2007GL029823.

Thuillier, G., Hersé, M., Foujols, T., Peetermans, W., Gillotay, D., Simon, P. C., & Mandel, H. (2003). The solar spectral irradiance from 200 to 2400 nm as measured by the SOLSPEC spectrometer from the ATLAS and EURECA missions. *Solar Physics, 214*(1), 1-22.

Toole, D. A., & Siegel, D. A. (2001). Modes and mechanisms of ocean color variability in the Santa Barbara Channel. *Journal of Geophysical Research, 106*, 26,985-27,000.

Wang, M., Son, S., & Harding, L. W. (2009). Retrieval of diffuse attenuation coefficient in the Chesapeake Bay and turbid ocean regions for satellite ocean color applications. *Journal of Geophysical Research, 114*, C10011, doi:10.1029/2009JC005286.

Werdell, P. J. (2009). Diffuse attenuation coefficient (K_d) for downwelling irradiance at 490-nm. http://oceancolor.gsfc.nasa.gov/REPROCESSING/R2009/kdv4/.

Whitehead, R. F., de Mora, S. J., & Demers, S. (2000). Enhanced UV radiation—a new problem for the marine environment. In S. de Mora, S. Demers & M. Vernet (Eds.), *The Effects of UV Radiation in the Marine Environment* (pp. 1-34). Cambridge University Press, Cambridge, UK.

Witte, W. G., Whitlock, C. H., Harriss, R. C., Usry, J. W., Poole, L. R., Houghton, W. M., Morris, W. D., & Gurganus, E. A. (1982). Influence of dissolved organic materials on turbid water optical properties and remote-sensing reflectance. *Journal of Geophysical Research*, *87*(C1), 441-446.

Yuan, X., Yin, K., Harrison, P. J., & Zhang, J. (2011). Phytoplankton are more tolerant to UV than bacteria and viruses in the northern South China Sea. *Aquatic Microbial Ecology*, *65*(2), 117-128.

Table 2.1: Sampling information of the data used in this study (N=438)

Location	Date	No. of samples
UCSB/Dalhousie dataset	1996-2002	333
South Atlantic Bight (SAB)	May 2006	15
SOLAS Autumn Cruise (SABINA)	2003	4
Mid-Atlantic Bight (MAB)/Gulf of Maine	July 2002	12
coastal Georgia	2006-2011	74

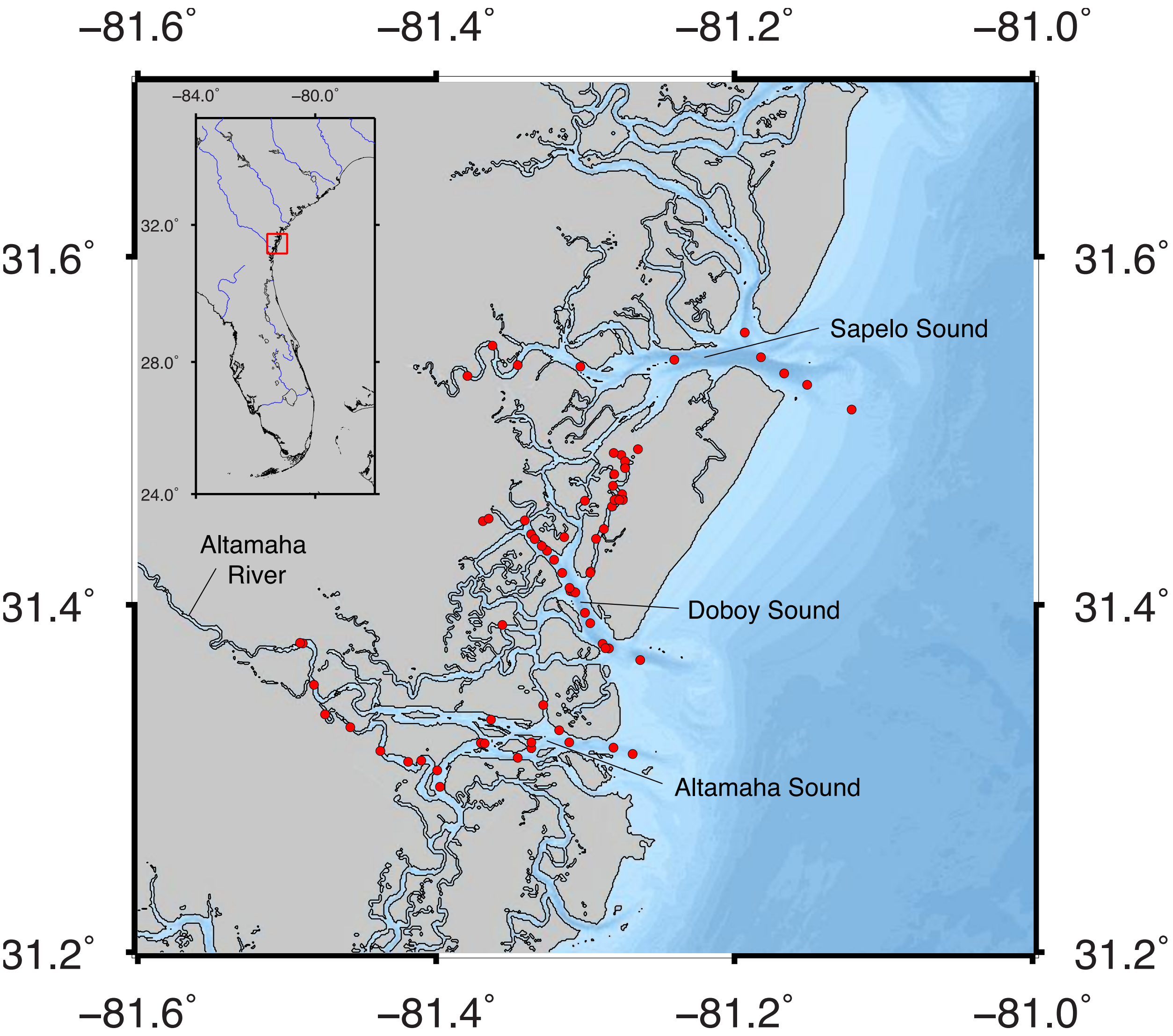

Figure 2.1: Map of optically complex inshore waters sampled along coastal Georgia during 2006 - 2011. The coastline data was downloaded from the NOAA National Geophysical Data Center (http://www.ngdc.noaa.gov/mgg/shorelines/shorelines.html).

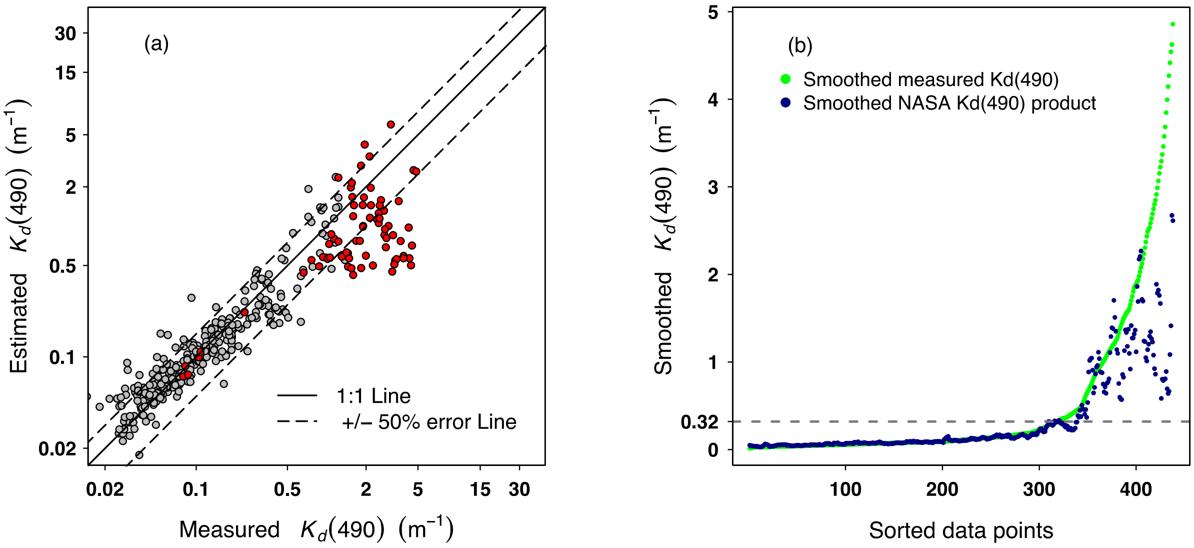

Figure 2.2: Determination of the cutoff point for the inshore water optimized Sea*UV*/Sea*UVc* algorithms. (a) Performance of the latest NASA $K_d(490)$ product on the complete training data set. Filled red circles mark K_d collected along coastal Georgia and gray circles represent K_d published by Fichot et al. (2008). (b) Smoothed results from the five-point moving-average function applied to measured *in situ* K_d data (filled green circles) and modeled K_d derived from the latest NASA $K_d(490)$ product (filled blue circles), respectively. The x-axis represents the data points sorted in ascending order (N = 438) based on measured *in situ* $K_d(490)$. The y-axis represents corresponding smoothed $K_d(490)$ values.

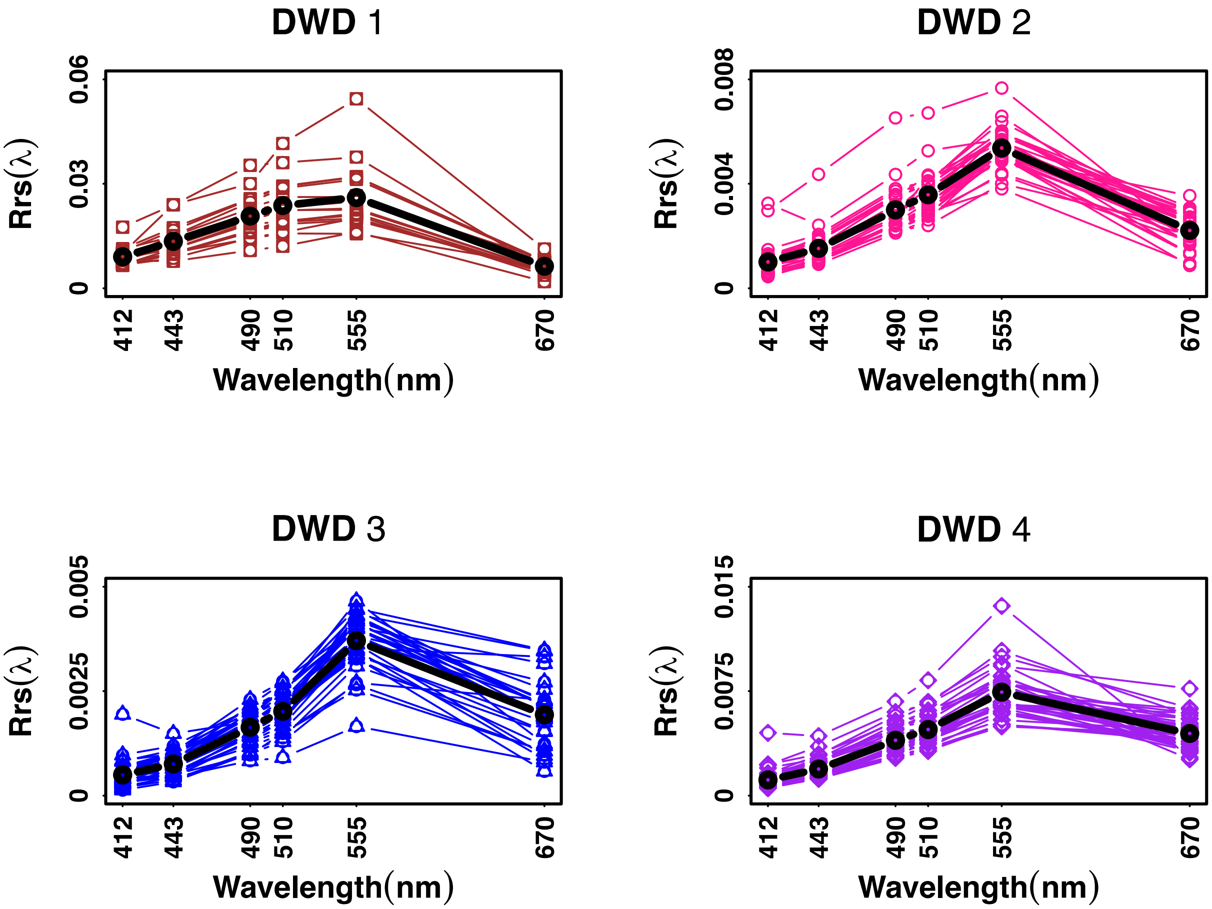

Figure 2.3: Remote sensing reflectance spectra (R_{rs}) in the four statistically determined dark water domains (DWDs). The spectra in black represents the mean R_{rs} values for each dark water domain.

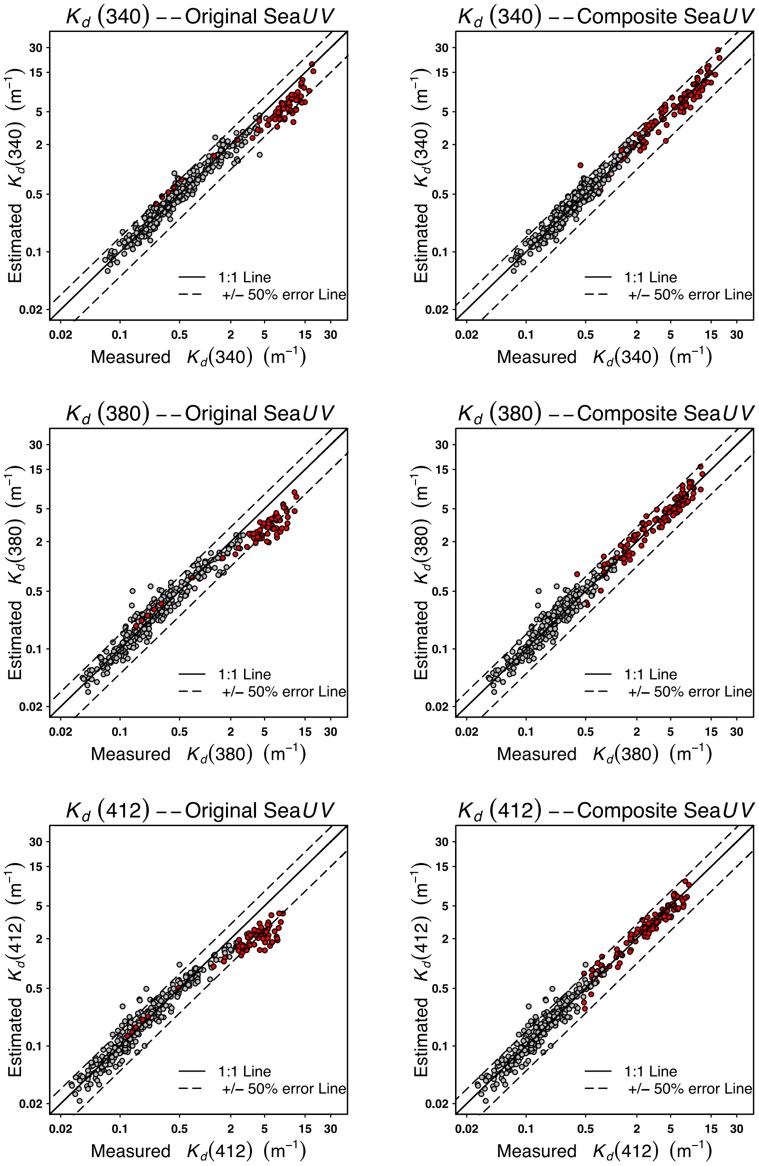

Figure 2.4: Comparisons of measured *in situ* K_d with calculated K_d derived from original Sea*UV* and composite Sea*UV* algorithms at λ = 340, 380 and 412 nm. In the panels at the left, filled red circles (*N* = 74) mark K_d collected along the Georgia coast and gray circles (*N* = 364) denote K_d published in Fichot et al (2008). In the panels on the right, filled red circles (*N* = 119) represent the inshore water training data set (*N* = 119) split from the complete training data set and gray circles represent all data collected not in the inshore water training data set.

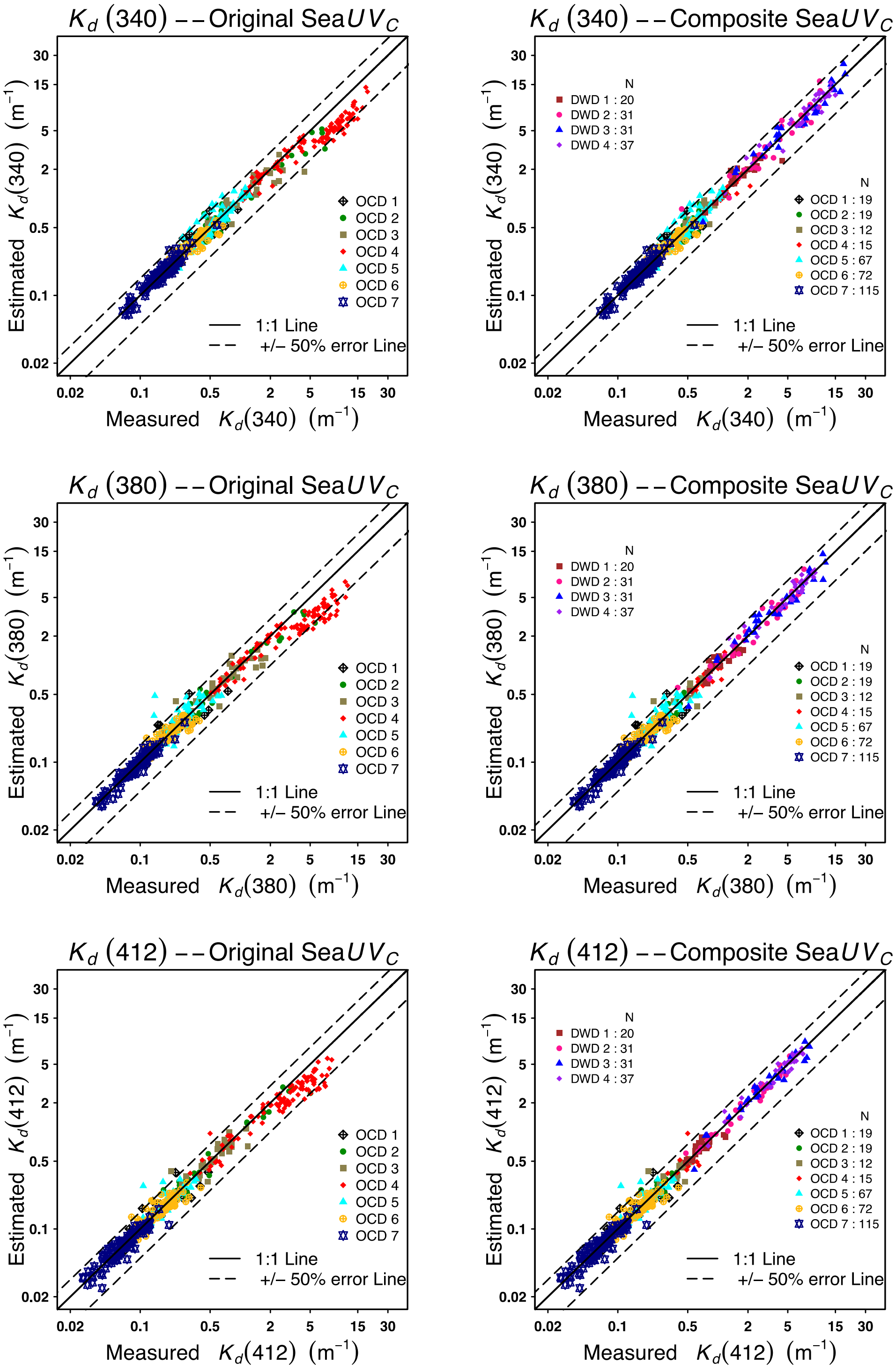

Figure 2.5: Comparisons of measured *in situ* K_d with calculated K_d derived from original Sea*UVc* and composite Sea*UVc* algorithms at λ = 340, 380 and 412 nm.

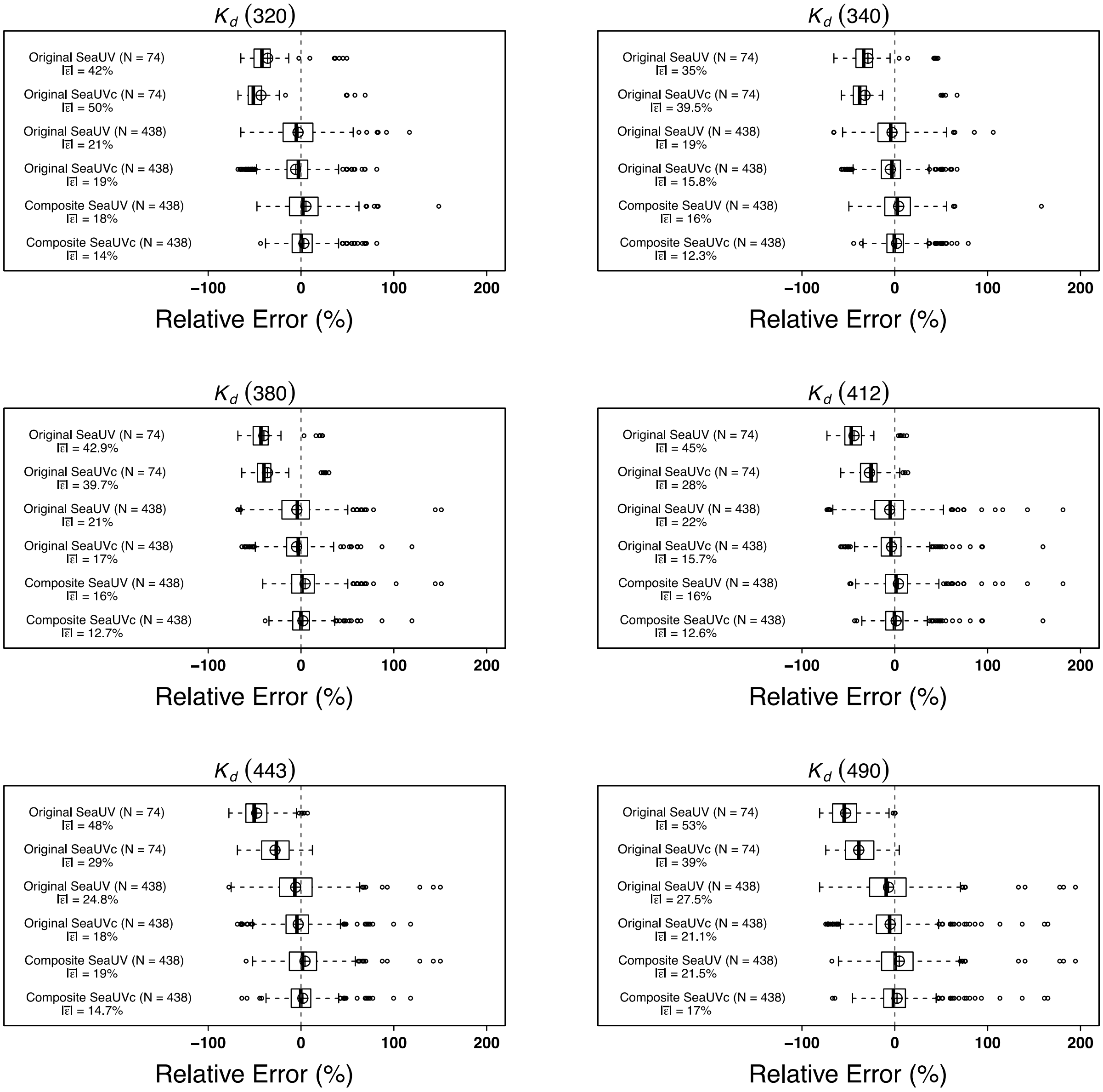

Figure 2.6: Box and whisker plots of relative error distribution of K_d derived from the original and composite Sea*UV*/Sea*UVc* algorithms at λ = 320, 340, 380, 412, 443 and 490 nm for the inshore data set collected in this study (N = 74) and complete training data set (N = 438). The circle plus symbol in each boxplot represents the mean relative error (MRE, $|\bar{\varepsilon}|$).

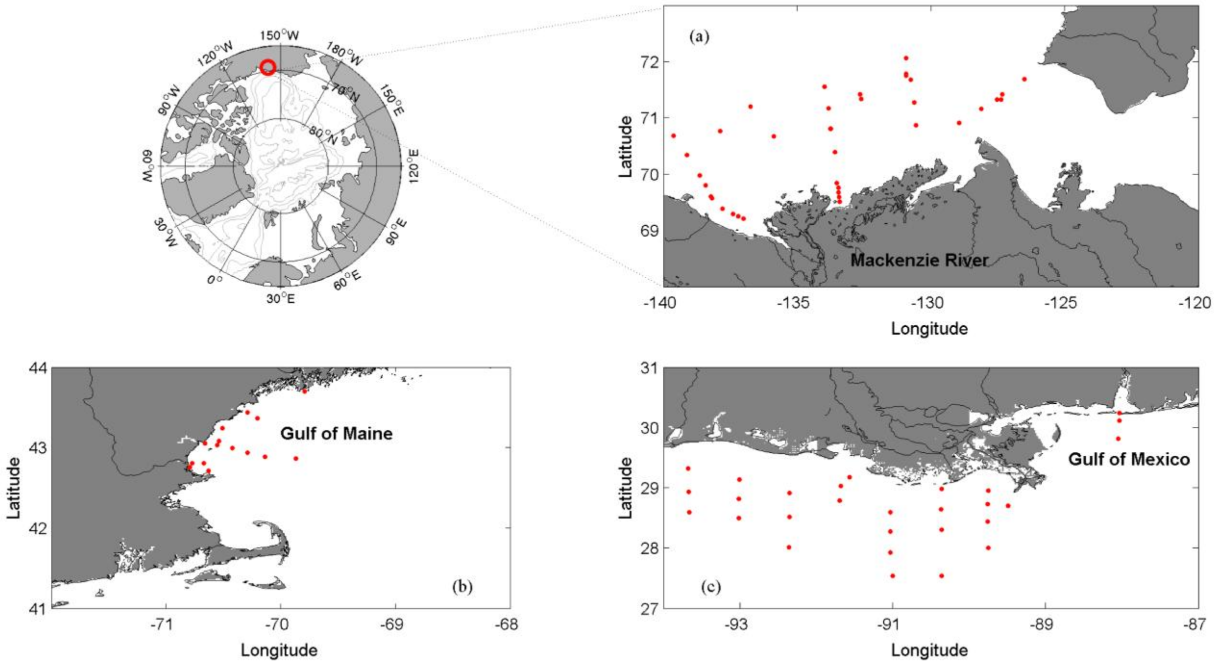

Figure 2.7: Locations of stations for *in situ* paired AOP data used as the validation data set (N = 125): (a) Mackenzie River outflow during the MALINA cruise, (b) Gulf of Maine, and (c) Northern Gulf of Mexico (collected during five GulfCarbon cruises).

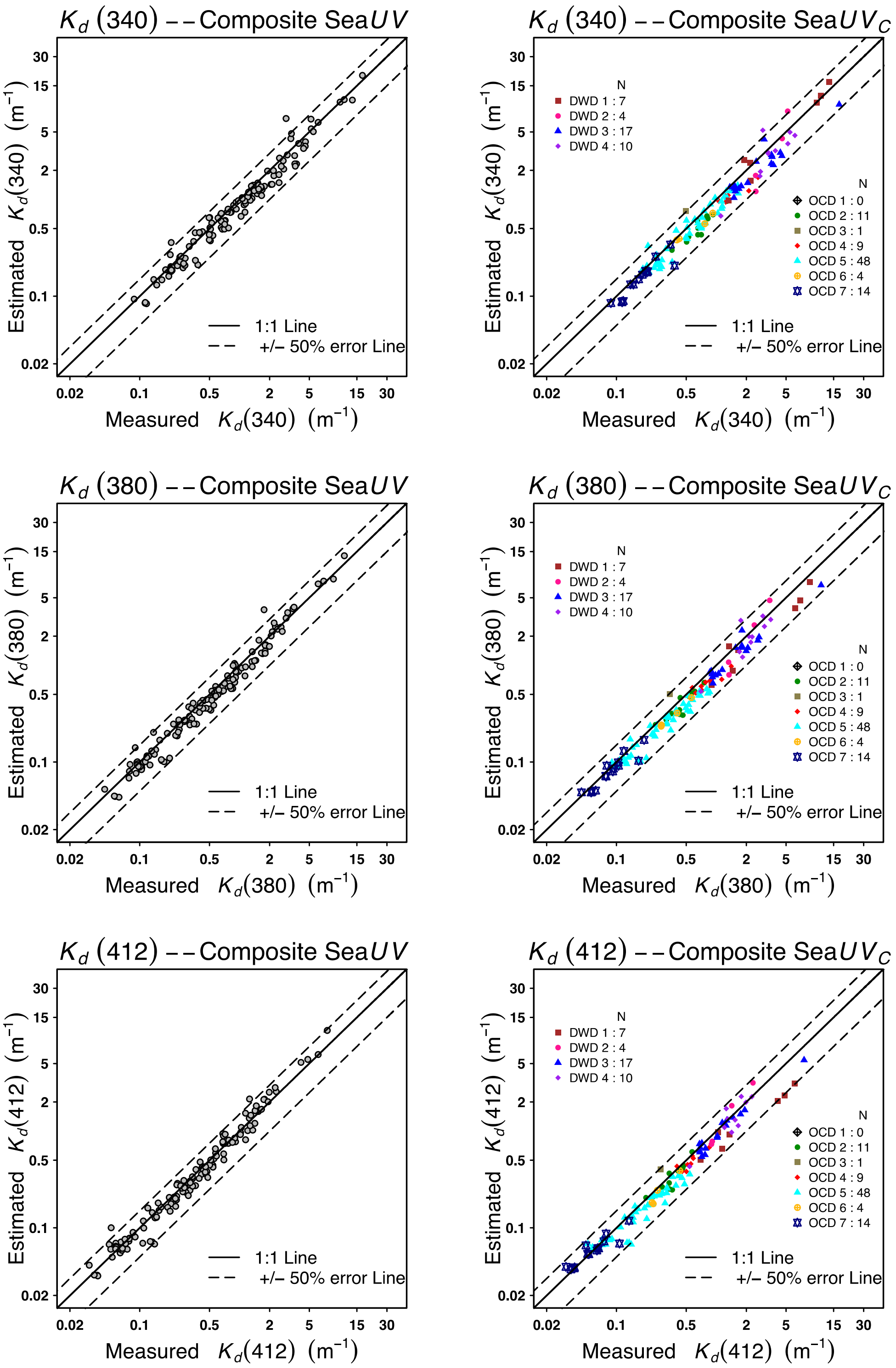

Figure 2.8: Comparisons of measured *in situ* K_d with calculated K_d derived from the composite Sea*UV*/Sea*UVc* algorithms at λ = 340, 380 and 412 nm for the *in situ* validation data set (N = 125).

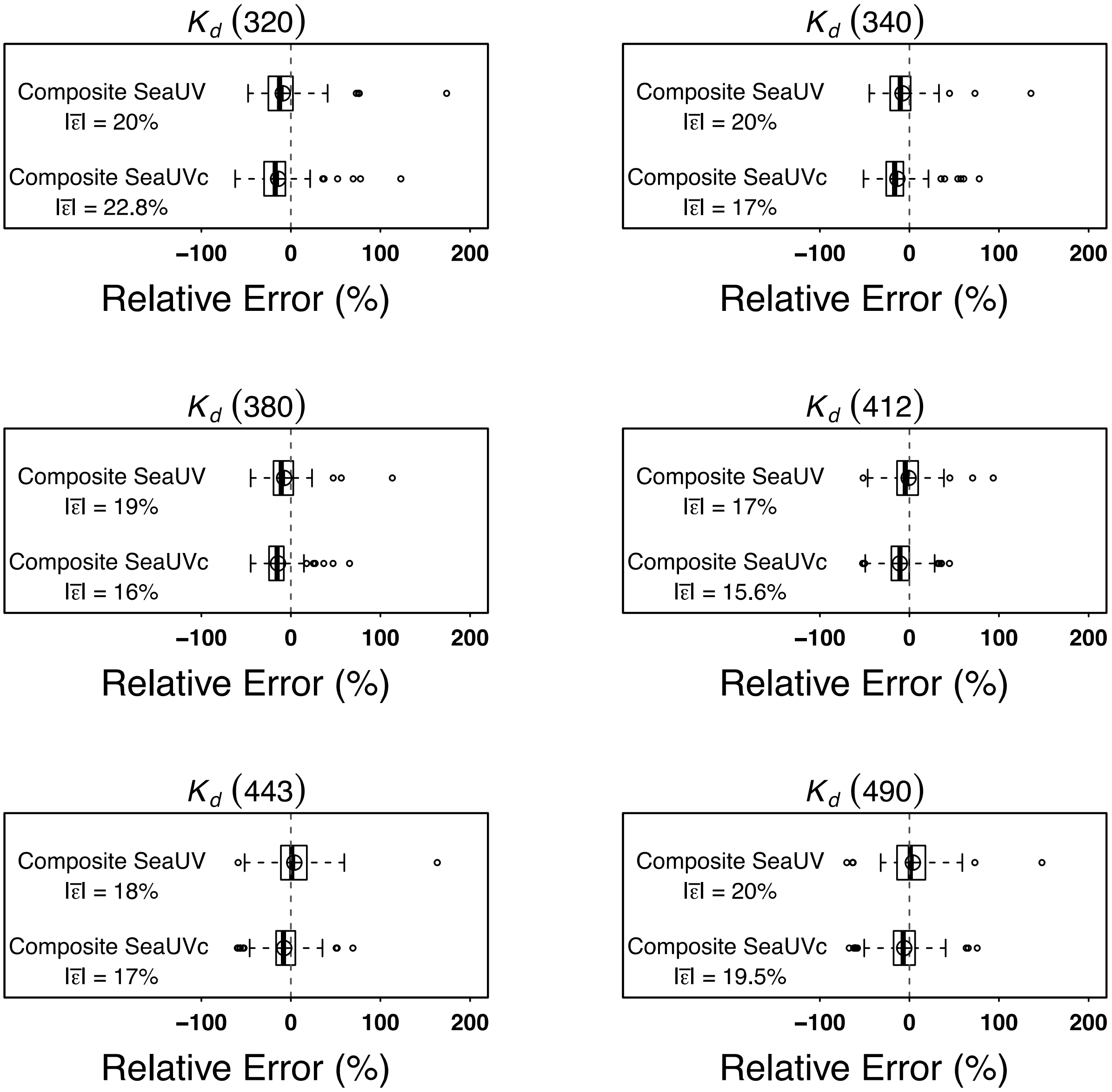

Figure 2.9: Box and whisker plots of relative error distribution of K_d derived from the composite Sea*UV*/Sea*UVc* at λ = 320, 340, 380, 412, 443 and 490 nm for the *in situ* validation data set (*N* = 125). Symbols are the same as in Figure 2.6.

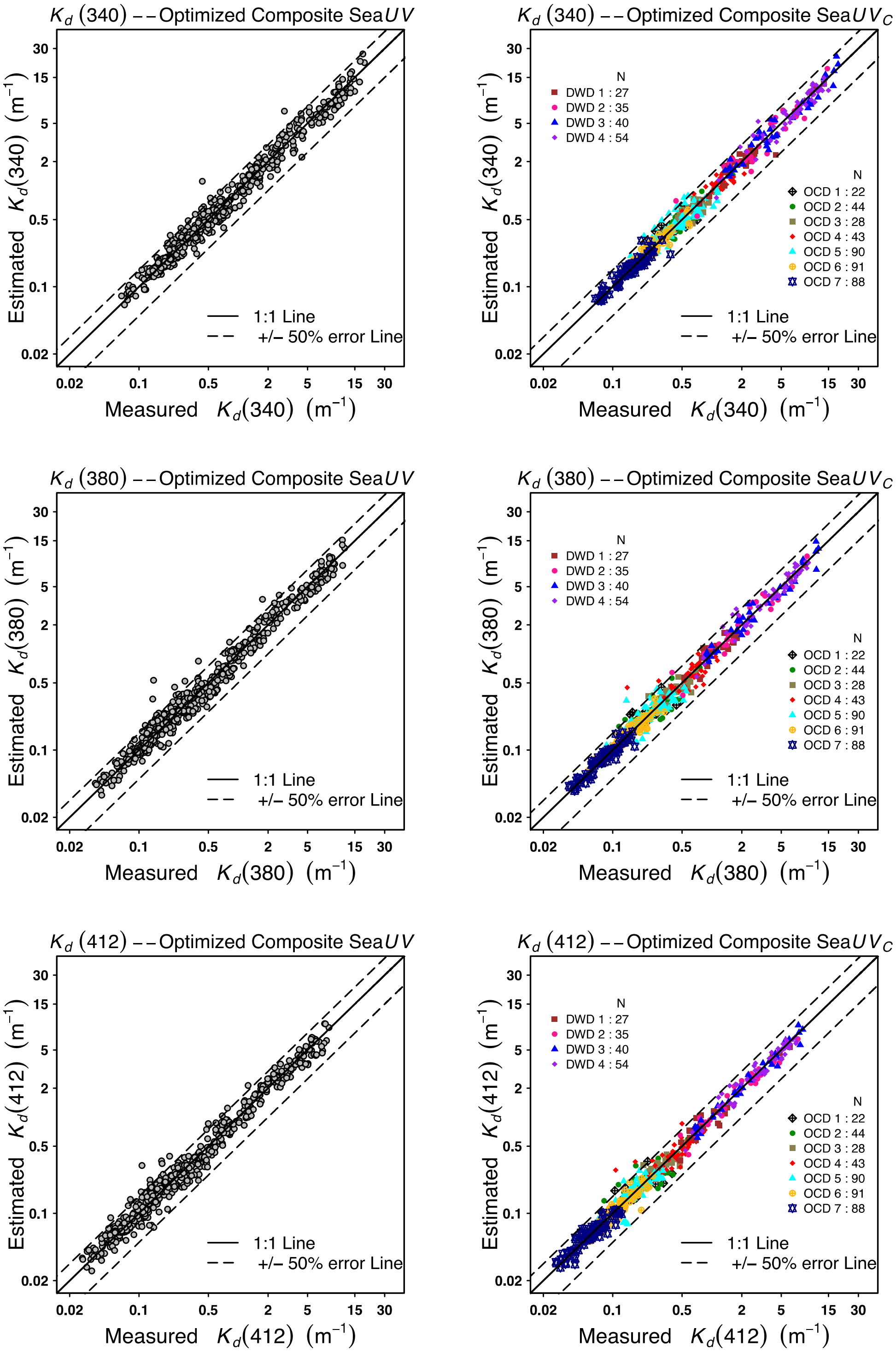

Figure 2.10: Comparisons of measured *in situ* K_d with calculated K_d derived from the optimized composite Sea*UV*/Sea*UVc* algorithms at λ = 340, 380 and 412 nm for the large training data set (N = 563).

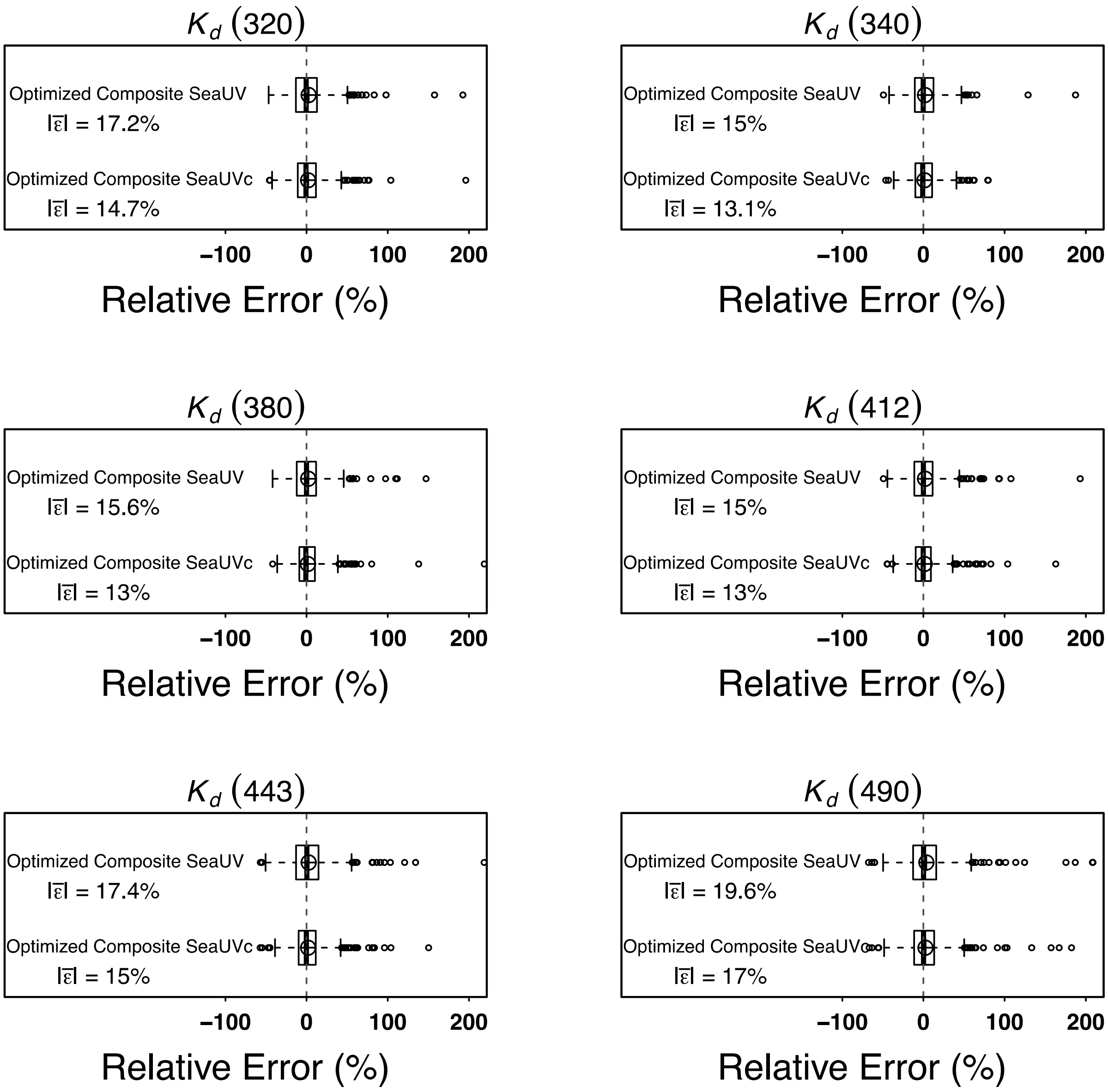

Figure 2.11: Box and whisker plots of relative error distribution of K_d derived from the optimized composite Sea*UV*/Sea*UVc* at λ = 320, 340, 380, 412, 443 and 490 nm for the large training data set (N = 563). Symbols are the same as in Figure 2.6.

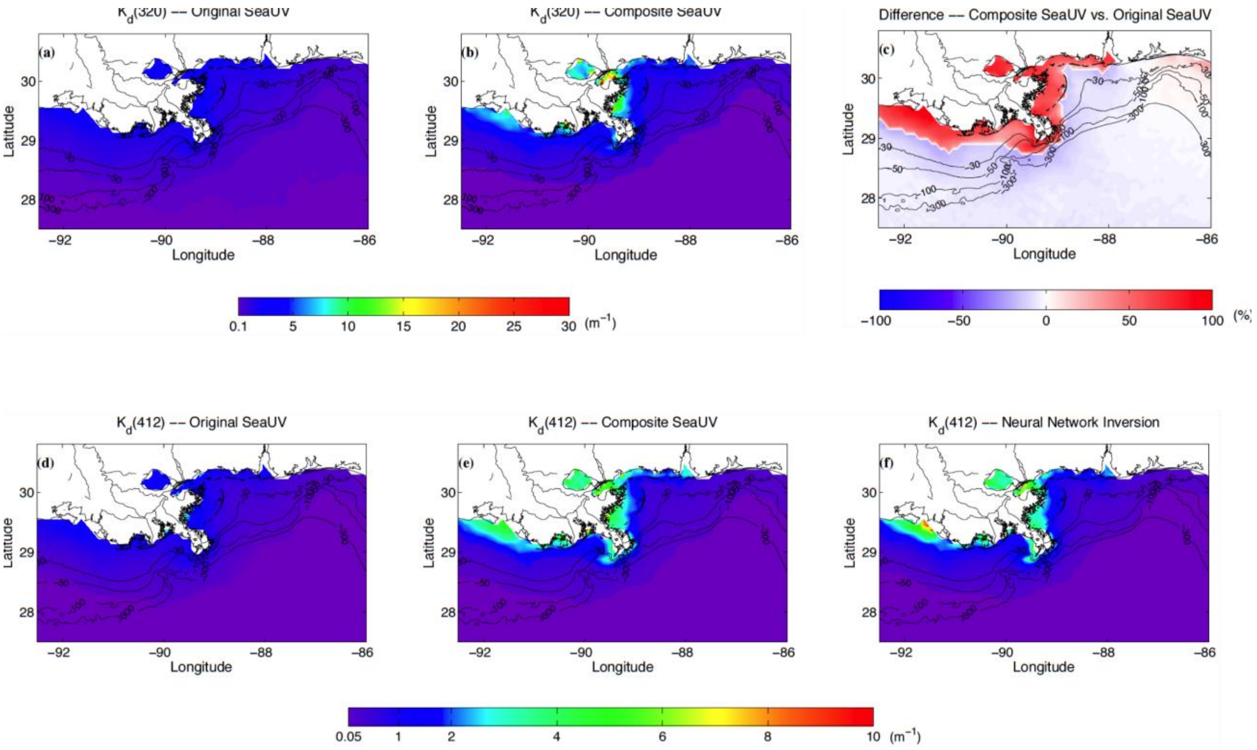

Figure 2.12: April climatology (in the period from 1998 to 2010) of $K_d(320)$ and $K_d(412)$ (m^{-1}) derived from SeaWiFS satellite images for the northern Gulf of Mexico using (a) the original Sea*UV* algorithm as published by Fichot et al. (2008) for $K_d(320)$, (b) the optimized composite Sea*UV* algorithm developed in this study for $K_d(320)$, (c) the difference between the optimized composite Sea*UV* and the original Sea*UV* algorithms for $K_d(320)$, the difference was calculated as $\frac{(K_d^{compositeSeaUV} - K_d^{originalSeaUV})}{(K_d^{compositeSeaUV} + K_d^{originalSeaUV})/2}$, (d) the original Sea*UV* algorithm as published by Fichot et al. (2008) for $K_d(412)$, (e) the optimized composite Sea*UV* algorithm developed in this study for $K_d(412)$ and (f) the neural network inversion method developed by Jamet et al. (2012) for $K_d(412)$. The bathymetry and coastline data was downloaded from the NOAA National Geophysical Data Center (http://www.ngdc.noaa.gov/mgg/bathymetry/relief.html and http://www.ngdc.noaa.gov/mgg/shorelines/shorelines.html).

CHAPTER 3

A NEW ALGORITHM TO RETRIEVE CHROMOPHORIC DISSOLVED ORGANIC MATTER (CDOM) ABSORPTION SPECTRA IN THE UV FROM OCEAN COLOR[3]

---

[3] Cao, F., and W. L. Miller (2014). *Journal of Geophysical Research: Oceans*, 120, 496–516, doi:10.1002/2014JC010241; Reprinted here with the permission of the publisher.

Abstract

Accurate estimation of the absorption coefficient (a_g) for chromophoric dissolved organic matter (CDOM) over ultraviolet (UV) and short visible radiation wavelengths (with λ = 275-450 nm) is crucial to provide a robust assessment of the biogeochemical significance of UV in the global ocean. Using a training data set spanning a variety of water types from the clearest open ocean to dynamic inshore waters, a novel algorithm to accurately resolve CDOM absorption spectra from ocean color is presented. Employing a suite of multivariate statistical approaches (principal component analysis, cluster analysis, and multiple linear regression), this new algorithm was developed with matched field data for CDOM spectra and remote sensing reflectance (R_{rs}) at Sea-viewing Wide Field-of-view Sensor (SeaWiFS) bands. Freed from any presupposition about CDOM spectral shape or conventional spectral extrapolations from visible data, our algorithm allows direct retrieval of a fully resolved CDOM absorption spectrum over UV wavelengths from visible R_{rs}, and further enables a global scale view of the dynamics of CDOM over different water types. Accuracy of a_g retrieval is good, with a mean absolute percent difference for a_g in the UV of ~25%. With fully resolved spectra, maps of calculated CDOM spectral slopes ($S_{275\text{-}295}$, $S_{350\text{-}400}$) and slope ratios (S_R) are presented with the potential to provide new information about the chemical composition (e.g., molecular weight, aromaticity), sources, transformation, and cycling pathways of CDOM on global as well as regional scales. The new algorithm will contribute to improved accuracy for photochemical and photobiological rate calculations from ocean color.

1. Introduction

Chromophoric dissolved organic matter (CDOM), the colored fraction in the total dissolved organic matter (DOM; < 0.2 μm) pool, plays the dominant role in regulating photoprocesses that influence the biogeochemical cycling of DOM in the ocean (Nelson and Siegel 2013; Tedetti and Sempere 2006). Initiated by the absorption of solar ultraviolet radiation (UVR; 280-400 nm), CDOM undergoes a variety of photochemical reactions, including formation of short-lived transit radicals (e.g., $\cdot HO$, $^1O_2$, O_2^-), as well as stable non-radical species that influence the global cycling of trace gases (e.g., CO, CO_2), the redox cycling of essential trace metals (e.g., Fe, Mn, Cu), and production of biologically labile substrates (Blough and Del Vecchio 2002b; Mopper and Kieber 2000b; Zepp et al. 2007a). Photobiological and ecological processes are also directly affected by CDOM and photobleaching reactions which in turn control ultraviolet (UV) penetration depth in the water column, influencing phytoplankton and microbial productivity in marine ecosystems (Del Vecchio and Blough 2006; Kirk 1994). Given its importance, accurate knowledge of the CDOM absorption spectrum throughout the UV wavelengths is a critical determinant for assessing photochemical and photobiological processes in global biogeochemical cycles (Reader and Miller 2011, Swan et al. 2013).

Satellite ocean color algorithms have proven beneficial for retrieving absorption coefficients for CDOM (a_g, Table 3.1) on a synoptic scale. Prediction of a_g from remote sensing reflectance (R_{rs}) via a variety of algorithms, either semi-analytical or empirical, has been routinely made in the visible regime. Based on radiative transfer theory, semi-analytical algorithms relate the ratio between backscattering and absorption of constituents in the water to R_{rs} and simultaneously derive a suite of inherent optical properties (IOPs), including chlorophyll, absorption of colored detrital material (e.g., $a_{dg}(443)$), and the backscattering coefficient of particles (b_{bp}) (e.g., Garver and Siegel 1997; Lee et al. 2002; Maritorena et al. 2002). Empirical algorithms have been used to statistically correlate a_g at specific visible wavelengths (e.g., $a_g(412)$), obtained either from *in situ* IOP profile observations or spectrophotometric measurements, to various R_{rs} ratios (e.g., Del Castillo and Miller 2008; Mannino et al. 2008). Additionally, a_{g} has been estimated by relating R_{rs} to an intermediate parameter (i.e., the diffuse attenuation coefficient, K_{d}), and subsequently using this to derive a_{g} based on an empirical relation between K_{d} and a_{g} (Fichot and Miller 2010; Johannessen et al. 2003b). The satellite derived estimates of $a_{\mathrm{dg}}(443)$ or $a_{\mathrm{g}}(412)$, are in turn used to model UV absorption of CDOM by assuming a single spectral slope (S) coefficient in an exponentially decreasing manner over increasing wavelengths modeled as

$$a_g(\lambda) = a_g(\lambda_o) \times e^{-S(\lambda-\lambda_o)}, \tag{1}$$

where $a_{\mathrm{g}}(\lambda)$ is the desired absorption coefficient (m^{-1}) of CDOM at wavelength λ, λ_o is the reference wavelength (nm), S (nm^{-1}) is the spectral slope coefficient for the CDOM (CDM) spectrum that describes the shape of the exponential curve (e.g., Bricaud et al. 1981; Twardowski et al. 2004).

Most efforts have modeled a_{g} at UV wavelengths by extrapolation from visible a_{g} estimates either using a predefined S value (Stedmon et al. 2000), or based on the functional relationship between $a_{\mathrm{dg}}(443)$ and S (Swan et al. 2013). Unfortunately, field studies have shown that S varies significantly with source material and biogeochemical processes that alter CDOM. Also, there have been few studies attempting to retrieve S from remote sensing (Carder et al. 1989; Fichot et al. 2013; Fichot et al. 2014; Vähätalo and Wetzel 2004). Recently, studies have proposed that S in the UV (e.g., $S_{275\text{-}295}$), can be used as a tracer for photochemical modification of terrestrial dissolved organic carbon in river-dominated coastal margins (Fichot and Benner 2012; Fichot et al. 2013). Other studies have also shown that the ratio between S values determined over different wavelength intervals (S_{R}), may reveal additional DOM chemical characteristics. Helms et al. (2008) proposed S_{R}, calculated as the ratio of $S_{275\text{-}295}$ to $S_{350\text{-}400}$, as a proxy for DOM molecular weight (MW), with changes indicating photochemical alteration of MW. Although S_R has been used to study the dynamics of DOM in samples taken from natural waters (Helms et al. 2013; Stubbins et al. 2012; Yamashita et al. 2013), synoptic assessment of S_R has not yet been made from remote sensing.

Since CDOM photoactive wavelengths are in the UV and blue spectral range, an accurate derivation of a_g at all UV wavelengths from remotely sensed data will prove to be indispensible for large scale spatio-temporal studies of DOM dynamics in the ocean. Based on work published by Fichot et al. (2008c) and Cao et al. (2014), we propose a new algorithm for retrieving the CDOM absorption spectrum over UV and short visible wavelengths (λ = 275-450 nm) from ocean color. This model, referred to hereafter as Sea*CDOM*, is primarily designed for determining UV absorption by CDOM in the ocean using the data from the *Sea*-viewing *Wide* Field-of-view Sensor (SeaWiFS) mission. As far as we know, this algorithm is the first model that retrieves spectrally resolved CDOM absorption in the UV from visible ocean color, free of prior assumptions of the exponential shape of CDOM spectrum. Unlike previous algorithms with a defined S, the derivation of CDOM absorption spectra from Sea*CDOM* allows direct calculation of S over any wavelength range from ocean color. The remainder of this manuscript is structured as follows. In section 2, we describe the training dataset, mathematical principles behind the algorithm, and briefly describe three other published ocean color algorithms for model performance comparison. In section 3, we present the results of Sea*CDOM* and performance for each of the four algorithms using our training dataset. Section 4 contains results for the validation process and a discussion of advantages and limitations associated with the algorithm, as well as a sample application of the algorithm to SeaWiFS imagery with derivation of a_g, S, and S_R.

2. Data and Approach

2.1. Data acquisition and preparation for the training data set

The training data set, including R_{rs} and spectrally resolved $a_g(\lambda)$ data, was compiled from two subsets; one from coastal Georgia and one with more extensive geographic coverage acquired from the SeaWiFS Bio-optical Archive and Storage System (SeaBASS, available from http://seabass.gsfc.nasa.gov/). For the coastal Georgia data set, multiple sampling expeditions were conducted along the southeastern US coast, spanning three estuarine systems (Altamaha, Doboy, and Sapelo sounds in the state of Georgia) during 2007 to 2011. A complete description of the hydrological characteristics for the sampling area is given in Cao et al. (2014). These sites are considered highly dynamic, optically deep systems. A total of 97 *in situ* measurements of $R_{rs}(\lambda, 0^+)$ were made at wavelengths coincident with SeaWiFS bands, centered at λ = 412, 443, 490, 510, 555, and 670 nm using a Satlantic® OCR507. Details on radiometric data collection can also be found in Cao et al. (2014). Discrete water samples were taken concurrently with radiometric measurements at each station. Surface water for CDOM analysis was collected using a clean plastic container and immediately filtered into precombusted glass bottles under low vacuum via a 0.2 μm Whatman Polycap AS 75 nylon cartridge filter, with samples subsequently stored at 4°C in the dark until further analysis. Absorbance spectra of CDOM were measured on a Perkin-Elmer Lambda-40 spectrophotometer using a 1-cm quartz cuvette over the range of 250-800 nm. Baseline corrections were made by subtracting an offset value from the absorbance spectra, according to Green and Blough (1994). The offset-corrected absorbance of CDOM was then converted into an absorption coefficient following Eq. (2)

$$a_g(\lambda) = 2.303 \times A(\lambda)/L, \tag{2}$$

where $a_g(\lambda)$ (m^{-1}) is the Napierian absorption coefficient of CDOM at wavelength λ, $A(\lambda)$ (unitless) is the measured CDOM absorbance at λ, and L (m) is the path length of the spectrophotometric cell.

In addition to the coastal Georgia data set, *in situ* radiometric data covering a wide spatial and temporal scale were queried from SeaBASS. These included R_{rs} or other apparent optical properties (AOPs), such as downward irradiance ($E_d(\lambda, 0^-)$), upwelling radiance ($L_u(\lambda, 0^-)$) just beneath the sea surface, along with fully resolved $a_g(\lambda)$ spectra with λ = 275-750 nm at 1 nm intervals. Only matched AOP and IOP observations identified as "coincident measurements in time and space" were included, according to Werdell and Bailey (2005). In light of the great variability in the data sources from various contributors, quality control was performed to rule out potentially problematic data points. In cases where R_{rs} was reported at non-SeaWiFS wavelengths, R_{rs} at corresponding SeaWiFS bands were estimated using a cubic spline interpolation method (Butler et al. 2003). For observations where radiometric results are described by AOPs other than remote sensing reflectance, R_{rs} was obtained according to the following equation

$$R_{rs}(\lambda, 0^+) = L_w(\lambda)/E_d(\lambda, 0^+), \tag{3}$$

where water-leaving radiance $L_w(\lambda)$ and downwelling irradiance right above the sea surface $E_d(\lambda, 0^+)$ were calculated using the approximations $L_w(\lambda) = 0.54 \times L_u(\lambda, 0^-)$ and $E_d(\lambda, 0^+) = 1.04 \times E_d(\lambda, 0^-)$, respectively (Austin 1974).

For acceptable IOP data reported in SeaBASS, because the purpose of our algorithm was to retrieve a_g from remote sensing, we limited the a_g measurement depth to the surface layer (less than 5 m). In samples from the African Monsoon Multidisciplinary Analysis (AMMA) cruises, where the surface data was not available, the acceptable measurement depth was extended to the upper 15 m, assuming that a_g in the mixed layer is homogeneous (Montegut et al. 2004). CDOM absorption spectra were visually inspected and those that plotted as jagged or erratic curves were rejected from further compilation, according to the measurement protocol from International Ocean Colour Coordinating Group (IOCCG, available from http://www.ioccg.org/training/pogo_ioccg/beagle/protocols/cdom_protocols.doc). Prior to final compilation, baseline correction to CDOM spectra was either made by initial data contributors prior to submission (as obtained from comments in each data file or by visually examining the absorption spectra), or performed in the same manner as the coastal Georgia IOP data. The quality data set from SeaBASS, once queried and screened, was considered accurate, yielding 377 observations. This SeaBASS data set was merged with the coastal Georgia data and a total of 474 observations were prepared as the training data set for developing the algorithm (Figure 3.1 and Table 3.2). The training data set is largely obtained from SeaBASS and consequently includes an aggregation of multiple data sets obtained from various geographic locations, optical instruments, and sampling protocols during different field campaigns. All this introduces a variety of uncertainty sources. It is therefore not practical to quantify the uncertainty level in processing R_{rs} and CDOM spectral data from all these campaigns.

2.2. Algorithm development

The Sea*CDOM* algorithm was developed in three stages using statistical relationships between ocean color (R_{rs} at SeaWiFS bands) and CDOM absorption coefficients. We first applied principal component analysis (PCA) to collapse the multispectral visible R_{rs} data into several representative principal components (PCs). We then classified the ocean color data set, spanned by the first three PCs, into distinct clusters. Finally, a multiple linear regression (MLR) analysis was performed between measured a_g at each wavelength individually to the PCs. The details of this procedure are described in the following section. A complete flow chart for implementing the algorithm is provided in Appendix A.

2.2.1. Stage 1: Principal component analysis of remote-sensing reflectance

To utilize as much AOP multispectral information as possible, we applied PCA to reduce the dimension of the dataset to several principal components that can best recreate the original data (Garver et al. 1994; Johnson and Wichern 2002; Mueller 1976; Toole and Siegel 2001). Since PCA is built on a framework of linear algebra, prior to performing PCA on the AOP dataset, R_{rs} data at each SeaWiFS band (centered at λ = 412, 443, 490, 510, 555, and 670 nm) were log-transformed [*Sathyendranath et al*., 1994] and standardized according to the following equation:

$$A_i(\lambda) = [R_i(\lambda) - \mu(\lambda)]/\sigma(\lambda) \qquad (4)$$

where $R_i(\lambda)$ is the log-transformed R_{rs} at wavelength λ for the *i*th observation, $\mu(\lambda)$ and $\sigma(\lambda)$ stand for the mean and standard deviation of the log-transformed R_{rs} at wavelength λ, respectively, and $A_i(\lambda)$ is the standardized R_{rs} at wavelength λ for the *i*th observation, which was used as the input for PCA in the following step.

The standardized R_{rs} data, consisting of 474 *in situ* observations of R_{rs} at 6 visible SeaWiFS bands, with a dimension of $[474 \times 6]$ (denoted here as data matrix $\boldsymbol{A}$**)**, was subjected to PCA using the open source statistical computing software “R” (http://www.r-project.org/). It should be noted that PCA encapsulates the variability of R_{rs}, by including a range of illumination conditions. PC extraction first involves an eigen-decomposition of the correlation matrix $\boldsymbol{\rho}$ $[6 \times 6]$ of $\boldsymbol{A}$ as shown in Eq. (5):

$$\boldsymbol{\rho} = \boldsymbol{U\Lambda U^{-1}} \qquad (5)$$

where $\boldsymbol{U}$ is a $[6 \times 6]$ matrix containing loadings of linearly independent eigenvectors, with each column corresponding to one eigenvector of $\boldsymbol{\rho}$; $\boldsymbol{\Lambda}$ is a $[6 \times 6]$ diagonal matrix of eigenvalues associated with each eigenvector, by which the degree of variance for each eigenvector was explained. Superscript (–1) denotes the pseudo-inverse of a matrix. Because eigenvectors are orthogonal to each other, the score on each PC was calculated by projecting the original data set (matrix $\boldsymbol{A}$) onto a newly formed coordinate system spanned by eigenvectors $\boldsymbol{U}$. Thus, the matrix of PC scores (hereafter designated as $\boldsymbol{T}$) was derived as the linear combination of R_{rs} and $\boldsymbol{U}$ in the form of

$$\boldsymbol{T} = \boldsymbol{A}\boldsymbol{U} \tag{6}$$

where $\boldsymbol{T}$ is a $[474 \times 6]$ matrix containing scores on each PC for each observation.

2.2.2. Stage 2: Classification into ocean color clusters

Since the first three PCs account for the majority of the total variance in R_{rs} (as shown later in section 3.1.1, >99% of total variance, (North et al. 1982)), it is reasonable to perform cluster analysis (CA) on only the first three PCs (denoted as PC1, PC2, and PC3 in the following text) to classify the R_{rs} features into different ocean color clusters. Therefore, a fuzzy c-means clustering method was applied to the 3D space spanned by PC1, PC2, and PC3. The rational and procedure for this stage is given in Cao et al. (2014) and references therein. A detailed description of the clustering results is presented in section 3.1.2.

2.2.3. Stage 3: Retrieving spectrally resolved $a_{\mathrm{g}}(\lambda)$ from remote sensing reflectance using the ordinary least squares (OLS) method

Considering that total UV light attenuation can be successfully described as K_{d} from ocean color, and that CDOM is the major absorber of UV in natural waters (Tedetti and Sempere 2006), we chose to correlate a_{g} in the UV domain directly to visible R_{rs}. Theoretically, to reproduce the total variance that is contained in the original R_{rs} data, all six PCs should be used. However, since the first three PCs describe more than 99% of the variance (Figure 3.2 (b)), and adding the forth through the sixth PCs to the model did not significantly improve the overall performance (North et al. 1982), we retained the first three principal components as predictor variables for subsequent algorithm development. Also, because the purpose of our effort was to retrieve a_g in the UV and short visible wavelengths, we focused on an a_g spectral range of λ = 275-450 nm.

In each ocean color cluster, a_g at a given wavelength λ, $a_g(\lambda)$, can be formulated to the three PCs in a MLR form (judged by Akaike information criterion, or AIC) as:

$$\ln(a_g(\lambda)_i) = \beta_0(\lambda) + \beta_1(\lambda)\times PC1_i + \beta_2(\lambda)\times PC2_i + \beta_3(\lambda)\times PC3_i \qquad (7)$$

where i is the index number of the ith observation; $\beta_0(\lambda)$, $\beta_1(\lambda)$, $\beta_2(\lambda)$, and $\beta_3(\lambda)$ are regression coefficients for the MLR at wavelength λ (more details can be found in the auxiliary material section 2). For the fully resolved CDOM spectra, the MLR can be further developed in a matrix form as:

$$\boldsymbol{y}(\lambda) = \boldsymbol{X\beta}(\lambda) + \boldsymbol{\varepsilon}(\lambda) \qquad (8)$$

where $\boldsymbol{y}$ is a column vector with a dimension of $[n \times 1]$ and $\boldsymbol{y}(\lambda) = [\ln(a_g(\lambda)_1) \quad \ln(a_g(\lambda)_2) \cdots \ln(a_g(\lambda)_i) \cdots \ln(a_g(\lambda)_n)]^T$ with superscript T denoting the matrix transpose, and i and n are the index number of the ith observation and the total number of observations in the cluster, respectively. The matrix $\boldsymbol{X}$ $[n \times 4]$

denotes the PC scores extracted from R_{rs} and $\boldsymbol{X} = \begin{bmatrix} 1 & PC1_1 & PC2_1 & PC3_1 \\ 1 & PC1_2 & PC2_2 & PC3_2 \\ \vdots & \vdots & \vdots & \vdots \\ 1 & PC1_i & PC2_i & PC3_i \\ \vdots & \vdots & \vdots & \vdots \\ 1 & PC1_n & PC2_n & PC3_n \end{bmatrix}$.

The column vector of parameters $\boldsymbol{\beta}(\lambda)\,[4 \times 1]$ is the solution to Eq. (8) and $\boldsymbol{\beta}(\lambda) = [\beta_0(\lambda)\ \beta_1(\lambda)\ \beta_2(\lambda)\ \beta_3(\lambda)]^T$. Column vector $\boldsymbol{\varepsilon}(\lambda)\,[n \times 1]$ represents the residuals for each observation that cannot be explained by the linear combination of three PCs and $\boldsymbol{\varepsilon}(\lambda) = [\varepsilon_1(\lambda)\ \varepsilon_2(\lambda)\ \cdots\ \varepsilon_i(\lambda)\ \cdots\ \varepsilon_n(\lambda)]^T$. Assuming a Gaussian distribution of the error term (ε), the ordinary least squares solution (Johnson and Wichern 2002) to Eq. (8) is given by

$$\boldsymbol{\beta}(\lambda) = (\boldsymbol{X}^T\boldsymbol{X})^{-1}\boldsymbol{X}^T\boldsymbol{y}(\lambda). \tag{9}$$

Thus by fitting the MLR models between a_g measured at each wavelength and three PCs individually, the final product of the Sea*CDOM* algorithm returns a matrix composed of various column vectors $\boldsymbol{\beta}(\lambda)$, with each column corresponding to one wavelength (λ = 275-450 nm at 1 nm increments), for each ocean color cluster.

2.3. Algorithm Performance Assessment

Three previously published ocean color algorithms were used to compare the relative accuracy of the Sea*CDOM* algorithm for retrieving a_g from remote sensing. These include: (i) the empirical ocean color band-ratio algorithm from Mannino et al. (2008), (ii) the Sea*UV* algorithm developed with a MLR approach similar to Sea*CDOM*, but estimating K_d as an intermediate step (Fichot and Miller 2010), and (iii) the algorithm proposed by Swan et al. (2013). In this section, we briefly describe these three algorithms (section 2.3.1-2.3.3) and the statistics used for algorithm performance assessment (section 2.3.4).

2.3.1. Empirical band-ratio based algorithm

Widely used R_{rs} spectral band-ratio based algorithms for estimating a_g have been developed in the framework of linear, or exponential relationships between a_g and R_{rs} (e.g., Del Castillo and Miller 2008; Mannino et al. 2008). First, this approach correlates a_g at a visible wavelength (typically at λ = 412) to various R_{rs} band ratios, and then extrapolates to the UV domain either by assuming an exponential CDOM absorption spectra (Eq. (1)) with a predefined S value (typically 0.014 nm^{-1}) (Stedmon et al. 2000 and references therein) or, alternatively, through a hyperbolic equation between $a_g(412)$ and a_g at other wavelengths ($a_g(\lambda)$), as suggested by Twardowski et al. (2004). Considering that band-ratio algorithms are usually developed for specific regions, we have not tested a specific published model, but rather have tested the *approach* by optimizing the formulation between $a_g(412)$ and R_{rs} band ratios to our training data set. A linear least squares fitting technique was employed with various R_{rs} band ratios ($R_{rs}(412)/R_{rs}(555)$, $R_{rs}(412)/R_{rs}(510)$, $R_{rs}(443)/R_{rs}(510)$, $R_{rs}(490)/R_{rs}(555)$, etc.) as predictor variables and with measured, *in situ* $a_g(412)$ as the response variable. The best linear regression (with $r > 0.90$) derived for our training data set resulted in the following relationship

$$\ln\left[a_g(412)\right] = -1.145 \times \ln[R_{rs}(490)/R_{rs}(555)] - 2.167 \qquad (10)$$

a_g values in the UV can be computed with the hyperbolic equation from Twardowski et al. (2004) as follows

$$a_g(\lambda) = a_g(412) \times (\lambda/412)^{-6.92} \qquad (11)$$

This R_{rs} band-ratio algorithm with a hyperbolic $a_g(\lambda)$ model is referred to as "R_{555}^{490}-HM" in the following text.

2.3.2. Sea*UV* based empirical algorithm

The Sea*UV* algorithm (Fichot and Miller 2010; Fichot et al. 2008c) first retrieves K_d in the UV (e.g., K_d at $\lambda = 320$ nm) from visible R_{rs} bands using PCA and MLR and then estimates $a_g(320)$ using the relation

$$a_g(320) = 0.68 \times K_d(320). \qquad (12)$$

Once $a_g(320)$ is obtained, a_g at other wavelengths is calculated assuming an exponential function with $S = 0.0194$ nm^{-1}. Cao et al. (2014) extended the original Sea*UV* model for improved performance in darker, optically complex coastal waters with a composite set of algorithms that accurately retrieve K_d in the UV for almost all types of marine waters. We applied these composite algorithms, along with Eq. (12) to predict a_g in the UV. This algorithm is hereafter referred to as "C-Sea*UV*".

2.3.3. Spectral slope based semi-analytical algorithm

The model published by Swan et al. (2013) was also applied to our training data set for inter-comparison. This approach retrieves a_g in the UV and near-UV visible using an exponential relationship between the spectral slope coefficient ($S_{320\text{-}400}$) and $a_\mathrm{g}(443)$ derived from an extensive field IOP data set obtained mostly in Case 1 waters. The original exponential function was then optimized using $a_\mathrm{dg}(443)$ as input that can be inverted from the semi-analytical Garver-Siegel-Maritorena (GSM 01) algorithm, making it possible to estimate a_g in the UV (with λ = 325-412 nm) from ocean color. We refer to this slope extrapolation method of Swan et al. (2013) as "GSM-SE" in the following text.

2.3.4. Accuracy Assessment

To evaluate performance, CDOM absorption spectra (λ = 275-450 nm, 1 nm resolution) were derived from each of the four algorithms using identical measured *in situ* R_rs as input. These estimates were compared to the matching *in situ* $a_\mathrm{g}(\lambda)$ spectra in the training data set. The mean absolute percent difference (mean APD) and root-mean-square-error (RMSE) were used to judge performance. Mean APD and RMSE are defined as follows:

$$mean\ APD(\lambda) = \left\{ \sum \left| \frac{\left[a_g(\lambda)_i^{estimated} - a_g(\lambda)_i^{measured}\right]}{a_g(\lambda)_i^{measured}} \right| \right\} \times 100/N \qquad (13)$$

$$RMSE(\lambda) = \left\{\frac{\Sigma\left[\log_{10}\left(a_g(\lambda)\right)_i^{estimated} - \log_{10}\left(a_g(\lambda)\right)_i^{measured}\right]^2}{N-2}\right\}^{\frac{1}{2}} \qquad (14)$$

where $a_g(\lambda)_i^{estimated}$ and $a_g(\lambda)_i^{measured}$ are a_g values from each algorithm and measured *in situ* at wavelength λ for the *i*th observation, respectively. N is the number of observations.

2.4. Algorithm Validation and Spectral Slope Determination

To examine a broad range of optical diversity, we applied our algorithm to 86 matched measurements of R_{rs} and a_g from three independent data sets: (1) seasonal data from the northern Gulf of Mexico, (2) waters around the Mackenzie River outflow in the Arctic Ocean, (3) South Pacific subtropical gyre samples that include the ocean's clearest oligotrophic water (Table 3.3). For validation and performance evaluation, the Sea*CDOM* algorithm was implemented on the R_{rs} spectra and spectrally resolved a_g estimates were compared with the *in situ* measured a_g.

To demonstrate the capacity for predicting S in the UV from visible ocean color with the Sea*CDOM* model, S was determined over the spectral range of 275-295 nm ($S_{275\text{-}295}$) for all observed and estimated $a_g(\lambda)$ in the training data set. $a_g(\lambda)$ spectra were fit to Eq. (1) using the "*nlinfit*" routine in the Statistics Toolbox for MATLAB® (2011, MathWorks, Natick, Massachusetts). Subsequent calculations of $S_{350\text{-}400}$ in section 4 below were carried out in the same way over the spectral range of 350-400 nm. One previously developed algorithm to estimate $S_{275\text{-}295}$ from multispectral ocean color by Fichot et al. (2013) was used to compare estimation accuracy for $S_{275\text{-}295}$. Since this algorithm is proposed with the Moderate-Resolution Imaging Spectroradiometer (MODIS) *Aqua* ocean color data, R_{rs} in our training data set was interpolated to corresponding MODIS *Aqua* wavelengths (Butler et al. 2003) to make it compatible with the algorithm application. To further test the MLR *approach* used in Fichot et al. (2013), as we did with the band ratio algorithm to retrieve a_g, we derived multi-linear regression coefficients with their model that best predict $S_{275\text{-}295}$ from ocean color using our training data set, resulting in the following:

$$\ln[S_{275\text{-}295}] = \alpha + \beta \times \ln[R_{rs}(443)] + \gamma \times \ln[R_{rs}(488)] + \delta \times \ln[R_{rs}(531)] + \varepsilon \times \ln[R_{rs}(555)] + \zeta \times \ln[R_{rs}(667)]. \quad (15)$$

where the derived fitting parameters are $\alpha = -3.0230$, $\beta = 0.3101$, $\gamma = 0.0732$, $\delta = -0.4528$, $\varepsilon = 0.2078$, and $\zeta = -0.0309$.

3. Results

3.1. Statistical analysis of the AOP data set

3.1.1. Output of principal component analysis

The eigen-analysis of $\boldsymbol{\rho}$ generated six eigenvectors and their corresponding eigenvalues. Figure 3.2 shows the first two dominant eigenvectors (Figure 3.2 (a)) and a scree plot with the contribution of each PC to the total variance in $\boldsymbol{A}$ (Figure 3.2 (b)). Because of the relatively small contribution of the third through sixth PC values to the total variance, we focus on the physical interpretation for the first two PCs.

A significant portion (~62%) of the total variance is explained by PC1 (Figure 3.2 (a)), which varies from -0.5 to 0.4 across the spectrum, demonstrating the complexity of optically significant constituents across the various water types in our training data set. PC1's spectral shape has a maximum at 670 nm, a feature common to sediment-laden waters, then declines toward shorter wavelengths. This resembles R_{rs} spectra we collected from the mouth of the Altamaha River with heavy particle loadings in our coastal GA data set (shown later in section 3.1.2). This suggests the importance of particulate backscattering in shaping the observed PC1 spectra. On the other hand, the PC1 score is significantly positively correlated with measured $a_g(320)$ ($r = 0.8$, p-value < 0.001), giving highest scores in CDOM-rich, inshore waters, indicating that absorption is also a critical factor explaining the variability of R_{rs} for PC1. Accordingly, the optically significant constituents described by PC1 are consistent with a combination of absorption and backscattering.

Compared to PC1, the second principal component (PC2) explains less variance (~21%). The spectral shape of PC2 decreases over the blue-green wavelengths, similar to the absorption spectrum of colored detrital material (Morel 1988). There is a significantly negative correlation between PC2 scores and measured $a_g(320)$ ($r = 0.5$, p-value < 0.001), further supporting the point that CDOM may be controlling the eigenvector pattern for PC2 as well. It remains challenging, however, to understand the possible contribution of particle backscattering to this PC due to the scarcity of available b_{bp} data.

The relationships described by each of the PCs for R_{rs} and a_g, corroborate the fact that they may not be linearly correlated to one specific optically active component, as noted by Mueller (1976) and Toole and Siegel (2001). The aim, however, of the Sea*CDOM* approach is to capture as much of the R_{rs} variability as possible in this first step of algorithm development and it is clear that the PCA approach succeeds in this regard, with results applicable to our ocean color data set.

3.1.2. Result of cluster analysis

The cluster analysis performed on the first three PCs resulted in nine distinct ocean color clusters (Figures 3.3 (a-b)). The clustering results of our training data set demonstrate different observed R_{rs} spectral characteristics over a comprehensive scale, and to some degree, are consistent with varying contributions of different optically active constituents across various water types.

Most of the R_{rs} spectra in cluster 1 (N = 27, Figure 3.3 (c)) were collected from the Gulf of Mexico along the western Florida shelf (northwest big bend region and southwest shelf). Compared to the other 8 clusters, the general spectral shape for this cluster is characterized by high broad reflectance in visible wavelengths. A similar spectral shape has been attributed to the presence of mineral particles (Lubac and Loisel 2007).

Cluster 2, 3, 4, 5, and 6 (N = 61, 68, 84, 46, and 39, respectively, Figures 3.3 (d-h)) cover most of the optically complex, nearshore waters sampled from areas like the Tampa Bay, coastal Georgia and the Chesapeake Bay. The mean R_{rs} spectra from these five clusters are similar in shape but different in magnitude. The overall trend for the five mean R_{rs} spectra can be described as low reflectance with limited variability at 412 nm, likely due to high CDOM and detrital particle absorption, with a gradual increase to higher wavelengths as scattering (backscattering) of particles and phytoplankton becomes dominant in the green (555 nm) (Gould and Arnone 1997; Lubac and Loisel 2007). Cluster 5 (Figure 3.3 (g)) contains samples with the highest CDOM absorbance (mean $a_g(320) \sim 13\ \mathrm{m}^{-1}$) among the five clusters. Note that although clusters 2, 3, and 4 (Figures 3.3 (d-f)) have similar a_g values (mean $a_g(320) \sim$ 5.4, 5.8, and 6.8 m^{-1}, respectively), R_{rs} spectra were discriminated into three distinct clusters, indicating that the relative contribution of other water constitutes driving observed R_{rs} were not correlated and varied independently among these water types.

Clusters 7 and 8 (N = 31 and 66, respectively, Figures 3.3 (i-j)) include samples that are typically classified as Case 1 waters, containing most samples from CLIVAR and offshore areas (i.e., CCE-LTER data set from the California coast). In contrast to clusters 2-6, these two clusters have relatively high $R_{rs}(412)$ values that decrease as wavelength increases, consistent with R_{rs} spectra reported for typical Case 1 waters (Werdell and Bailey 2005 and references therein).

Cluster 9 (N = 52, Figure 3.3 (k)) shows a fairly uniform mean R_{rs} spectra in the blue/green wavelengths but substantial variability within the cluster. Interestingly, most of the waters in this group were high latitude waters from the Beaufort/Chukchi Sea and the Southern Ocean near the Antarctic Peninsula. While a large solar zenith angle exists in polar regimes, a more significant influence could result from the peculiar IOPs assemblage at high latitudes, including elevated levels of CDOM at coastal margins from river discharge (Bélanger et al. 2008), densely packaged phytoplankton pigments in response to reduced solar radiation (Arrigo et al. 2011; Matsuoka et al. 2011; Matsuoka et al. 2007; Mitchell and Holmhansen 1991), and high particulate backscattering background (Reynolds et al. 2001). This may at least partially explain these waters being classified as a unique cluster (Szeto et al. 2011).

3.2. Performance of Sea*CDOM* algorithm on the training data set

The retrieval performances from different algorithms at short UV and visible wavelengths are given in Figure 3.4. Statistics for GSM-SE and C-Sea*UV* are comparable, with a mean APD of ~38% and a RMSE of ~0.5 for $a_g(350)$ for example. These are slightly better than the R_{555}^{490}-HM algorithm with its mean APD exceeding 50%. Sea*CDOM*, however, provides improved accuracy for a_g estimates with a mean APD of ~25% and a RMSE of ~0.3 for $a_g(350)$. Discussion of factors that may contribute to this result is provided in section 4.1.

By correlating three PCs to measured a_g at every wavelength independently, Sea*CDOM* can reconstruct each CDOM absorption spectrum (λ = 275-450 nm; 1 nm resolution) for our entire training data set. As shown in Figure 3.5, modeled a_g from the Sea*CDOM* algorithm is in excellent agreement with measured a_g. Figure 3.5 further highlights the improved performance of the Sea*CDOM* algorithm over the short UV spectral region. In the UVB (280-320 nm), R_{555}^{490}-HM and C-Sea*UV* yield large errors relative to measured a_g. Figure 3.6 presents the spectrally resolved mean APD and RMSE associated with all four algorithms tested. A significant improvement in retrieving $a_g(\lambda)$ (λ = 275-450 nm) is achieved with the Sea*CDOM* algorithm over our modeled wavelength range (e.g., for $a_g(350)$, mean APD is ~25% for Sea*CDOM* compared to ~38% for GSM-SE). Also note that Sea*CDOM* demonstrates a consistent retrieval performance over the entire spectral range (Figure 3.6), particularly in the UV domain. Errors produced by other algorithms tested generally increase towards short UV wavelengths (e.g., at $a_g(275)$, Sea*CDOM* achieves a mean APD of ~24%, compared to ~56% and ~45%, respectively for R_{555}^{490}-HM and C-Sea*UV*). Note that the GSM-SE model was optimized over the 325-412 nm range and thus we did not test its performance for $\lambda < 325$ nm. Sea*CDOM* actually performs slightly better in the UV relative to the short visible wavelengths beyond 400 nm (e.g., mean APD ~24% at $a_g(275)$ and ~32% at $a_g(440)$; Figure 3.6). This trend may result from the stronger light absorption of CDOM in lower UV wavelengths, thus allowing better measurement accuracy and less variability in our training data set.

3.3. Performance of the Sea*CDOM* algorithm on validation data sets

Validation results confirm robust performance of the Sea*CDOM* algorithm, with errors comparable to those for the training data set. For example, $a_g(350)$ in the validation test has a mean APD and RMSE of ~28% and ~0.3 respectively, compared with a mean APD of ~25% and RMSE of ~0.3 for the training data set (Figure 3.7). These results indicate that Sea*CDOM* should provide generally good results when estimating a_g at UV wavelengths in marine waters not directly included in our training data set.

3.4. Deriving CDOM spectral slope from ocean color

The Sea*CDOM* algorithm also allows estimates of S using the fully-resolved a_g spectra derived from ocean color. It is encouraging to observe the excellent agreement for $S_{275\text{-}295}$

calculated using measured and estimated a_g spectra (with $r = 0.94$, slope = 0.88, and intercept = 0.003; Figure 3.8 (a)), and the retrieval accuracy was significantly improved compared to the algorithm/*approach* proposed by Fichot et al. (2013) (with $r = 0.85$ and slope = 0.58 from the algorithm in Fichot et al. (2013), and $r = 0.87$, slope = 0.65 using the *approach* developed by Fichot et al. (2013) but tuned for our training data set, respectively, Figure 3.8 (b)) (t-tests, $p < 0.05$, $N = 474$). This further highlights the potential of our algorithm to remotely calculate S over any desired wavelength range, which may provide new applications in tracing CDOM dynamics and provide insights into CDOM-related biogeochemical cycles (Helms et al. 2013; Helms et al. 2008).

4. Discussion

4.1. Merits and Limitations of Sea*CDOM* algorithm

Throughout the course of algorithm development, and with the validation process, the Sea*CDOM* algorithm displayed promising advantages over other models tested. There are, of course, limitations associated with its merits, both of which must be considered when applying it to ocean color data. First, the Sea*CDOM* algorithm is trained with a wide variety of water types using statistical approaches (PCA, CA, and MLR) that likely account for improved performance in a_g retrieval when compared to existing models tested. Rather than relying on R_{rs} at two wavebands like conventional band-ratio ocean color algorithms (e.g., R_{555}^{490}-HM), PCA retains R_{rs} features from all six visible SeaWiFS wavebands. Using this multispectral information, together with a further classification of reflectance spectra according to its spectral shape and magnitude, enables a more complete capture of R_{rs} variability in our training data set. In the C-Sea*UV* algorithm, $a_g(320)$ is retrieved using its relation to K_d. Uncertainties associated with K_d estimates are propagated directly into the estimation of $a_g(320)$ and into a_g at other wavelengths through extrapolation. In the Sea*CDOM* algorithm, however, direct parameterization of $a_g(\lambda)$ with R_{rs} by MLR eliminates error introduced by intermediate steps, allowing a more accurate and straightforward estimation of a_g at all wavelengths. Based on this alone, it is understandable that Sea*CDOM* gave improved retrieval accuracy for estimates of $a_g(\lambda)$.

It should be pointed out, however, that algorithms of this type have limitations. The OLS coefficients derived for MLR are purely empirical, and as such, do not necessarily represent a unique solution to the relation between a_g and R_{rs}. This is because the variability of R_{rs} is driven by various IOPs and not simply a_g. Our algorithm performed very well in Case 1 waters, as clearly shown in the training and validation steps. Good retrieval accuracy was also made in Case 2 waters where the model was initially trained. Applying the Sea*CDOM* algorithm in marine waters with optical characteristics included in our training data set should yield accurate $a_g(\lambda)$ estimates. However, readers should be aware that for instance, in coastal zones, waters with identical remote sensing reflectance profile could have different a_g absorbance (Defoin-Platel and Chami 2007). Consequently, as is the case for all empirical models, application of Sea*CDOM* in water types not captured in the training data set should proceed with some caution.

Additional validation with data from the Gulf of Maine (Figure 3.7) demonstrates these potential limitations. Although $a_g(300)$ in this test fell within the range for which the algorithm was developed ($a_g(300)$ from 1.5 to 31.4 m^{-1}), Sea*CDOM* performed poorly (mean APD ~ 140%). The R_{rs} spectra collected for this test were from far up the rivers and tributaries of the Gulf of Maine watershed in as little as 1.5 m of water and characterized by high values in the red and near-infrared portion of the spectrum, reflectance usually associated with sediment-rich waters (S. Hooker, personal communication, 2013). Failure to predict a_g in this region is likely attributed to (1) the R_{rs} spectral shape not being captured in our initial training data with R_{rs}

magnitudes that were systematically lower than those for the same classifications in the training data set (see supporting information Figure S 3.1 (a) in Appendix D) and a resulting misclassification of these R_{rs} spectrum into clusters 4 and 5, thereby resulting in poor estimates; and (2) strong contributions from other optically active constitutes such as suspended particles, phytoplankton pigments that do not conform to the linear relationships between AOPs and a_g in the MLR derived from our training data set. While Sea*CDOM* attempts to capture as much variability as possible from the different optical constitutes as they relate to AOPs by classification, it is understandable that confidence will decrease in cases with a strong difference in optical composition from those used in any empirical algorithm. In such cases, other optical models may fare better or regional algorithms with specific parameters must be derived to correctly estimate a_g.

Since the variability of ocean color largely reflects changes of IOPs that are subject to physical and biogeochemical processes in the ocean, predictions of a_g may not be satisfactory during extreme mixing events such as upwelling or strong vertical diffusion. For instance, the mean APD for Sea*CDOM* is ~26% at 300 nm when applied to the BIOSOPE data set alone (N = 24). This initially appears disappointing for Case 1 water (e.g., mean APD of cluster 8 in our training data set is ~15%) but on closer examination, the increased errors are seen to arise mainly from only four data points with elevated a_g collected within the Peru-Chile upwelling area. More specifically, although the R_{rs} of these four samples lined up with R_{rs} in our training data set representative of open ocean waters (supporting information Figure S3.1 (b) in Appendix D), and were successfully classified into the proper theoretical clusters (clusters 8 and 9), a_g estimates from the Sea*CDOM* algorithm were not predicted well (mean APD = 43% for these four samples). This may be, in part, ascribed to the distinct intrinsic particulate assemblages and particles levels associated with this upwelling zone relative to those in the central part of the South Pacific Gyre (Stramski et al. 2008). Absorption by particles in these four sample points close to the Peruvian coast was considerably higher than offshore samples (see supporting information Figure S 3.1 (c) in Appendix D and Bricaud et al. (2010, Figure 9)). This, together with the effect of particle backscattering, could potentially result in a similar R_{rs} spectrum that did not have the same R_{rs} to a_{g} relationship as found in our initial model parameterization, thus explaining the large uncertainties in a_{g} estimates and under-performance of our algorithm on these four outlier locations. If these four points are excluded from the validation, the mean APD is reduced to ~19% and becomes comparable to that of Case 1 water in the training data set. Elevated a_{g} values for these four samples were observed by Bricaud et al. (2010), along with reduced S values within a prominent salinity gradient, suggesting a complexity in these upwelling areas that may not be completely captured by our algorithm. Such situations call for the Sea*CDOM* algorithm to be applied in conjunction with hydrographic information of different water masses encountered in the target area.

Another factor that could affect the performance of the Sea*CDOM* algorithm when applied to satellite data involves known atmospheric correction issues. Current methods can overcorrect aerosol effects in the blue portion of the R_{rs} spectrum, in particular for coastal zones, resulting in large errors in satellite observations (e.g., $R_{\mathrm{rs}}(412)$) (Siegel et al. 2000). These uncertainties in $R_{\mathrm{rs}}(412)$ can subsequently translate onto uncertain a_{g} estimates (Fichot et al. 2014). Sea*CDOM* was developed using *in situ* $R_{\mathrm{rs}}(412)$ as part of its spectral algorithm, and consequently uses satellite estimates of $R_{\mathrm{rs}}(412)$ in its retrieval of a_{g} from remotely sensed ocean color. Therefore, retrieval of a_{g}, particularly in coastal waters, will potentially include added uncertainties stemming from atmospheric correction issues and should be carefully considered when assessing satellite-based results.

A second issue for remote predictions of a_{g} is that with the R_{555}^{490}-HM, C-SeaUV, and GSM-SE algorithms, implicit assumptions are made in modeling spectrally resolved a_{g}. These algorithms generally assume that a_{g} is distributed exponentially over UV wavelengths, whereas in fact, this is not always the case (Nelson and Siegel 2013) and CDOM absorption spectral shapes vary with geo-locations. In coastal waters that experience terrestrial runoff, CDOM spectra can be best described with an exponential function. However, a strong deviation from the exponential spectral assumption can occur in open ocean waters such as the North Atlantic subtropical gyre, especially in the UV wavelengths. Nelson and Siegel (2002b) noted that at wavelengths < 320 nm, a_{g} has features that can no longer be modeled exponentially, with potentially large errors resulting from this faulty assumption. Accordingly, the GSE-SE model prudently does not attempt to predict values for a_{g} at wavelengths < 325 nm using an exponential description of *S*. Unlike existing models, the Sea*CDOM* algorithm is independent of any underlying assumptions about spectral shape, resulting in improved prediction of a_{g} over a broad geographic range and through the UVB. To our knowledge, the Sea*CDOM* algorithm is the only approach to date that models the CDOM UV absorption spectra from visible remote sensed ocean color data free of assumptions about its spectral shape.

Third, while current semi-analytical algorithms predict a_{dg} remotely, it remains challenging to further separate a_{dg} into a_{g} and a_{NAP}, since a_{g} and a_{dg} are similar in spectral shape (Siegel et al. 2002). Nelson et al. (1998) noted that in Case 1 waters, where CDOM and NAP co-vary with chlorophyll, the contribution of NAP to the total absorption is ~9% at 443 nm and therefore negligible. This approximation is quite reasonable for chlorophyll estimates since

CDOM and NAP are both considered by-products of phytoplankton and there is no need to further discriminate between the two. With respect to photochemistry, however, CDOM likely dominates UV driven photoreactions in the ocean and photochemical efficiency is almost always defined as a function of the rate of CDOM photon absorbance. Therefore, a_g, rather than a_{dg}, is ultimately needed for accurate modeling of photochemical processes (Bélanger et al. 2008; Fichot and Miller 2010). Using the direct link between a_g in the UV and R_{rs}, the Sea*CDOM* algorithm makes a_g retrievable from ocean color and facilitates further evaluation of photochemical reactions in the surface ocean.

Finally, direct prediction of S and S_R can be achieved from ocean color using the Sea*CDOM* algorithm. As stated previously, most if not all published remote sensing algorithms generally extrapolate using an unvaried S to calculate a_g in the UV but the validity of this approach has long been challenged along two lines of reasoning: (1) If S reflects the composition of CDOM, then it should be variable with different water types and can be altered by physical mixing and biogeochemical processes, and (2) if S describes the rate at which absorption decreases over wavelengths, then it will largely depend on the spectral range selected and the curve fitting techniques applied (Blough and Del Vecchio 2002b; Twardowski et al. 2004). As expected, measured S values reported in the literature are highly variable. Nevertheless, to facilitate a_g estimation in the UV via an extrapolation method, existing algorithms reconcile this discrepancy by simplifying S into one “average” value which varies slightly among different algorithms (e.g., $S = 0.0194\ \text{nm}^{-1}$ in C-Sea*UV*, while $S = 0.0206\ \text{nm}^{-1}$ in GSM01). While this approach may capture the average CDOM spectra, it imparts error in the estimate and has no capacity to examine the variations in S that are known to exist. Moreover, most of the published S values do not involve the UV domain, either because the authors’ concern was in the visible or due to instrument limitations (Reader and Miller 2011b and references therein). Large errors could arise from extrapolation into the UVB, as supported by the fact that S values obtained from different UV ranges on the same sample can be very different (Twardowski et al. 2004 and references therein). As discussed earlier in section 3.4, by reconstructing CDOM absorption spectra at individual wavelengths directly from ocean color, Sea*CDOM* allows calculation of S and S_R remotely.

4.2. Application to Satellite Imagery

To demonstrate the capability for Sea*CDOM* to predict a_g in the UV, and to allow the direct calculation of S ($S_{275\text{-}295}$, $S_{350\text{-}400}$) and S_R ($S_{275\text{-}295} : S_{350\text{-}400}$) on a synoptic scale, we applied the algorithm to SeaWiFS imagery centered over the Equatorial and North Atlantic Ocean (90°W-10°E, 15°S-45°N). The scene was chosen to provide a wide range of oceanographic and optical scenarios for examination of Sea*CDOM*'s performance. Ten-year monthly climatology data (Level-3, binned 9×9 km^2 spatial resolution) from 2001 to 2010 for R_{rs} in February and August was acquired from the NASA ocean color website (http://oceancolor.gsfc.nasa.gov). This application, based on climatological data, is obviously not meant to assess the absolute accuracy for predicting specific *in situ* observations for CDOM and/or S, but rather to show the ability of the Sea*CDOM* algorithm to address CDOM-related distributions and processes in the ocean from satellite imagery.

Overall, the climatology of $a_g(320)$ captures its main features in the ocean over the seasons. Figures 3.9 (a) and (b) show the expected increased $a_g(320)$ values in coastal waters subjected to terrestrial impact. For example, $a_g(320)$ values at the Amazon River mouth are elevated due to input of terrestrially derived CDOM with strong UV absorption, relative to its adjacent western tropical Atlantic Ocean water. Higher $a_g(320)$ values can also be found in areas that experience upwelling, possibly representing CDOM-rich deeper waters brought to the surface (e.g., seasonal upwelling peaking during winter and early spring off Cape Blanc). On the other hand, reduced $a_g(320)$ values are observed in regions prone to downwelling such as that found in the North Atlantic subtropical gyre. Superimposed on this spatial mapping of $a_g(320)$, temporal variations of CDOM can also be seen with the ocean color climatology. For instance, the Amazon River plume is clearly seen flowing northward during wintertime (February, Figure 3.9 (a)), as compared to an eastward flow toward Africa, retroflexed by the North Equatorial Counter Current in the summer (August, Figure 3.9 (b)) (Coles et al. 2013 and references therein). Reduced $a_g(320)$, possibly indicating CDOM photobleaching from enhanced solar radiation during boreal summer (Swan et al. 2009b), is also observed in the North Atlantic subtropical gyre and in Mediterranean waters (Figure 3.9 (b)), as compared to relatively higher values in the winter (Figure 3.9 (a)) at the same locations. Further, higher winter CDOM levels in the Sargasso Sea are consistent with strong convective mixing and weaker surface irradiance (Figure 3.9 (a)), similar to field observation made by Nelson et al. (1998). These same oceanographically consistent a_g observations are likely seen with all of the CDOM models tested, but based on error analysis from validations and our training data set, any quantitative comparison of the a_g variability using the Sea*CDOM* algorithms should be more highly constrained than previous estimates.

The climatology of $S_{275\text{-}295}$ derived by Sea*CDOM* from ocean color shows patterns that are largely correlated to $a_g(320)$ (Figures 3.9 (c) and (d)), an expected result given that higher and lower a_g are usually accompanied by smaller and larger S values respectively (Nelson and Siegel 2002b). For example, the elevated $a_g(320)$ is observed in the Amazon River plume due to large amounts of terrestrially derived CDOM input are mapped as reduced $S_{275\text{-}295}$ values.

Conversely, low $a_g(320)$ in the North Atlantic subtropical gyre are coincident with elevated $S_{275\text{-}295}$. Seasonal variability of $S_{275\text{-}295}$ also mirrors a_g, capturing the variability of the Amazon River plume (Figures 3.9 (c) and (d)) and $S_{275\text{-}295}$ variations consistent with CDOM photobleaching offshore. $S_{275\text{-}295}$ is reported to be more sensitive to photo-alteration processes than a_g alone, and can be used as a tracer for photochemical history of CDOM in both coastal waters (Fichot and Benner 2012) and the open ocean (Yamashita et al. 2013). Increased $S_{275\text{-}295}$ values associated with CDOM photobleaching are thought to reflect shifts from high to low MW within the CDOM pool (Helms et al. 2013; Helms et al. 2008). $S_{275\text{-}295}$ may also contain information on source material and the molecular composition of CDOM, however, investigations of photochemical processes on $S_{275\text{-}295}$ from ocean color are rare (Fichot et al. 2013). With its unique ability to estimate $S_{275\text{-}295}$ directly from R_{rs}, the Sea*CDOM* algorithms provide a new and promising remote sensing tool for tracing oceanic changes in S, potentially providing MW information for the surface DOC pool during the course of exposure to sunlight.

Unlike the climatology of $a_g(320)$ and $S_{275\text{-}295}$, the map of $S_{350\text{-}400}$ does not reflect recognizable oceanic patterns. This is not surprising since Fichot and Benner (2012) and Helms et al. (2008) both found that $S_{350\text{-}400}$ is less sensitive than $S_{275\text{-}295}$ to photochemically influenced changes and lacks a correlation to either salinity or photochemical history, findings consistent with Sea*CDOM* results. Figure 3.9 (e) does not show as clear a signature for $S_{350\text{-}400}$ in the Amazon River outflow where increased a_g and reduced $S_{275\text{-}295}$ have been observed. Yamashita et al. (2013) found a similar result with no noticeable difference of $S_{350\text{-}400}$ between subtropical and subarctic Pacific waters, thus inferring that $S_{350\text{-}400}$ in the open ocean is likely governed by factors other than photobleaching.

Finally, we generated a map of slope ratio, S_R, (Figures 3.9 (g-h)) and this distribution generally matches those of $a_g(320)$ and $S_{275\text{-}295}$. In the subtropical North Atlantic, elevated S_R is observed coincidentally with increased $S_{275\text{-}295}$, a result consistent with CDOM photobleaching. At present, the chemical interpretation of S_R is debated, with some studies showing changes of S_R for terrestrial and coastal DOM during photo-exposure (Helms et al. 2008) while others claim this index does not change with CDOM photochemical bleaching (Yamashita et al. 2013). Helms et al. (2008) suggested that variability of S_R along an estuarine gradient results from the combined effect of photochemical and microbial alternations, with increased S_R associated with photochemistry and reduced S_R resulted from microbial activity. An argument for the photochemical impact on S_R can be made by comparing Figures 3.9 (c-d) and (g-h) in the Mediterranean Sea. Both elevated S_R and $S_{275\text{-}295}$ are observed in summertime compared with relatively low values for both in the winter. Using climatologies, however, to examine the balance between photochemical and microbial influences on S_R will not resolve the issue and further field measurements are needed to clarify the possible links between these processes and the optical characteristics of CDOM. Sea*CDOM,* with its unique ability to examine these CDOM UV optical relationships directly over large spatial and temporal scales, should provide new capacity to extrapolate field results to quantitative models.

5. Summary and Conclusions

Developed using an extensive training data set covering various water types with contemporaneous collection of *in situ* R_{rs} at SeaWiFS bands, centered at λ = 412, 443, 490, 510, 555, and 670 nm, with a_g(275-450 nm) in the surface ocean, a new algorithm has been developed to estimate CDOM absorption spectra in the UV from ocean color remote sensing in the global ocean. It provides improved retrieval accuracy compared to existing algorithms, having an overall mean APD of ~25% for $a_g(350)$. The inherent benefits offered by the statistical approaches used in our algorithm development allow a spectrally resolved CDOM absorption spectrum to be reconstructed from remotely sensed visible reflectance, free of any presupposition about the spectral shape for CDOM absorption (i.e., there is no assumed exponential shape or slope coefficient). Furthermore, the ability to recreate a fully resolved CDOM absorption spectrum in this way allows the calculation of spectral slope (S) over any wavelength range and the "slope ratio" (S_R), potential proxies for MW and CDOM source material. Therefore, the methodologies developed in this manuscript provide the oceanographic community an exciting new tool to investigate the dynamics of CDOM in response to changing physical and biogeochemical processes, potentially tracking the origin, transformation, and chemical/molecular evolution of CDOM in the context of global ocean carbon cycles.

As an empirical model, there are certain limitations to the algorithm that may result in sub-par performance in its a_g retrieval for optical cases or study areas outside the training data set. This could result from possible bias or invalidity of the linear regression relationship between CDOM and reflectance. Nevertheless, this approach provides a novel means to accurately retrieve CDOM absorption in the UV from ocean color in a very broad spectrum of oceanic waters. Given its empirical nature, the algorithm can be updated and expanded with additional data sets containing additional bio-optical diversity, filling gaps in areas not currently included. By leveraging the approach in this study, regional tuning of the model for specific areas, especially in optically complex waters heavily impacted by terrestrial runoff, could help overcome existing deficiencies in the algorithm and rectify prediction errors (e.g., our Gulf of Maine validation).

Even though the Sea*CDOM* algorithm is initially developed using SeaWiFS wavelengths, data that does not extend beyond 2011, the methodological details offered by this study can easily be applied to current and forthcoming satellite missions, such as the MODIS, the Medium Resolution Imaging Spectrometer (MERIS), the Ocean and Land Colour Instrument (OLCI), the Pre-Aerosol, Clouds, and ocean Ecosystem (PACE), and the GEOstationary Coastal and Air Pollution Events (GEO-CAPE) missions, etc, being developed to remotely address biogeochemical issues in the ocean.

While the development of our Sea*CDOM* algorithm was originally motivated by a need for accurate UV estimates for calculating marine photochemical processes related to organic carbon cycling, the algorithm should find applications in other photo-related oceanographic fields. For instance, accurate understanding of UV light attenuation due to CDOM in the aquatic ecosystem can be beneficial to evaluation of the effect of UVB-induced photoinhibition and DNA damage on marine biota (Lindell et al. 1995 and references therein). In addition, organic breakdown products from DOM photolysis represent a transfer of carbon into the microbial loop, stimulating heterotrophic bacterial respiration. Consequently, quantifying CDOM absorptivity in the DOM pool will help clarify interactions between photochemical and microbial processes and resolve the complexity of DOM liability in the marine systems (Miller and Moran 1997; Reader and Miller 2014).

Acknowledgments

The coastal Georgia data and Matlab code for developing the algorithm are available from the authors (bmiller@uga.edu) upon request. A complete scheme on the Sea*CDOM* algorithm implementation and required parameters are provided in the supporting material. Financial support from the Office of Naval Research (N00140610219), NASA (NNX07AD85G), and Georgia Sea Grant (R/SD-5) for coastal Georgia fieldwork are gratefully acknowledged. We would like to thank L. Powers, J. Green, I. Sellers, M. Price and J. Johnson for sampling assistance aboard the *R/V Mud Minnow*. S. Lohrenz and C. Fichot provided the Gulf of Mexico validation data from the GulfCarbon cruises (2009-2010), funded by the NSF (OCE-0752254). S. Hooker kindly shared the AOPs data from the Gulf of Maine and MALINA cruises. We are greatly indebted to scientists who contributed bio-optical data to the SeaBASS archive, the BIOSOPE database, and to NASA for providing access to SeaWiFS data. SeaWiFS data were used in accordance with the SeaWiFS data access authorization policy. A. Burd provided helpful suggestions on algorithm development and mathematical descriptions. This work also benefited greatly from discussions with D. Di Iorio and D. Mishra. We also thank Simon Bélanger and another anonymous reviewer for their detailed and thorough reviews of this manuscript.

References

Arrigo, K.R., Matrai, P.A., & van Dijken, G.L. (2011). Primary productivity in the Arctic Ocean: Impacts of complex optical properties and subsurface chlorophyll maxima on large-scale estimates. *Journal of Geophysical Research-Oceans, 116*

Austin, R.W. (1974). The remote sensing of spectral radiance from below the ocean surface. *Optical aspects of oceanography*, 317-344

Bélanger, S., Babin, M., & Larouche, P. (2008). An empirical ocean color algorithm for estimating the contribution of chromophoric dissolved organic matter to total light absorption in optically complex waters. *Journal of Geophysical Research: Oceans (1978–2012), 113*

Blough, N.V., & Del Vecchio, R. (2002). Chromophoric DOM in the coastal environment

Bricaud, A., Babin, M., Claustre, H., Ras, J., & Tieche, F. (2010). Light absorption properties and absorption budget of Southeast Pacific waters. *Journal of Geophysical Research-Oceans, 115*

Bricaud, A., Morel, A., & Prieur, L. (1981). Absorption by dissolved organic matter of the sea (yellow substance) in the UV and visible domains. *Limnology and Oceanography, 26*, 43-53

Butler, J.J., Brown, S.W., Saunders, R.D., Johnson, B.C., Biggar, S.F., Zalewski, E.F., Markham, B.L., Gracey, P.N., Young, J.B., & Barnes, R.A. (2003). Radiometric measurement comparison on the integrating sphere source used to calibrate the Moderate Resolution Imaging Spectroradiometer (MODIS) and the Landsat 7 Enhanced Thematic Mapper Plus (ETM+). *Journal of Research of the National Bureau of Standards and Technology, 108*, 199-228

Cao, F., Fichot, C.G., Hooker, S.B., & Miller, W.L. (2014). Improved algorithms for accurate retrieval of UV/visible diffuse attenuation coefficients in optically complex, inshore waters. *Remote Sensing of Environment, 144*, 11-27

Carder, K.L., Steward, R.G., Harvey, G.R., & Ortner, P.B. (1989). Marine humic and fulvic acids: Their effects on remote sensing of ocean chlorophyll *Limnology and Oceanography, 34*, 68-81

Coles, V.J., Brooks, M.T., Hopkins, J., Stukel, M.R., Yager, P.L., & Hood, R.R. (2013). The pathways and properties of the Amazon River Plume in the tropical North Atlantic Ocean. *Journal of Geophysical Research: Oceans*

Defoin-Platel, M., & Chami, M. (2007). How ambiguous is the inverse problem of ocean color in coastal waters? *Journal of Geophysical Research: Oceans (1978–2012), 112*

Del Castillo, C.E., & Miller, R.L. (2008). On the use of ocean color remote sensing to measure the transport of dissolved organic carbon by the Mississippi River Plume. *Remote Sensing of Environment*, *112,* 836-844

Del Vecchio, R., & Blough, N.V. (2006). Influence of ultraviolet radiation on the chromophoric dissolved organic matter in natural waters. In F. Ghetti, G. Checcucci & J.F. Bornman (Eds.), *Environmental UV Radiation: Impact on Ecosystems and Human Health and Predictive Models* (pp. 203-216)

Fichot, C.G., & Benner, R. (2012). The spectral slope coefficient of chromophoric dissolved organic matter (S275-295) as a tracer of terrigenous dissolved organic carbon in river-influenced ocean margins. *Limnology and Oceanography, 57,* 1453-1466

Fichot, C.G., Kaiser, K., Hooker, S.B., Amon, R.M.W., Babin, M., Belanger, S., Walker, S.A., & Benner, R. (2013). Pan-Arctic distributions of continental runoff in the Arctic Ocean. *Scientific Reports, 3*

Fichot, C.G., Lohrenz, S.E., & Benner, R. (2014). Pulsed, cross-shelf export of terrigenous dissolved organic carbon to the Gulf of Mexico. *Journal of Geophysical Research: Oceans, 119,* 1176-1194

Fichot, C.G., & Miller, W.L. (2010). An approach to quantify depth-resolved marine photochemical fluxes using remote sensing: Application to carbon monoxide (CO) photoproduction. *Remote Sensing of Environment, 114*, 1363-1377

Fichot, C.G., Sathyendranath, S., & Miller, W.L. (2008). SeaUV and SeaUV(C): Algorithms for the retrieval of UV/Visible diffuse attenuation coefficients from ocean color. *Remote Sensing of Environment*, *112,* 1584-1602

Garver, S.A., & Siegel, D.A. (1997). Inherent optical property inversion of ocean color spectra and its biogeochemical interpretation .1. Time series from the Sargasso Sea. *Journal of Geophysical Research-Oceans, 102*, 18607-18625

Garver, S.A., Siegel, D.A., & Mitchell, B.G. (1994). Variability in near-surface particulate absorption spectra: What can a satellite ocean color imager see? *Limnology and Oceanography, 39*, 1349-1367

Gould, R.W., & Arnone, R.A. (1997). Remote sensing estimates of inherent optical properties in a coastal environment. *Remote Sensing of Environment, 61*, 290-301

Green, S.A., & Blough, N.V. (1994). Optical absorption and fluorescence properties of chromophoric dissolved organic matter in natural waters. *Limnology and Oceanography, 39*, 1903-1916

Helms, J.R., Stubbins, A., Perdue, E.M., Green, N.W., Chen, H., & Mopper, K. (2013). Photochemical bleaching of oceanic dissolved organic matter and its effect on absorption spectral slope and fluorescence. *Marine Chemistry, 155*, 81-91

Helms, J.R., Stubbins, A., Ritchie, J.D., Minor, E.C., Kieber, D.J., & Mopper, K. (2008). Absorption spectral slopes and slope ratios as indicators of molecular weight, source, and photobleaching of chromophoric dissolved organic matter. *Limnology and Oceanography, 53*, 955-969

Johannessen, S.C., Miller, W.L., & Cullen, J.J. (2003). Calculation of UV attenuation and colored dissolved organic matter absorption spectra from measurements of ocean color. *Journal of Geophysical Research-Oceans, 108*

Johnson, R.A., & Wichern, D.W. (2002). *Applied multivariate statistical analysis*: Prentice hall Upper Saddle River, NJ

Kirk, J.T. (1994). *Light and photosynthesis in aquatic ecosystems*: Cambridge university press

Lee, Z.P., Carder, K.L., & Arnone, R.A. (2002). Deriving inherent optical properties from water color: a multiband quasi-analytical algorithm for optically deep waters. *Applied Optics, 41*, 5755-5772

Lindell, M.J., Graneli, W., & Tranvik, L.J. (1995). Enhanced bacterial growth in response to photochemical transformation of dissolved organic matter. *Limnology and Oceanography, 40*, 195-199

Lubac, B., & Loisel, H. (2007). Variability and classification of remote sensing reflectance spectra in the eastern English Channel and southern North Sea. *Remote Sensing of Environment, 110,* 45-58

Mannino, A., Russ, M.E., & Hooker, S.B. (2008). Algorithm development and validation for satellite-derived distributions of DOC and CDOM in the US Middle Atlantic Bight. *J. Geophys. Res, 113*

Maritorena, S., Siegel, D.A., & Peterson, A.R. (2002). Optimization of a semianalytical ocean color model for global-scale applications. *Applied Optics, 41*, 2705-2714

Matsuoka, A., Hill, V., Huot, Y., Babin, M., & Bricaud, A. (2011). Seasonal variability in the light absorption properties of western Arctic waters: parameterization of the individual components of absorption for ocean color applications. *Journal of Geophysical Research: Oceans (1978–2012), 116*

Matsuoka, A., Huot, Y., Shimada, K., Saitoh, S., & Babin, M. (2007). Bio-optical characteristics of the western Arctic Ocean: implications for ocean color algorithms. *Canadian Journal of Remote Sensing, 33,* 503-518

Miller, W.L., & Moran, M.A. (1997). Interaction of photochemical and microbial processes in the degradation of refractory dissolved organic matter from a coastal marine environment. *Limnology and Oceanography, 42*, 1317-1324

Mitchell, B.G., & Holmhansen, O. (1991). Observations and modeling of the antarctic phytoplankton crop in relation to mixing depth. *Deep-Sea Research Part a-Oceanographic Research Papers, 38*, 981-1007

Montegut, C.D., Madec, G., Fischer, A.S., Lazar, A., & Iudicone, D. (2004). Mixed layer depth over the global ocean: An examination of profile data and a profile-based climatology. *Journal of Geophysical Research-Oceans, 109*

Mopper, K., & Kieber, D.J. (2000). *Marine photochemistry and its impact on carbon cycling The effects of UV radiation in the marine environment*: Cambridge University Press

Morel, A. (1988). Optical modeling of the upper ocean in relation to its biogenous matter content (case I waters). *Journal of Geophysical Research-Oceans, 93*, 10749-10768

Mueller, J.L. (1976). Ocean color spectra measured off the Oregon coast: characteristic vectors. *Applied Optics, 15*, 394-402

Nelson, N.B., & Siegel, D.A. (2002). Chromophoric DOM in the open ocean. In D.A. Hansell & C.A. Carlson (Eds.), *Biogeochemistry of marine dissolved organic matter* (pp. 547-578). Academic Press, San Diego, Calif.

Nelson, N.B., & Siegel, D.A. (2013). The Global Distribution and Dynamics of Chromophoric Dissolved Organic Matter. In C.A. Carlson & S.J. Giovannoni (Eds.), *Annual Review of Marine Science, Vol 5* (pp. 447-476)

Nelson, N.B., Siegel, D.A., & Michaels, A.F. (1998). Seasonal dynamics of colored dissolved material in the Sargasso Sea. *Deep-Sea Research Part I-Oceanographic Research Papers, 45*, 931-957

North, G.R., Bell, T.L., Cahalan, R.F., & Moeng, F.J. (1982). Sampling errors in the estimation of empirical orthogonal functions. *Monthly Weather Review, 110*, 699-706

Reader, H.E., & Miller, W.L. (2011). Effect of estimations of ultraviolet absorption spectra of chromophoric dissolved organic matter on the uncertainty of photochemical production calculations. *Journal of Geophysical Research-Oceans, 116*

Reader, H.E., & Miller, W.L. (2014). The efficiency and spectral photon dose dependence of photochemically induced changes to the bioavailability of dissolved organic carbon. *Limnol. Oceanogr, 59*, 182-194

Reynolds, R.A., Stramski, D., & Mitchell, B.G. (2001). A chlorophyll-dependent semianalytical reflectance model derived from field measurements of absorption and backscattering coefficients within the Southern Ocean. *Journal of Geophysical Research: Oceans (1978–2012), 106,* 7125-7138

Siegel, D.A., Maritorena, S., Nelson, N.B., Hansell, D.A., & Lorenzi-Kayser, M. (2002). Global distribution and dynamics of colored dissolved and detrital organic materials. *Journal of Geophysical Research-Oceans, 107*

Siegel, D.A., Wang, M., Maritorena, S., & Robinson, W.D. (2000). Atmospheric correction of satellite ocean color imagery: the black pixel assumption. *Applied Optics, 39,* 3582-3591

Stedmon, C.A., Markager, S., & Kaas, H. (2000). Optical Properties and Signatures of Chromophoric Dissolved Organic Matter (CDOM) in Danish Coastal Waters. *Estuarine, Coastal and Shelf Science, 51,* 267-278

Stramski, D., Reynolds, R.A., Babin, M., Kaczmarek, S., Lewis, M.R., Röttgers, R., Sciandra, A., Stramska, M., Twardowski, M.S., & Franz, B.A. (2008). Relationships between the surface concentration of particulate organic carbon and optical properties in the eastern South Pacific and eastern Atlantic Oceans. *Biogeosciences, 5,* 171-201

Stubbins, A., Niggemann, J., & Dittmar, T. (2012). Photo-lability of deep ocean dissolved black carbon. *Biogeosciences, 9,* 1661-1670

Swan, C.M., Nelson, N.B., Siegel, D.A., & Fields, E.A. (2013). A model for remote estimation of ultraviolet absorption by chromophoric dissolved organic matter based on the global distribution of spectral slope. *Remote Sensing of Environment, 136,* 277-285

Swan, C.M., Siegel, D.A., Nelson, N.B., Carlson, C.A., & Nasir, E. (2009). Biogeochemical and hydrographic controls on chromophoric dissolved organic matter distribution in the Pacific Ocean. *Deep-Sea Research Part I-Oceanographic Research Papers, 56,* 2175-2192

Szeto, M., Werdell, P.J., Moore, T.S., & Campbell, J.W. (2011). Are the world's oceans optically different? *Journal of Geophysical Research-Oceans, 116*

Tedetti, M., & Sempere, R. (2006). Penetration of ultraviolet radiation in the marine environment. A review. *Photochemistry and Photobiology, 82,* 389-397

Toole, D.A., & Siegel, D.A. (2001). Modes and mechanisms of ocean color variability in the Santa Barbara Channel. *Journal of Geophysical Research-Oceans, 106,* 26985-27000

Twardowski, M.S., Boss, E., Sullivan, J.M., & Donaghay, P.L. (2004). Modeling the spectral shape of absorption by chromophoric dissolved organic matter. *Marine Chemistry, 89,* 69-88

Vähätalo, A.V., & Wetzel, R.G. (2004). Photochemical and microbial decomposition of chromophoric dissolved organic matter during long (months-years) exposures. *Marine Chemistry, 89*, 313-326

Werdell, P.J., & Bailey, S.W. (2005). An improved in-situ bio-optical data set for ocean color algorithm development and satellite data product validation. *Remote Sensing of Environment, 98*, 122-140

Yamashita, Y., Nosaka, Y., Suzuki, K., Ogawa, H., Takahashi, K., & Saito, H. (2013). Photobleaching as a factor controlling spectral characteristics of chromophoric dissolved organic matter in open ocean. *Biogeosciences, 10*, 7207-7217

Zepp, R.G., Erickson-III, D.J., Paul, N.D., & Sulzberger, B. (2007). Interactive effects of solar UV radiation and climate change on biogeochemical cycling. *Photochemical & Photobiological Sciences, 6*, 286-300

Table 3.1: List of Abbreviations and Acronyms

Symbol	Description	Unit
a_g	absorption coefficient of chromophoric dissolved organic matter	(m^{-1})
a_{dg}	absorption coefficient of non-algal particles and chromophoric dissolved organic matter	(m^{-1})
a_{NAP}	absorption coefficient of non-algal particles	(m^{-1})
A	absorbance (optical density) of CDOM	
AOPs	apparent optical properties	
b_{bp}	backscattering coefficient of particles	(m^{-1})
CDM	colored detrital material (non-algal particles + chromophoric dissolved organic matter)	
CDOM	chromophoric dissolved organic matter	
$E_d(\lambda, 0^-)$	downwelling irradiance just beneath the sea surface	$\mu W/cm^2/nm$
$E_d(\lambda, 0^+)$	downwelling (incident) irradiance just above the sea surface	$\mu W/cm^2/nm$
IOPs	inherent optical properties	
K_d	diffuse attenuation coefficient	(m^{-1})
$L_u(\lambda, 0^-)$	upwelling radiance just beneath the sea surface	$\mu W/cm^2/nm/sr^{-1}$
$L_w(\lambda)$	water-leaving radiance	$\mu W/cm^2/nm/sr^{-1}$
NAP	non-algal particles	
R_{rs}	remote sensing reflectance	(sr^{-1})
$S_{\lambda 1-\lambda 2}$	exponential slope parameter for CDOM absorption over the spectral range of λ_1- λ_2	(nm^{-1})

Table 3.2: Training Data Sets used to develop the Sea*CDOM* algorithm[a].

Index	Experiments	Locations	No. of Samples	Date	$a_g(300)$ (m^{-1}) [min, max]	References or PIs
1	AMMA	Equatorial Atlantic near 23° W	4	Jun-July, 2006	[0.18, 0.26]	N. Nelson & D. Siegel
2	AMLR	Southern Drake Passage near Antarctic Peninsula	45	2004; 2006-2008	[0.22, 0.97]	G. Mitchell
3	Big_Bend	Big bend region in Florida	82	2011	[16.7, 0.9]	C. Hu
4	CCE-LTER	Upwelling regime off California	20	Apr, 2007; Oct, 2008	[0.37, 1.07]	G. Mitchell
5	CLIVAR - A20	North Atlantic Ocean along 52 °W	4	Oct, 2003	[0.11, 0.83]	N. Nelson & D. Siegel
	A22	North Atlantic Ocean along 66 °W	6	Oct-Nov, 2003	[0.12, 0.77]	[Nelson et al., 2010]
		Indian Ocean and Southern Ocean	28	Feb-Apr, 2007	[0.09, 0.21]	
	I8SI9N	Meridional South Pacific along 150 °W	3	Jan, 2005	[0.07, 0.15]	
	P16S	Eastern Pacific and Southern Ocean	36	2007-2008	[0.08, 0.36]	
	P18					
6	coastal_GA	Estuaries along Georgia coast	97	2007-2011	[0.73, 30.4]	W. Miller
7	GEOCAPE - CBODAQ	Chesapeake Bay	45	July, 2011	[4.9, 7.0]	A. Mannino & C. Hu
8	ICESCAPE	Beaufort and Chukchi Sea	20	Jun-July, 2010	[0.56, 11.9]	S. Hooker & G. Mitchell
9	SWFL	Southwest Florida shelf	17	2010; 2011	[0.9, 18.3]	C. Hu
10	Tampa_Bay	Tampa Bay in Florida	68	2010-2012	[4.8, 38.2]	C. Hu

[a] Abbreviations for Experiments: AMMA = African Monsoon Multidisciplinary Analyses; AMLR = Antarctic Marine Living Resources; Big Bend = cruises in the big bend region in Northwest Florida, US; CCE-LTER = California Current Ecosystem LTER; CLIVAR = Climate Variability and Predictability; ICESCAPE = Impacts of Climate on the Eco-Systems and Chemistry of the Arctic Pacific Environment; coastal_GA = cruises along the coast of Georgia, US; Tampa_Bay = experiments conducted in Tampa Bay, FL, US; SWFL = Southwest Florida shelf, FL, US; GEOCAPE-CBODAQ = GEOstationary Coastal and Air Pollution Events - Chesapeake Bay Oceanographic Campaign with Discover AQ;

Table 3.3: Data Sets used in validation of the Sea*CDOM* algorithm[b].

Index	Experiments	Locations	No. of Samples	Date	$a_g(300)$ (m^{-1}) [min, max]	References or PIs
1	GulfCarbon	Northern Gulf of Mexico (NGoM)	42	Jan 2009-Mar 2010	[0.22, 4.1]	[*Fichot and Benner*, 2011, 2012]
2	MALINA	Arctic Ocean	20	Aug 2009	[0.51, 13]	S. Hooker
3	BIOSOPE	Southeast Pacific	24	Oct-Dec, 2004	[0.06, 0.27]	[*Bricaud et al.*, 2010]

[b] Abbreviations for Experiments: GulfCarbon = cruises conducted during the GuflCarbon project, northern Gulf of Mexico; MALINA = the *R/V CCGS Amundsen* expedition to the southern Beaufort Sea and shelf adjacent to the Mackenzie River outlet (available from http://malina.obs-vlfr.fr/index.html); BIOSOPE = BIogeochemistry and Optics South Pacific Experiment (available from http://www.obs-vlfr.fr/proof/vt/op/ec/biosope/bio.htm).

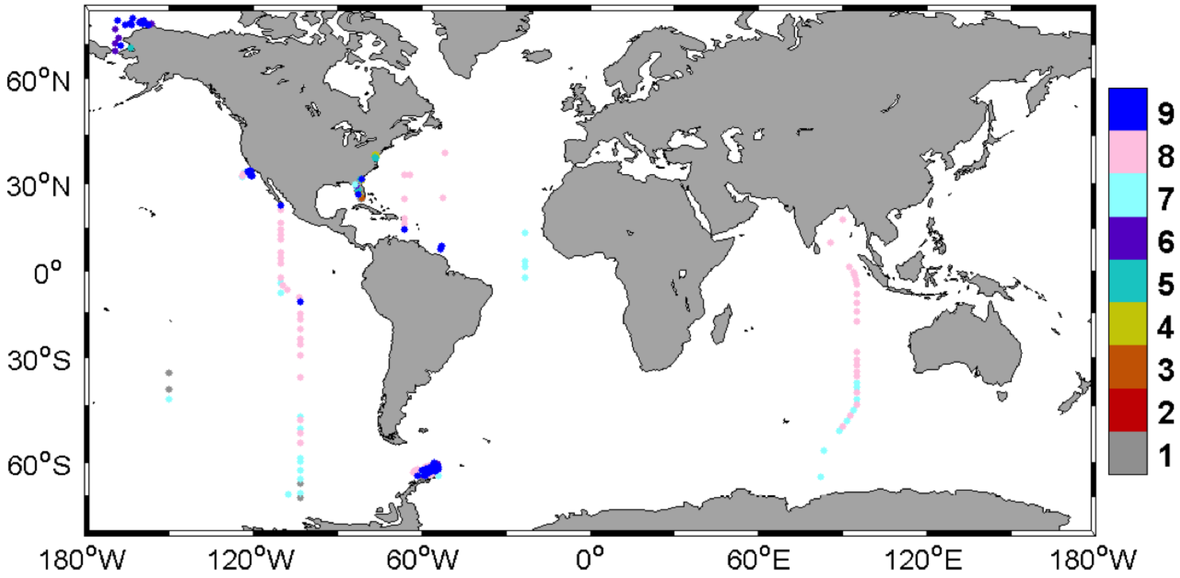

Figure 3.1: Sampling locations of *in situ* R_{rs} and CDOM absorption spectra in the training data set (N = 474). Colors on the location represent the assignments of sample points into distinct ocean color clusters as indicated with the color bar on the right.

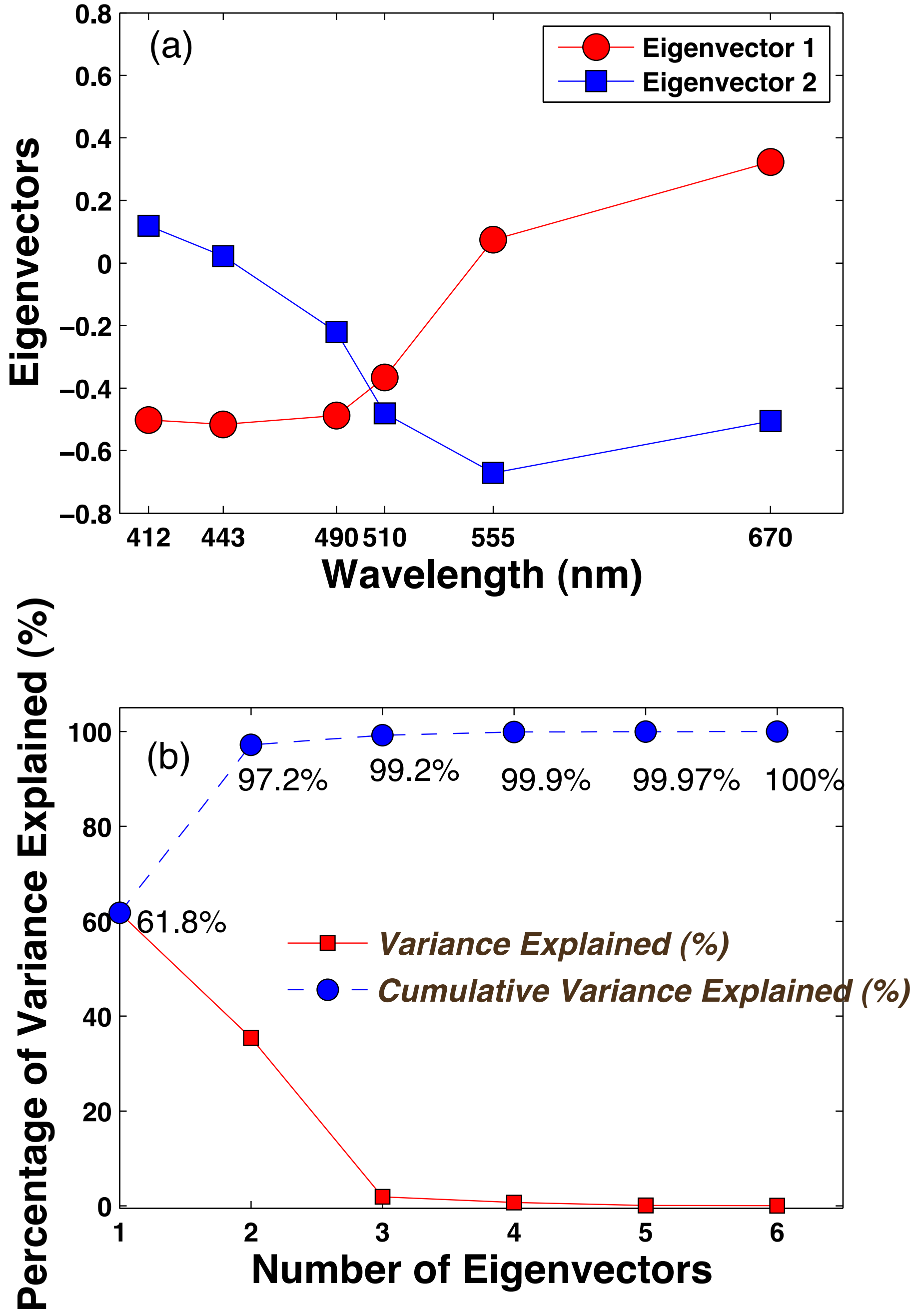

Figure 3.2: Results of (a) the first two eigenvectors of the correlation matrix $\boldsymbol{\rho}$ derived from multispectral R_{rs}; (b) contribution of each eigenvector to the total variance in $\boldsymbol{A}$.

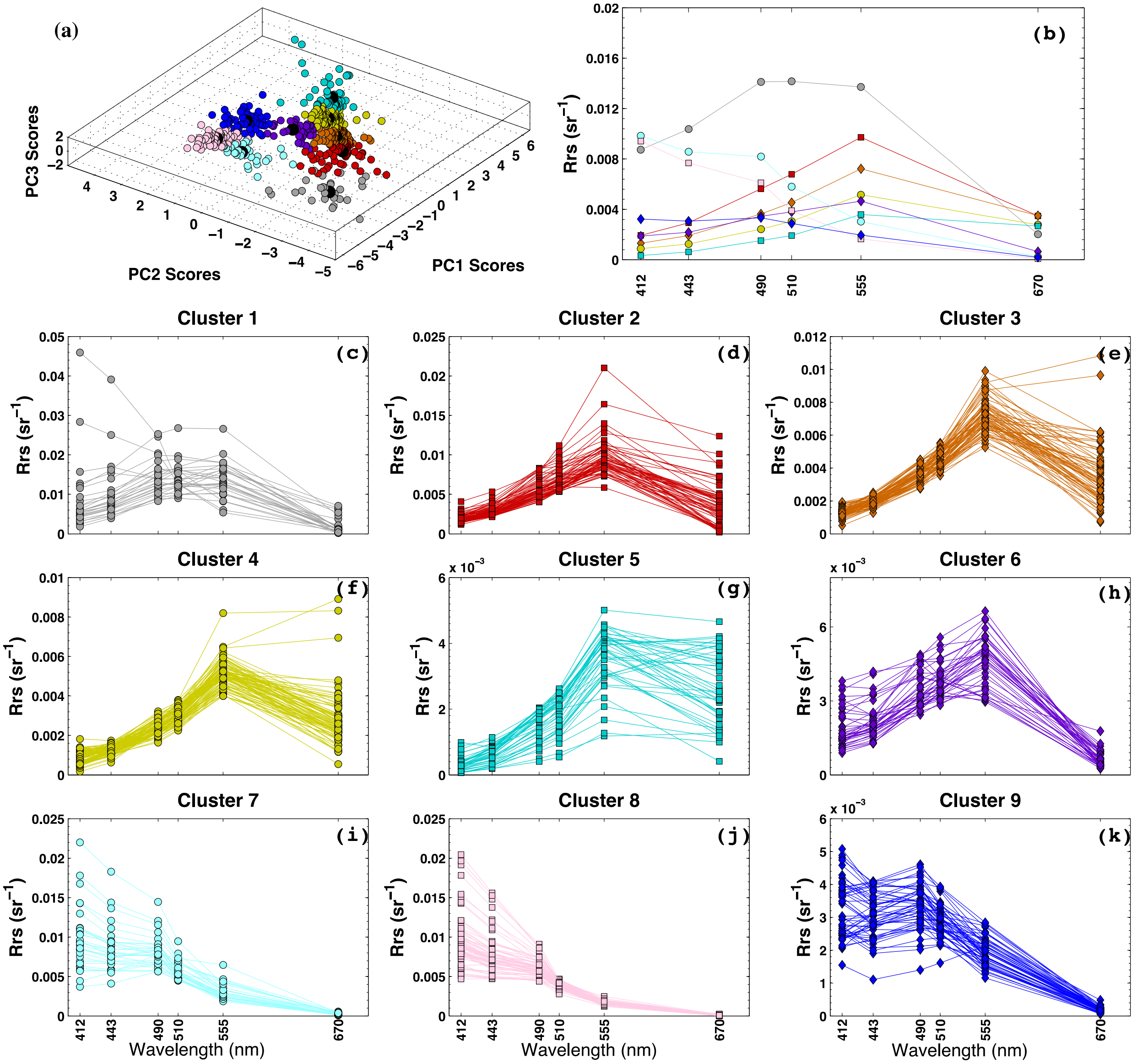

Figure 3.3: (a) Nine clusters of R_{rs} spectra derived from fuzzy *c*-means cluster analysis, black circles denote cluster centers; (b) Mean R_{rs} spectra in each cluster; (c)-(k) Respective R_{rs} spectra classified in each ocean color cluster.

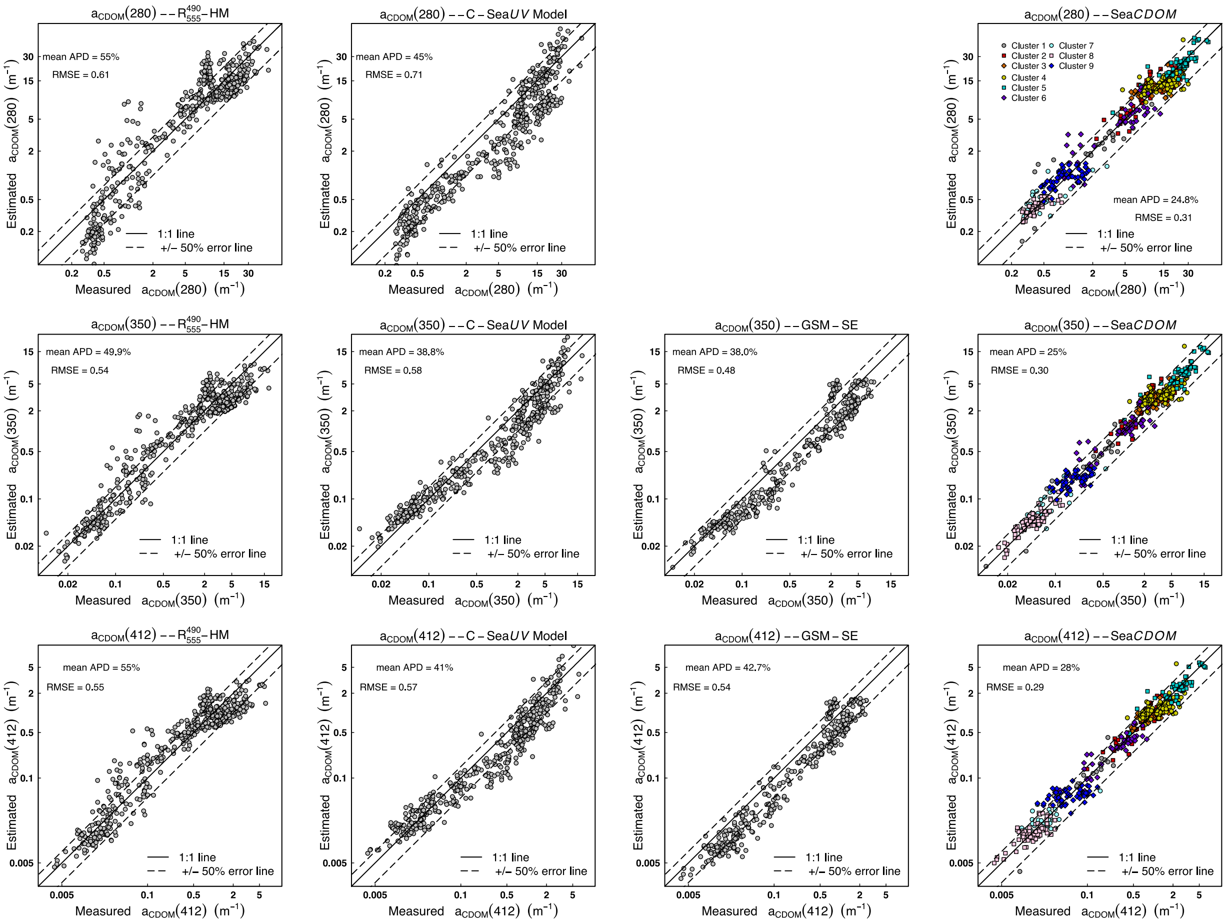

Figure 3.4: Comparison of measured *in situ* $a_g(\lambda)$ with estimated $a_g(\lambda)$ derived from the four algorithms at $\lambda = 280$, 350, and 412 nm. Note that the GSM-SE algorithm was developed for wavelengths beyond 325 nm and thus we did not test its performance for $\lambda = 280$ nm.

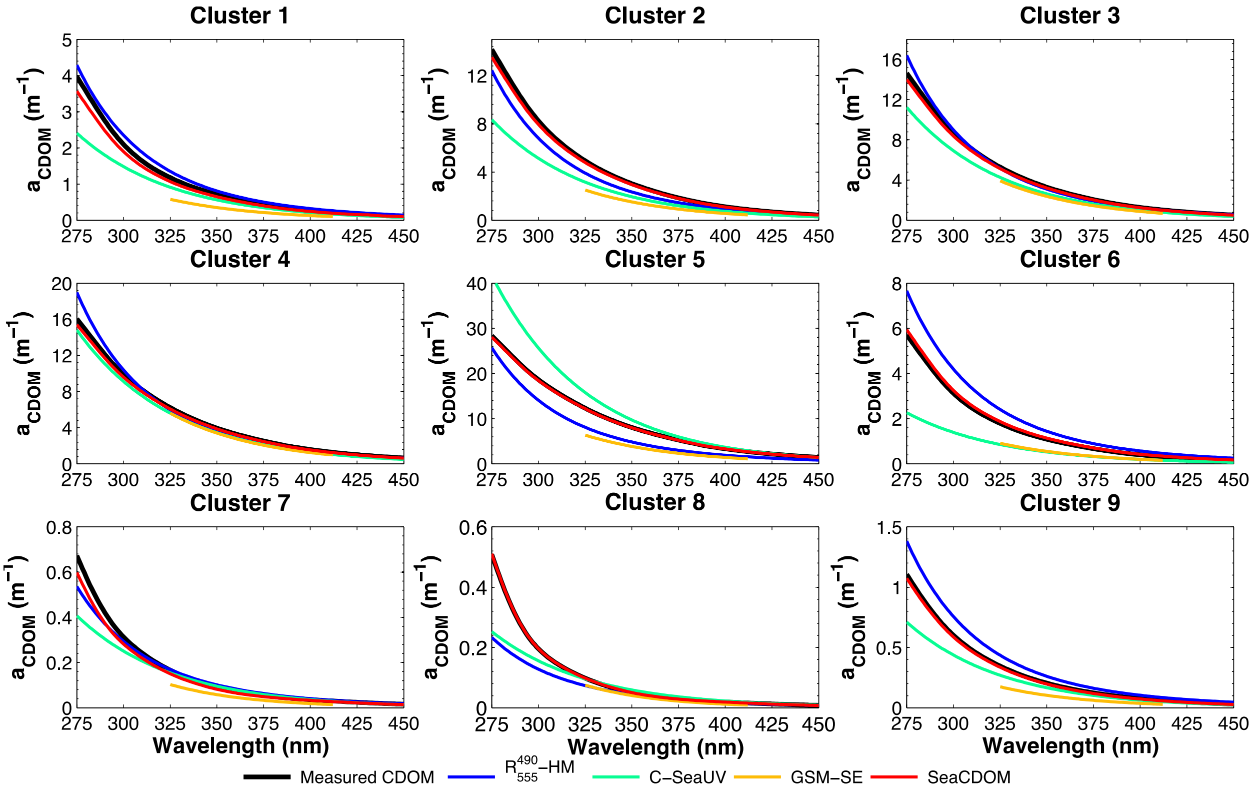

Figure 3.5: Comparison of the mean fully-resolved CDOM absorption spectra derived from the four algorithms in the range of 275-450 nm for each cluster.

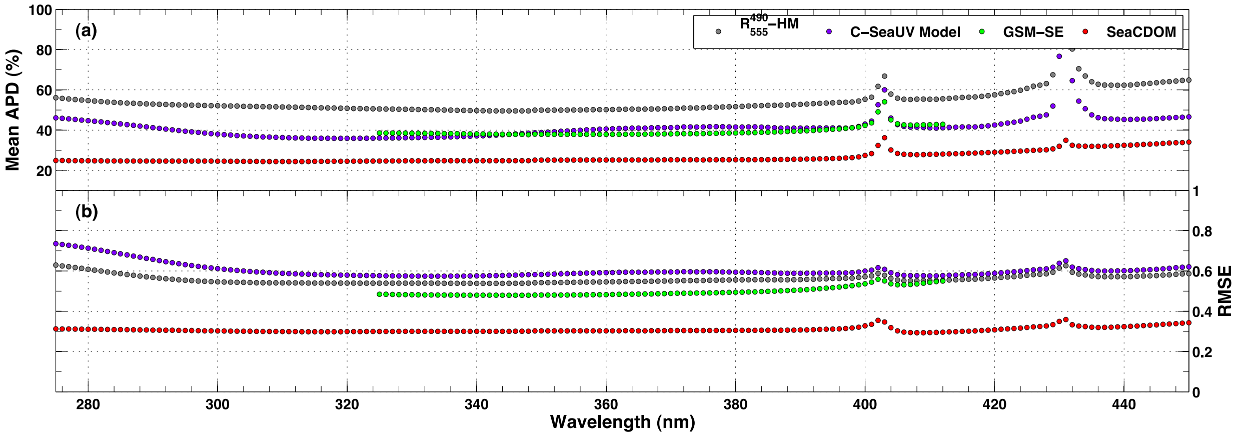

Figure 3.6: Statistical results of (a) mean APD and (b) RMSE for the retrieval of $a_g(\lambda)$ from the four algorithms in the range of 275-450 nm. Note that anomalies at 404 and 430 nm are not a function of algorithms but rather result from original spectrophotometer spectra contained in the database used for training.

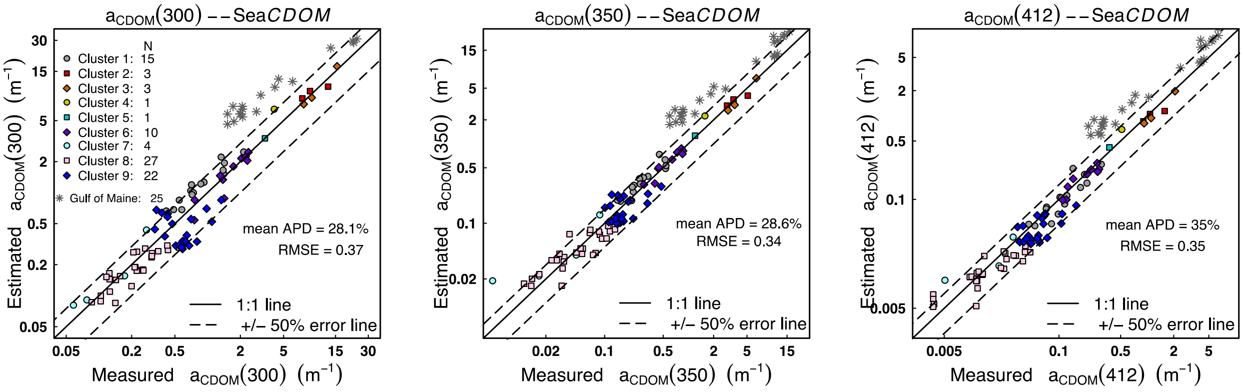

Figure 3.7: Performance evaluation of the Sea*CDOM* algorithm in estimating a_g at λ = 300, 350, and 412 nm for the three independent validation data sets in Table 3, with mean APD and RMSE (N = 86) were reported in black. Color-coded symbols mark the assignments of samples to each of the nine clusters and are the same as in Figure 3.4. The grey asterisks denote the poor performance in retrieving a_g for waters in the Gulf of Maine (N = 25), and discussions were included in section 4.1.

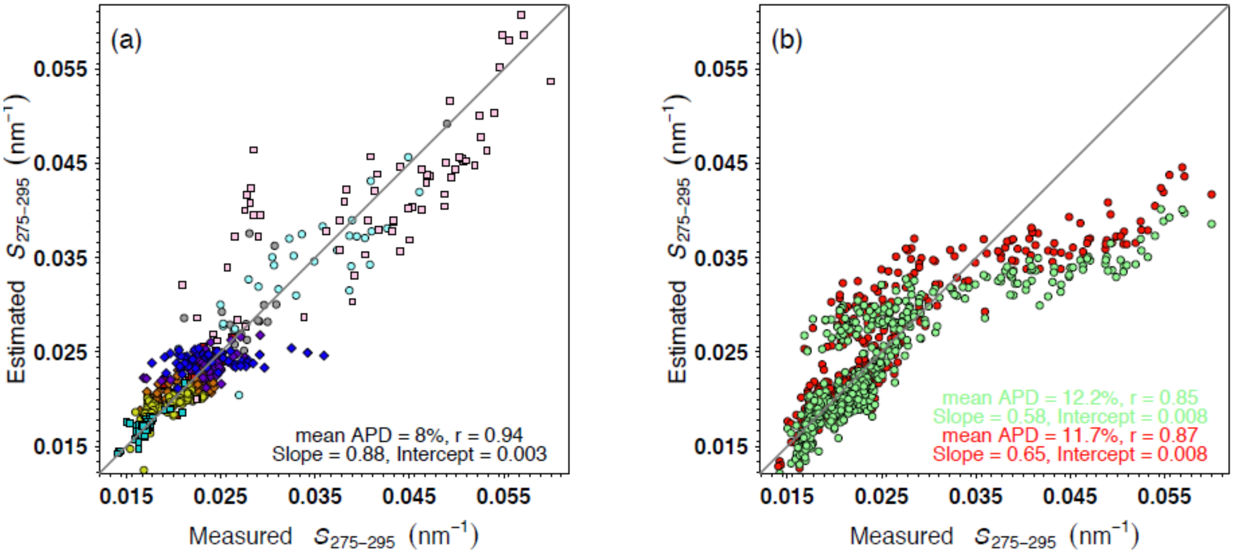

Figure 3.8: Scatter plots of the calculated $S_{275\text{-}295}$ of measured a_g verses calculated $S_{275\text{-}295}$ derived from (a) the Sea*CDOM* algorithm; symbols and legends are the same as in Figure 4; (b) the algorithm (lightgreen) published in Fichot et al. (2013) (with fitting parameters as: $\alpha = -3.4567$, $\beta = 0.4299$, $\gamma = 0.0924$, $\delta = -1.2649$, $\varepsilon = 0.8885$, and $\zeta = -0.1025$ in Eq. (15)) and the approach (red) proposed in Fichot et al. (2013) (with fitting parameters tuned for our training data set resulted as: $\alpha = -3.0230$, $\beta = 0.3101$, $\gamma = 0.0732$, $\delta = -0.4528$, $\varepsilon = 0.2078$, and $\zeta = -0.0309$ in Eq. (15)). Solid gray line represents the 1:1 correlation.

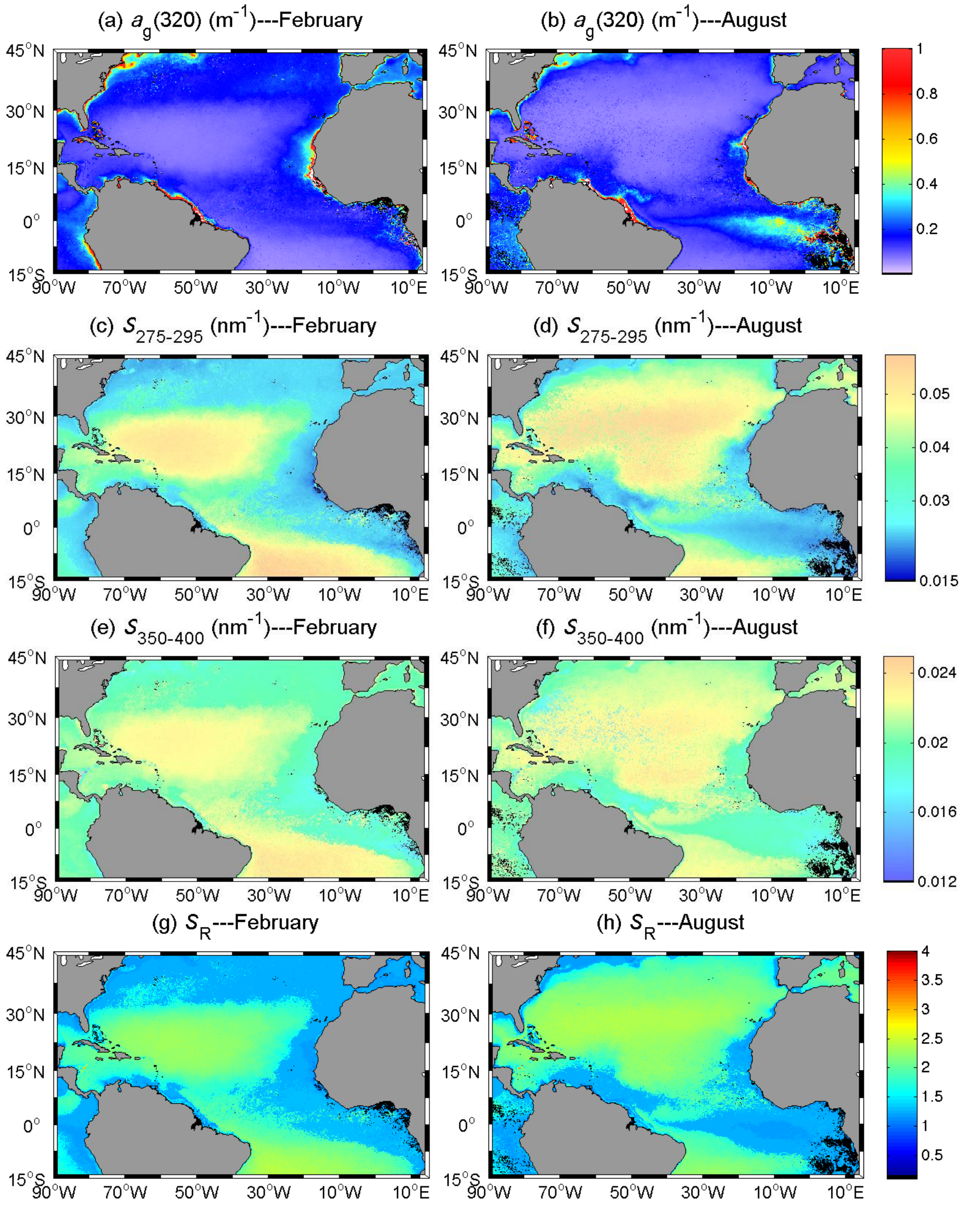
(a) $a_g(320)$ (m^{-1})---February

(b) $a_g(320)$ (m^{-1})---August

(c) $S_{275\text{-}295}$ (nm^{-1})---February

(d) $S_{275\text{-}295}$ (nm^{-1})---August

(e) $S_{350\text{-}400}$ (nm^{-1})---February

(f) $S_{350\text{-}400}$ (nm^{-1})---August

(g) S_R---February

(h) S_R---August

Figure 3.9: Ten-year (2001-2010) monthly climatologies derived from Sea*CDOM* application to SeaWiFS data. $a_g(320)$ in (a) February and (b) August; $S_{275\text{-}295}$ for (c) February and (d) August; $S_{350\text{-}400}$ for (e) February and (f) August; S_R for (g) February and (h) August.

CHAPTER 4

BLENDING TWO OCEAN COLOR ALGORITHMS TO EVALUATE ULTRAVIOLET (UV) OPTICS AND PHOTOCHEMISTRY USING THE HYPERSPECTRAL IMAGER FOR THE COASTAL OCEAN (HICO)[4]

---

[4] Cao, F., and W. L. Miller. To be submitted to *Remote Sensing of Environment.*

Abstract

Knowledge of light partition into different optically active constituents particularly chromophoric dissolved organic matter (CDOM) in the ultraviolet (UV) is indispensible for understanding UV dependent biogeochemical issues including photochemical processes in optically complex waters. Herein a new approach is presented to investigate photochemistry by blending two ocean color algorithms, namely the composite Sea*UV* [*Cao et al.*, 2014] and the Sea*CDOM* [*Cao and Miller*, 2014] algorithms, to visible remote sensing reflectance measured using the Hyperspectral Imager for the Coastal Ocean (HICO). As exemplified with photoproduced carbon monoxide (CO) from CDOM photodegradation, we model CO photoproduction at specific depth as well as integrating over the water column and elucidate the mechanism regulating the depth-integrated photoproduction rates in the UV in a dynamic coastal environment. Decoupled retrieval of bio-optical properties such as the diffuse attenuation coefficient (K_d) and CDOM absorption coefficient (a_g) in the UV from ocean color observations allows a synoptically dynamic view of CDOM contribution to total light attenuation (a_g/K_d) and will have potential to probe UV processes on regional as well as global scales using remote sensing of ocean color.

1. Introduction

Estuarine and coastal waters function as critical interfaces between terrestrial and marine systems. Despite covering a small area compared to the global ocean, coastal waters play an active role in regulating carbon (C) fluxes and transformations [*Bauer et al.*, 2013]. Dissolved organic matter (DOM) delivered by rivers is estimated to be ~0.25 Gt C per year and a large fraction of this riverine DOM must be remineralized during transport to the open ocean via multiple physical and biogeochemical processes [*Cauwet*, 2002]. Among these, ultraviolet (UV) photochemistry is a crucial sink for photo-labile chromophoric dissolved organic matter (CDOM), producing new bioavailable organic materials and environmentally important inorganic and organic carbon species (e.g., carbon monoxide (CO), carbon dioxide, carbonyl sulfide, etc.) [*Blough and Del Vecchio*, 2002; *Mopper and Kieber*, 2002]. On the other hand, photochemical breakdown of CDOM, by influencing underwater UV irradiance, could have ecological consequences, affecting phytoplankton assemblages [*Domingues et al.*, 2014], resulting in photoacclimation and adaption [*Neale et al.*, 1998]. Since UV light is responsible for CDOM photochemistry, understanding the coastal carbon cycle requires a detailed knowledge of UV processes and related biogeochemical modifications of CDOM in coastal waters.

Progress in satellite sensor development such as the Hyperspectral Imager for the Coastal Ocean (HICO) provides a unique opportunity to assess coastal processes [*Lucke et al.*, 2011]. Its enhanced spatial resolution (~ 96 meters at nadir) makes it well suited for providing spatial details of coastal features and studies have begun to demonstrate its potential for examining phytoplankton ecology [*Ryan et al.*, 2014], chlorophyll relevant index [*Mishra et al.*, 2014], and coastal bathymetry [*Garcia et al.*, 2014]. While this powerful tool creates opportunity to understand fine-scale processes with explicit descriptions of spatial complexity, to our knowledge, application of HICO imagery has not been used to model photochemical processes in near–shore environments.

Modeling photochemistry driven by UV–CDOM interactions in highly dynamic coastal waters has been challenging yet potentially retrievable from ocean color. Herein we introduce a new approach that employs two distinct ocean color algorithms that retrieve UV attenuation (Sea*UV* ; [*Cao et al.*, 2014]) and CDOM absorbance (Sea*CDOM*; [*Cao and Miller*, 2014]) from a single coastal HICO image centered on Sapelo Island, GA, USA, to estimate photochemical fluxes using CO photoproduction as an example. We demonstrate HICO's potential to address both biogeochemical processes and mechanisms regulating UV–dependent photochemistry in a highly dynamic estuarine system by modeling depth–specific and depth–integrated CO photoproduction from one HICO scene.

2. Background

Quantitative modeling of depth-specific CO photoproduction rates (hereafter $\mathit{\Psi}_{\mathrm{CO}}(z)$, where z denotes depth) from ocean color, requires knowledge of four parameters [*Fichot and Miller*, 2010]. They are (1) the incident radiant energy as spectral downwelling scalar irradiance just below the sea surface ($E_{\mathrm{od}}(\lambda,0^{-})$, mol (photons) m^{-2} s^{-1} nm^{-1}), (2) the diffuse attenuation coefficient of downward irradiance (K_{d}, m^{-1}), (3) the absorption coefficient of CDOM (a_{g}, m^{-1}), and (4) the photochemical efficiency of the reaction in question. As in *Fichot and Miller* [2010], the reaction considered here is CO production via CDOM photolysis. Efficiency is described using an apparent quantum yield (AQY, hereafter ϕ_{CO}, mol (CO) mol (photons) $^{-1}$), calculated as moles of CO formed per mole photons absorbed by CDOM. CO photoproduction rates can therefore be calculated over the entire photoreactive spectrum as in equation (1),

$$\mathit{\Psi}_{\mathrm{co}}(z) = \int_{\lambda_{min}}^{\lambda_{max}} E_{\mathrm{od}}(\lambda, 0^{-}) \times \exp(-K_{\mathrm{d}}(\lambda) \times z) \times a_{\mathrm{g}}(\lambda, z) \times \phi_{\mathrm{CO}}(\lambda, z) \mathrm{d}\lambda \tag{1}$$

where $\mathit{\Psi}_{\mathrm{CO}}(z)$ (mol (CO) m^{-3} s^{-1}) is the CO photoproduction rate at depth z (m), and λ_{min} and λ_{max} are the minimal and maximal wavelength (nm) respectively over which the production is integrated. Assuming vertical homogeneity in each ocean color pixel, $\mathit{\Psi}_{\mathrm{CO}}(z)$ is fundamentally a function of two optical (K_{d}, a_{g}) and one photochemical (ϕ_{CO}) properties, with optical terms retrievable from remote sensing and the photochemical term typically based on laboratory determinations. Hence, robust retrieval of these optical parameters in the wavelength range of photochemical production (i.e., UV) is essential for accurate quantification of marine photochemical fluxes based on ocean color.

Even though photochemical reactions are acknowledged as important in many marine chemical cycles, few studies have made synoptic estimates of marine photochemistry using remote sensing [e.g., *Bélanger et al.*, 2008; *Xie et al.*, 2012]. Notably, *Fichot and Miller* [2010] proposed a "practical" model (using equation (1)) to quantify depth–specific photochemical fluxes with the Sea*UV* algorithms [*Fichot et al.*, 2008] and ocean color climatology to give a global estimate of CO photoproduction. This approach, hereafter referred to as the "FM" approach", is highly idealized, but nonetheless serves as a good starting point for understanding photochemical processes occurring in the water column. There are, however, several significant limitations when applying the FM approach to coastal waters. The *Fichot et al.* [2008] Sea*UV* algorithms, developed with few high CDOM samples, significantly underestimates K_d(UV) for darker inshore waters (see Figure 4 in *Cao et al.* [2014]). Also the FM approach retrieved CDOM absorption coefficients at 320 nm ($a_g(320)$) from modeled K_d using a fixed $a_g(320)/K_d(320)$ ratio of 0.68 (equation (2)) derived from limited marine samples and this could be very different for near–shore waters

$$a_g(320) = 0.68 \times K_d(320) \tag{2}$$

Further, modeling a_g at other wavelengths required use of a pre-defined CDOM spectral slope coefficient (S) that is known to vary, especially in terrestrial–influenced coastal waters. These assumptions create uncertainties leading to erroneous results in estimating the UV optical properties required for photochemical calculations.

Improved performance over the FM approach is now possible as ocean color algorithms that retrieve UV optical properties have matured. *Cao et al.* [2014] extended the original Sea*UV* algorithms to better characterize complex coastal/inshore waters, and presented a composite set of Sea*UV* algorithms that apply universally to all water types. *Cao and Miller* [2014] further improved algorithms to allow direct estimates of spectrally–resolved CDOM spectra (275-450 nm) from ocean color. Together, these improvements allow an estimation of $K_d(340)$ and $a_g(340)$ with uncertainties of ±15% and ±25%, respectively. Our modeling approach for the HICO image here is similar to the FM approach, but with UV optical properties retrieved using improved ocean color algorithms that allow emphasis on dynamic coastal areas.

3. Methods

3.1. Study area and HICO data

This study was focused on the Georgia coast (Figure 4.1 (a)), USA, spanning roughly from -81.7°E to -80.6°E and from 30.8°N to 31.9°N encompassing three distinct estuarine systems (Altamaha, Doboy, and Sapelo Sounds). A detailed description of hydrological patterns in these three adjacent estuaries can be found in *Cao et al.* [2014]. Overall, this coastal estuarine system is optically deep, landward edged with extensive intertidal marsh habitats that export substantial amounts of organic matter to the coastal ocean.

One HICO image (scene ID: 12459, Figure 4.1 (b)) was acquired on January 18th, 2013, under mostly clear sky conditions (http://hico.coas.oregonstate.edu/). Atmospheric correction was made by applying the ATmosphere REMoval algorithm developed by the Naval Research Laboratory, followed by an empirical sun glint and cloud removal [*B-C Gao and Davis*, 1997]. Because the optical algorithms applied thereafter are initially developed with the multispectral Sea-Viewing Wide Field-of-View Sensor (SeaWiFS) platform, we obtained R_{rs} at SeaWiFS wavebands centered at λ = 412, 443, 490, 510, 555, and 670 nm by interpolating R_{rs} at corresponding atmospherically corrected HICO wavelengths.

3.2. Modeling procedures

Our model incorporated several assumptions from the FM approach, including (1) UV wavelengths from 290–490 nm are responsible for photochemical reactions involving CDOM, (2) total solar scalar irradiance is approximated by solar downwelling scalar irradiance ($E_{od}(\lambda,0^-)$) and upwelling irradiance is negligible, and (3) attenuation of downwelling scalar irradiance can be approximated with $K_d(\lambda)$. Derivations of input parameters and analysis of the resulting uncertainty (section 5.1) are discussed below.

3.2.1. Spectral solar downwelling scalar irradiance ($E_{0d}(\lambda,0^-)$)

$E_{0d}(\lambda,0^-)$ is derived from spectral solar downwelling irradiance ($E_d(\lambda,0^+)$), which was modeled using the Simple Model of the Atmospheric Radiative Transfer of Sunshine model (SMARTS, version 2.9.2; http://www.nrel.gov/rredc/smarts/), considered to be a robust prediction of solar spectral irradiance, especially in the UV wavelengths [*Stubbins et al.*, 2006]. SMARTS outputs both direct and diffuse components of global solar spectral irradiance with a 0.5 nm spectral resolution over the photoreactive wavelength range of 290-400 nm and a 1.0 nm resolution between 401-480 nm. We limited our use of SMATRS output to the photoreactive wavelength range in 290–450 nm, calculating spectral solar downwelling irradiance just below the sea surface with the approximation: $E_d(\lambda,0^-) \approx 0.97 \times E_d(\lambda,0^+)$. $E_{0d}(\lambda,0^-)$ was then calculated by applying a conversion factor ($\bar{\mu}_d$) to modeled $E_d(\lambda,0^-)$. $\bar{\mu}_d$ accounts for the cosine effect of the downwelling irradiance fields and can be estimated as in equation (3) according to *Prieur and Sathyendranath* [1981]:

$$\frac{1}{\bar{\mu}_d} = \frac{0.6}{\cos(\theta(t))} + \frac{0.4}{0.859} \qquad (3)$$

where $\bar{\mu}_d$ is the mean cosine for $E_d(\lambda,0^-)$ in the surface ocean and $\cos(\theta(t))$ is the cosine of the solar zenith angle θ at time t. The desired $E_{0d}(\lambda,0^-)$ (Figure 4.2 (a)) can be obtained as: $E_{0d}(\lambda,0^-) \approx E_d(\lambda,0^-)/\bar{\mu}_d$.

3.2.2. Derivation of optical properties

Downward diffuse attenuation coefficients $K_d(\lambda)$ at discrete UV and visible wavelengths (i.e., λ = 320, 340, 380, 412, 443, and 490 nm) were estimated from visible R_{rs} using the composite Sea*UV* algorithms as detailed in *Cao et al.* [2014]. K_d (λ) from 320 to 450 nm was subsequently derived at 5 nm intervals with a cubic interpolation and extrapolated into the UV-B (λ = 290–320 nm) assuming an exponential increase of K_d over decreasing wavelengths and a spectral slope value calculated using $K_d(320)$ and $K_d(340)$. Spectrally resolved CDOM absorption coefficients a_g(290–450 nm; 5 nm resolution) were modeled using the Sea*CDOM* algorithm [*Cao and Miller*, 2014].

3.2.3. Determination of AQY spectra for CO ($\phi_{CO}(\lambda)$)

Previous seasonal studies have shown the photochemical efficiency of CO production in coastal Georgia estuarine waters to be fairly well constrained [*Reader and Miller*, 2012]. Here we add four more CO AQY spectra to the *Reader and Miller* [2012] data set from samples collected within the study area in May 2013. All laboratory irradiations, optical measurements, and modeling of CO AQY were performed as described in *Reader and Miller* [2012]. New CO AQY determined here compare well with prior measurements (Figure 4.2 (d)) and argues that coastal Georgia waters can likely be modeled with a single CO AQY spectrum, representative for our small-scale study area within observed error. The single CO AQY spectra used to model CO photochemistry obtained from the total 41 spectra is displayed in equation (4):

$$\emptyset_{CO}(\lambda) = \exp\left(-8.216 + 0.034 \times (\lambda - 269.54)\right) \tag{4}$$

To compare results in this study to those of previous work, CO photoproduction rate (nmol (CO) m^{-3} s^{-1}) was upscaled to hourly production (nmol (CO) m^{-3} h^{-1}), assuming that irradiance intensity and optical properties remain constant within a one hour time window over the entire study area.

3.2.4. Computation of depth-integrated CO photoproduction rate (P_{CO}) and Calculation of differences in P_{CO} using two different approaches

Depth-integrated CO photoproduction rates using the approach described for this study (hereafter P_{CO}^{BL}, nmol (CO) m^{-2} h^{-1}) was calculated with a trapezoidal integral method, assuming a homogeneous distribution of CDOM throughout the photic zone for each pixel. The effects of using the composite SeaUV and SeaCDOM algorithms to estimate P_{CO} relative to those in the FM approach and its subsequent derivation of a_g (hereafter P_{CO}^{FM}, nmol (CO) m^{-2} h^{-1}), were examined by calculating P_{CO} using both approaches. For this, we implemented the Sea*UV* algorithms exactly as described by *Fichot et al.* [2008] to the same HICO scene and derived K_d and $a_g(320)$ as calculated using equation (2). To obtain the entire CDOM spectra, a_g at other wavelengths was estimated according to $a_g(\lambda) = a_g(320) \times \exp\big(-0.0175 \times (\lambda - 320)\big)$, where 0.0175 is *S* calculated from CDOM samples collected in the study area [*Cao and Miller*, 2014]. The CO AQY spectrum in equation (4) was used for both P_{CO} calculations and the differences between models was calculated with equation (5) as follows:

$$\text{Difference} = (P_{CO}^{BL} - P_{CO}^{FM})/[(P_{CO}^{BL} + P_{CO}^{FM})/2] \qquad (5)$$

4. Results

4.1. Depth-specific distribution of CO photoproduction

The spatial distribution of depth-specific CO photoproduction rates (Ψ_{CO}, nmol (CO) m^{-3} h^{-1}) varies partially as a function of different depths considered. The rates calculated at the sea surface ($z = 0^{-}$) demonstrate remarkable spatial variation, ranging from 50 nmol m^{-3} h^{-1} in the intracoastal waterway to 0.2 nmol m^{-3} h^{-1} offshore, with a mean of 9.2 nmol m^{-3} h^{-1} (Figure 4.3 (a)). These values are comparable with coastal waters reported elsewhere in the Gulf of Maine [*Ziolkowski and Miller*, 2007], the Canada Basin [*Song et al.*, 2013]. Ψ_{CO} at z = 1 m is generally one to two orders of magnitude lower than that just at the surface, ranging from 1×10^{-4} to 3.8 nmol m^{-3} h^{-1}, with a mean of 1.2 nmol m^{-3} h^{-1} (Figure 4.3 (b)). Comparison of the spatial Ψ at these two different depths shows a striking difference behind barrier islands where the lowest rates were observed at z = 1 m while Ψ remains highest just below the surface. This is understandable given the high abundances of optically active constituents in estuaries including CDOM (Figure 4.2 (c)) and particles, both contributing to the high K_{d} observations (Figure 4.2 (b)). Rapid attenuation of UV irradiation results in little light energy for photochemistry at z = 1 m, creating low photoproduction rates within estuaries at the 1 m isobaths. Ψ_{CO} at z = 1 m is higher in coastal areas due to reduced UV attenuation, at least partly from lower CDOM values. This gradual reduction in CDOM seaward, on the other hand, results in Ψ at 1 m decreasing overall towards the inner shelf.

4.2. Depth-integrated CO photoproduction

The spatial detail of depth-integrated photochemistry obtained with our model obtained with our approach (P_{CO}^{BL}) ranges over an order of magnitude with the scene, varying from 0.13 to 12 nmol m^{-2} h^{-1}, with a mean of 4.3 nmol m^{-2} h^{-1} (Figure 4.4). A seemingly surprising result is that the lowest P_{CO}^{BL} values occur in the most inshore estuarine waters, exactly where CDOM and surface rates ($\Psi_{\mathrm{CO}}(z = 0^{-})$) are the highest. In other words, the most photochemically productive waters, in terms of P_{CO}, are decoupled from their source material (CDOM) in these estuaries.

Seaward transects for P_{CO}^{BL} shows decreasing values and is similar to Ψ_{CO} in the surface and at one meter depth.

Distributions of depth-integrated rates using the FM approach (P_{CO}^{FM}, Figure 4.5 (a)), however, bear little resemblance to P_{CO}^{BL} (Figure 4.4). Compared to P_{CO}^{BL}, P_{CO}^{FM} exhibits far less spatial variability and the difference between P_{CO}^{FM} and P_{CO}^{BL} can be quite striking, especially for inshore waters and downstream of the Altamaha River outflow which differ by as much as as ±100% (Figure 4.5 (b)). A detailed discussion on these discrepancies is provided in section 5.2.

5. Discussion

Based on the optical and photochemical parameters, approaches, and assumptions involved in producing the results above, the following discussion explores three issues: (1) uncertainties in estimating photoproduction from ocean color; (2) potential causes of differences between the depth-integrated CO photoproduction results in this study (i.e., P_{CO}^{BL}) and values calculated using the FM approach (i.e., P_{CO}^{FM}); and (3) implications for UV-dependent processes in the ocean derived from using two, independent ocean color algorithms to retrieve decoupled K_d and a_g.

5.1. Uncertainties in CO photoproduction estimation from ocean color

The derivation of UV optical parameters and the characterization of spectral photochemical efficiency both introduced uncertainties into our ultimate calculation of P or Ψ. For example, even assuming R_{rs} is accurate, the best UV optical models introduce uncertainties of 15% and 25% when deriving $K_d(340)$ and $a_g(340)$ using the composite Sea*UV* and Sea*CDOM* algorithms, respectively.

A second source of uncertainty stems from the variability of laboratory derived photochemical quantum yield spectra. Numerous studies have shown that AQY for several photoproducts critically depends on CDOM characteristics [*Stubbins et al.*, 2011] and therefore AQY spatial distribution can vary appreciably [e.g., *Bélanger et al.*, 2008; *Bélanger et al.*, 2006; *Johannessen and Miller*, 2001]. CO AQY spectra, however, remain relatively constant in oligotrophic open ocean waters [*Zafiriou et al.*, 2003] and so reasonably allow the usage of one average AQY_{CO} spectrum in global studies such as *Fichot and Miller* [2010]. Estuarine and coastal areas, on the other hand, are subjected to variable terrestrial influence and AQY variations can span several orders of magnitude [*Powers and Miller*, 2015] due to increased complexity of CDOM sources and photochemical mechanisms by which CDOM produces CO [*H Gao and Zepp*, 1998]. This natural variability of CDOM complicates efforts to constrain photochemical rates in coastal waters.

This difficulty is partly overcome in our coastal study area in two ways. First, the area within our HICO image is relatively small and represents only a small subset of possible CDOM sources that create variability in AQY. Second, AQY spectra for this area have been determined with a field sampling program covering 3 years of seasonal study, allowing us to capture the AQY variability and define a single AQY_{CO} spectra that is representative of our specific study area. We caution, therefore, that, photochemical modeling results from this study cannot simply be generalized to other estuaries or the entire coastal ocean with the same confidence. Although significant improvements in the accuracy of retrieving K_d and a_g in a wide variety of coastal waters have been achieved ([*Cao and Miller*, 2014; *Cao et al.*, 2014]), they may be largely overshadowed by the great uncertainties resulting from varied AQY spectra over larger and more diverse geographic areas. In light of this, to apply the approach proposed in this study elsewhere, rigorous modeling and precise knowledge of regional AQY spectra is essential for improved estimates of photoproduction rates from satellite data.

In addition, ocean color algorithms in coastal waters that rely on satellite platforms are often subjected to errors resulting from the imperfect atmospheric correction of blue wavebands, in particular the 412 nm waveband. It is worth noting that both the composite Sea*UV* and Sea*CDOM* algorithms were developed from optical buoy data that included $R_{rs}(412)$ and the inclusion of uncertainties due to atmospheric correction can lead to biased optical property estimates when applied to satellite data. Unfortunately, there is no robust ground-truth data included in this study, preventing direct determination of the exact uncertainty associated with this recognized issue. Nevertheless, this potential source of error cannot be neglected and future ocean color algorithms for coastal waters may benefit from approaches that do not require $R_{rs}(412)$ for their implementation.

5.2. Interpretation of depth-integrated CO photoproduction

The large differences between P_{CO} in this study (P_{CO}^{BL}) and results obtained using the FM approach (P_{CO}^{FM}), can be explained by differences in modeling procedures. Factors driving P_{CO} are threefold: (1) the incident downwelling irradiance below the sea surface ($E_d(\lambda, 0^-)$); (2) the spectral fraction of that irradiation absorbed by CDOM; and (3) the photochemical efficiency of CO production from CDOM, namely $\phi_{CO}(\lambda)$ [*Bélanger et al.*, 2006]. Because in applying both models, we used the same $\phi_{CO}(\lambda)$ and irradiance data, the spectral contribution of CDOM absorbance to total light attenuation, $a_g(\lambda)/K_d(\lambda)$, or the ratio of $a_g(\lambda)/a_{total}(\lambda)$ as in *Bélanger et al.* [2006], becomes the largest driver behind P_{CO} variations. It is known that the value of $a_g(\lambda)/K_d(\lambda)$ not only varies with wavelength [*Johannessen et al.*, 2003] but depends on water optical properties [*Tedetti et al.*, 2007; *Zepp et al.*, 2008]. Lacking options, the FM approach uses a field-derived constant of 0.68 for $a_g(320)/K_d(320)$ and thus cannot accommodate its known spatial heterogeneity in complex systems. This faulty assumption leads to the homogeneous distribution of P_{CO}^{FM} seen in Figure 4.5(a), and fails to capture the true P_{CO} in the coastal environment where various optically active materials occur independently. Comparatively, decoupled retrievals of K_d and a_g from two separate algorithms that are applied independently to each pixel, can account for this variance and seem to recover more reasonable spatial details for these optically complex waters.

To help with the interpretation, we examined the spatial distribution of the fraction of UV radiation absorbed by CDOM relative to total attenuation at λ = 340 nm (i.e., $a_\mathrm{g}(340)/K_\mathrm{d}(340)$) estimated from the HICO image. As shown in Figure 4.6, $a_\mathrm{g}(340)/K_\mathrm{d}(340)$ varied markedly, with inshore waters generally having lower $a_\mathrm{g}(340)/K_\mathrm{d}(340)$ values than coastal and offshore waters, suggesting a dynamic partitioning of light into different optically active components. Waters from the Altamaha River have very heavy particle loadings which absorb and scatter light and show the lowest $a_\mathrm{g}(340)/K_\mathrm{d}(340)$ (~ 0.1–0.2) in the study area. The attenuation of irradiance by particles diminishes during estuarine mixing processes as particles are removed from the water column due to flocculation, resulting in higher values (~0.9) of $a_\mathrm{g}(340)/K_\mathrm{d}(340)$ in nearshore coastal areas where CDOM remains high. Further offshore, the ratio becomes slightly lower, perhaps representing the dilution of CDOM away from shore. This dynamic range of $a_\mathrm{g}(340)/K_\mathrm{d}(340)$ observed from ocean color agrees reasonably well with prior field observations within the study area ranging from 0.33 to 1. While direct field verification is warranted, these results confirm the potential of this blended approach to quantify the contribution of CDOM absorbance to the total attenuation of photons in surface waters using remote sensing.

Our modeling results provide insight into the underlying optical principle that governs observed spatial distributions of the depth-integrated photoproduction rate P. The close coupling of patterns in $a_\mathrm{g}/K_\mathrm{d}$ (Figure 4.6) with P_{CO}^{BL} (Figure 4.4) is clearly seen, with lower P associated with lower a_g/K_d values that very likely track particle concentrations within estuarine waters and increased P in coastal waters where elevated a_g/K_d is observed. Similar correlations have been observed in other optically complex waters [*Bélanger et al.*, 2008; *Xie et al.*, 2012]. Unlike modeling depth-specific photoproduction rates that requires explicit knowledge of both K_d and a_g, estimation of CDOM-driven photochemical processes integrated over the entire water column is primarily a function of the proportion of the spectral radiation absorbed by CDOM to the total loss of photons to other mechanisms, namely a_g/K_d. Whereas this partitioning of photons has been noted previously in the visible regime [*Bélanger et al.*, 2008; *Bélanger et al.*, 2006], to the best of our knowledge, our study provides the first synoptic estimate of this optical phenomenon in the UV. Revealing these spatial patterns from satellite-derived ocean color underscores the value of our new ability to blend two disparate ocean color algorithms to probe UV processes in the marine environment.

5.3. Implications of decoupled retrievals of optical properties

In addition to the substantial benefits inherent in the independent retrievals of two optical parameters by different ocean color algorithms in estimating CDOM photochemistry, novel insights should be obtainable for estimating photochemistry occurring in the particulate phase. Recent studies have noted a significant photoreactivity involving suspended particles [*Xie and Zafiriou*, 2009 and references therein]. Notably, *Song et al.* [2013] demonstrate that particulate organic matter, regardless of its origins, could be more susceptible to photo alteration than CDOM in terms of CO photoproduction. More generally, *Estapa and Mayer* [2010] conclude that quantitative knowledge of light absorption partitioning into different photochemically active materials is indispensible to clarify the photoredox mechanisms of particulate organic matter. Hence, spectral partitioning of the CDOM absorption in the UV relative to the total attenuated photon budget, as described in this study, could help describe variability in the UV light allocation among materials in different phases (dissolved vs. particulate) and further aid in disentangling metal redox (e.g., iron) effects on the photochemistry of particulate organic matter in the ocean.

Implications for the capability to quantify the relative contribution of CDOM to UV attenuation using remote sensing could go well beyond photochemistry. Since CDOM serves as a “sunscreen” from destructive UV radiation for marine biota, spectral knowledge of CDOM absorption relative to photon interaction with particles is desirable to evaluate biological effects on marine ecosystems including direct DNA damage [*Zepp et al.*, 2008] and coral reef health [*Barnes et al.*, 2014] on a spatially synoptic scale from ocean color. Additionally, it is widely acknowledged that different biological responses to UV radiation vary with wavelength [*Neale*, 2000]. Hence, knowledge of the spectrally resolved UV light flux partitioned to CDOM may allow remote sensing data to inform biological weighting functions and further describe the spectrally dependent biologically effective radiance in the water column [*Cullen et al.*, 1992; *Williamson et al.*, 2001].

6. Concluding remarks and Outlook

This work has shown the potential of blending two different ocean color algorithms to address UV dependent processes in a coastal environment from high resolution satellite observations. Two main contributions are (1) the successful demonstration of both depth–specific and depth–integrated photochemical production of CO on a small estuarine scale, and (2) the use of decoupled retrievals of K_d and a_g for the appraisal of optical dynamics that estimate the percentage of light attenuated by CDOM at high spatial resolution through the UV wavelengths using remote sensing. This later contribution appears to overcome a persistent challenge in remote sensing applications predicting marine photochemistry and could provide opportunities to quantify diverse UV-dependent processes in the ocean. With good estimates of CDOM absorbance contribution to total UV attenuation, important biogeochemical issues like the impact of photochemical reactions on carbon cycling, redox chemistry, and marine ecosystem responses to UV radiation can be more accurately addressed.

While this “snapshot” assessment of UV–driven photochemistry from HICO ocean color appears to have succeeded, it should be noted again that the AQY for CO (or for any other photoproduct) in coastal and inshore systems is most likely regional and exerts a predominant control on photochemical calculations. Upscaling CO production values obtained in this study to other coastal waters is not recommended without fully understanding that AQY is variable and must be constrained for the location under study. A particular challenge is to quantify the natural variability of AQY for high resolution applications since it is known to be dynamic and remains highly field/laboratory measurement dependent. Consequently, our study is somewhat more tentative with regards to absolute values of CO photochemical production than it is as a demonstration of the use of remote sensing to address biogeochemical issues at a fine scale in optically dynamic inshore systems. Accurate seasonal and yearly quantification of photochemical fluxes on a coastal scale requires long term, systematic ocean color climatology as well as rigorous modeling of regional AQY for any photoproduct in question. Photochemical fluxes dependent on UV CDOM photolysis can easily be pursued for photoproducts other than CO. For instance, the photoproduction of hydrogen peroxide has been mapped on a global scale using remote sensing [*Powers and Miller,* 2014] and may potentially serve as a proxy to allow estimates of the photoproduction of carbon dioxide [Powers, 2014], which is of great interest from a climate change and carbon cycling perspective. In this respect, future work may benefit from our two algorithm blended approach to better understand the contribution of photochemistry to total carbon inventories.

On the other hand, with regard to remotely sensed optical variables (i.e., K_d and a_g), uncertainties stemming from the inclusion of R_{rs} in the blue wavelengths, namely $R_{rs}(412)$, in satellite ocean color algorithms are clearly recognized. Further refinements of *Cao et al.* [2014] and *Cao and Miller* [2014], algorithms for K_d and a_g respectively, may reduce errors by omitting $R_{rs}(412)$, thereby improving optical retrievals from ocean color in a synoptic view, particularly for coastal waters. In addition, evaluation of UV light partitioning into different optically active constituents at present, can only be made for the dissolved phase. Nevertheless, this determination is informative. Within the context of current satellite mission planning, such as the PACE (Pre-Aerosol, Clouds, and ocean Ecosystems) that includes UV measurements of ocean color, one potential application of our approach would be to explore UV-affected ocean ecology and carbon chemistry by assessing relative contributions of photo-sensitive materials affecting the ocean color observations.

Acknowledgements

We are grateful to B-C Gao in the Naval Research Laboratory for helping with the atmospheric correction on the HICO data. We thank D. Mishra and J. Schalles for helpful comments on this manuscript.

References

Barnes, B. B., C. Hu, J. P. Cannizzaro, S. E. Craig, P. Hallock, D. L. Jones, J. C. Lehrter, N. Melo, B. A. Schaeffer, and R. Zepp (2014), Estimation of diffuse attenuation of ultraviolet light in optically shallow Florida Keys waters from MODIS measurements, *Remote Sensing of Environment*, *140*, 519-532.

Bauer, J. E., W.-J. Cai, P. A. Raymond, T. S. Bianchi, C. S. Hopkinson, and P. A. Regnier (2013), The changing carbon cycle of the coastal ocean, *Nature*, *504*(7478), 61-70.

Bélanger, S., M. Babin, and P. Larouche (2008), An empirical ocean color algorithm for estimating the contribution of chromophoric dissolved organic matter to total light absorption in optically complex waters, *Journal of Geophysical Research: Oceans (1978–2012)*, *113*(C4).

Bélanger, S., H. Xie, N. Krotkov, P. Larouche, W. F. Vincent, and M. Babin (2006), Photomineralization of terrigenous dissolved organic matter in Arctic coastal waters from 1979 to 2003: Interannual variability and implications of climate change, *Global Biogeochemical Cycles*, *20*(4).

Blough, N. V., and R. Del Vecchio (2002), Chromophoric DOM in the coastal environment, *Biogeochemistry of marine dissolved organic matter*, 509-546.

Cao, F., and W. L. Miller (2014), A new algorithm to retrieve chromophoric dissolved organic matter (CDOM) absorption spectra in the UV from ocean color, *Journal of Geophysical Research: Oceans*.

Cao, F., C. G. Fichot, S. B. Hooker, and W. L. Miller (2014), Improved algorithms for accurate retrieval of UV/visible diffuse attenuation coefficients in optically complex, inshore waters, *Remote Sensing of Environment*, *144*, 11-27.

Cauwet, G. (2002), DOM in the coastal zone, *Biogeochemistry of marine organic matter*, 570-611.

Cullen, J. J., P. J. Neale, and M. P. Lesser (1992), Biological weighting function for the inhibition of phytoplankton photosynthesis by ultraviolet radiation, *Science*, *258*(5082), 646-650.

Domingues, R. B., C. C. Guerra, A. B. Barbosa, V. Brotas, and H. M. Galvão (2014), Effects of ultraviolet radiation and CO2 increase on winter phytoplankton assemblages in a temperate coastal lagoon, *Journal of Plankton Research*, fbt135.

Estapa, M. L., and L. M. Mayer (2010), Photooxidation of particulate organic matter, carbon/oxygen stoichiometry, and related photoreactions, *Marine chemistry*, *122*(1), 138-147.

Fichot, C. G., and W. L. Miller (2010), An approach to quantify depth-resolved marine photochemical fluxes using remote sensing: Application to carbon monoxide (CO) photoproduction, *Remote Sensing of Environment*, *114*(7), 1363-1377.

Fichot, C. G., S. Sathyendranath, and W. L. Miller (2008), Sea< i> UV</i> and Sea< i> UV</i>< sub> C</sub>: Algorithms for the retrieval of UV/Visible diffuse attenuation coefficients from ocean color, *Remote Sensing of Environment*, *112*(4), 1584-1602.

Gao, B.-C., and C. O. Davis (1997), Development of a line-by-line-based atmosphere removal algorithm for airborne and spaceborne imaging spectrometers, paper presented at Optical Science, Engineering and Instrumentation'97, International Society for Optics and Photonics.

Gao, H., and R. G. Zepp (1998), Factors influencing photoreactions of dissolved organic matter in a coastal river of the southeastern United States, *Environmental Science & Technology*, *32*(19), 2940-2946.

Garcia, R. A., P. R. C. S. Fearns, and L. I. W. McKinna (2014), Detecting trend and seasonal changes in bathymetry derived from HICO imagery: A case study of Shark Bay, Western Australia, *Remote Sensing of Environment*, *147*, 186-205.
Johannessen, S. C., and W. L. Miller (2001), Quantum yield for the photochemical production of dissolved inorganic carbon in seawater, *Marine chemistry*, *76*(4), 271-283.

Johannessen, S. C., W. L. Miller, and J. J. Cullen (2003), Calculation of UV attenuation and colored dissolved organic matter absorption spectra from measurements of ocean color, *Journal of Geophysical Research: Oceans (1978–2012)*, *108*(C9).

Lucke, R. L., M. Corson, N. R. McGlothlin, S. D. Butcher, D. L. Wood, D. R. Korwan, R. R. Li, W. A. Snyder, C. O. Davis, and D. T. Chen (2011), Hyperspectral Imager for the Coastal Ocean: instrument description and first images, *Applied Optics*, *50*(11), 1501-1516.

Mishra, D. R., B. A. Schaeffer, and D. Keith (2014), Performance evaluation of normalized difference chlorophyll index in northern Gulf of Mexico estuaries using the Hyperspectral Imager for the Coastal Ocean, *GIScience & Remote Sensing*, *51*(2), 175-198.

Mopper, K., and D. J. Kieber (2002), *Photochemistry and the cycling of carbon, sulfur, nitrogen and phosphorus*, Academic Press: New York.

Neale, P. J. (2000), Spectral weighting functions for quantifying effects of UV radiation in marine ecosystems, *The effects of UV radiation in the marine environment*, 72-100.

Neale, P. J., J. J. Cullen, and R. F. Davis (1998), Inhibition of marine photosynthesis by ultraviolet radiation: Variable sensitivity of phytoplankton in the Weddell-Scotia Confluence during the austral spring, *Limnology and oceanography*, *43*(3), 433-448.

Powers, L. C., and W. L. Miller (2014), Blending remote sensing data products to estimate photochemical production of hydrogen peroxide and superoxide in the surface ocean, *Environmental Science: Processes & Impacts*, *16*(4), 792-806.

Powers, L.C. 2014. Probing the photochemical reactivity of oceanic dissolved organic carbon. Ph.D. thesis. Univ. of Georgia.

Powers, L. C., & Miller, W. L. (2015). Photochemical production of CO and CO 2 in the Northern Gulf of Mexico: Estimates and challenges for quantifying the impact of photochemistry on carbon cycles. *Marine Chemistry*, *171*, 21-35.

Prieur, L., and S. Sathyendranath (1981), An optical classification of coastal and oceanic waters based on the specific spectral absorption curves of phytoplankton pigments, dissolved organic matter, and other particulate materials, *Limnology and oceanography*, *26*(4), 671-689.

Reader, H. E., and W. L. Miller (2012), Variability of carbon monoxide and carbon dioxide apparent quantum yield spectra in three coastal estuaries of the South Atlantic Bight, *Biogeosciences*, *9*(11), 4279-4294.

Ryan, J. P., C. O. Davis, N. B. Tufillaro, R. M. Kudela, and B. C. Gao (2014), Application of the Hyperspectral Imager for the Coastal Ocean to phytoplankton ecology studies in Monterey Bay, CA, USA, *Remote Sensing*, *6*(2), 1007-1025.

Song, G., H. Xie, S. Bélanger, E. Leymarie, and M. Babin (2013), Spectrally resolved efficiencies of carbon monoxide (CO) photoproduction in the western Canadian Arctic: particles versus solutes, *Biogeosciences*, *10*(6), 3731-3748.

Stubbins, A., C. S. Law, G. Uher, and R. C. Upstill-Goddard (2011), Carbon monoxide apparent quantum yields and photoproduction in the Tyne estuary, *Biogeosciences*, *8*(3), 703-713.

Stubbins, A., G. Uher, C. S. Law, K. Mopper, C. Robinson, and R. C. Upstill-Goddard (2006), Open-ocean carbon monoxide photoproduction, *Deep Sea Research Part II: Topical Studies in Oceanography*, *53*(14), 1695-1705.

Tedetti, M., R. Sempéré, A. Vasilkov, B. Charriere, D. Nérini, W. L. Miller, K. Kawamura, and P. Raimbault (2007), High penetration of ultraviolet radiation in the south east Pacific waters, *Geophysical research letters*, *34*(12).

Williamson, C. E., P. J. Neale, G. Grad, H. J. De Lange, and B. R. Hargreaves (2001), Beneficial and detrimental effects of UV on aquatic organisms: implications of spectral variation, *Ecological Applications*, *11*(6), 1843-1857.

Xie, H., and O. C. Zafiriou (2009), Evidence for significant photochemical production of carbon monoxide by particles in coastal and oligotrophic marine waters, *Geophysical research letters*, *36*(23).

Xie, H., S. Bélanger, G. Song, R. Benner, A. Taalba, M. Blais, J.-É. Tremblay, and M. Babin (2012), Photoproduction of ammonium in the southeastern Beaufort Sea and its biogeochemical implications, *Biogeosciences*, *9*(8), 3047-3061.

Zafiriou, O. C., S. S. Andrews, and W. Wang (2003), Concordant estimates of oceanic carbon monoxide source and sink processes in the Pacific yield a balanced global “blue- water” CO budget, *Global Biogeochemical Cycles*, *17*(1).

Zepp, R. G., G. C. Shank, E. Stabenau, K. W. Patterson, M. Cyterski, W. Fisher, E. Bar-Tels, and S. L. Anderson (2008), Spatial and temporal variability of solar ultraviolet exposure of coral assemblages in the Florida Keys: Importance of colored dissolved organic matter, *Limnology and oceanography*, *53*(5), 1909.

Ziolkowski, L. A., and W. L. Miller (2007), Variability of the apparent quantum efficiency of CO photoproduction in the Gulf of Maine and Northwest Atlantic, *Marine chemistry*, *105*(3), 258-270.

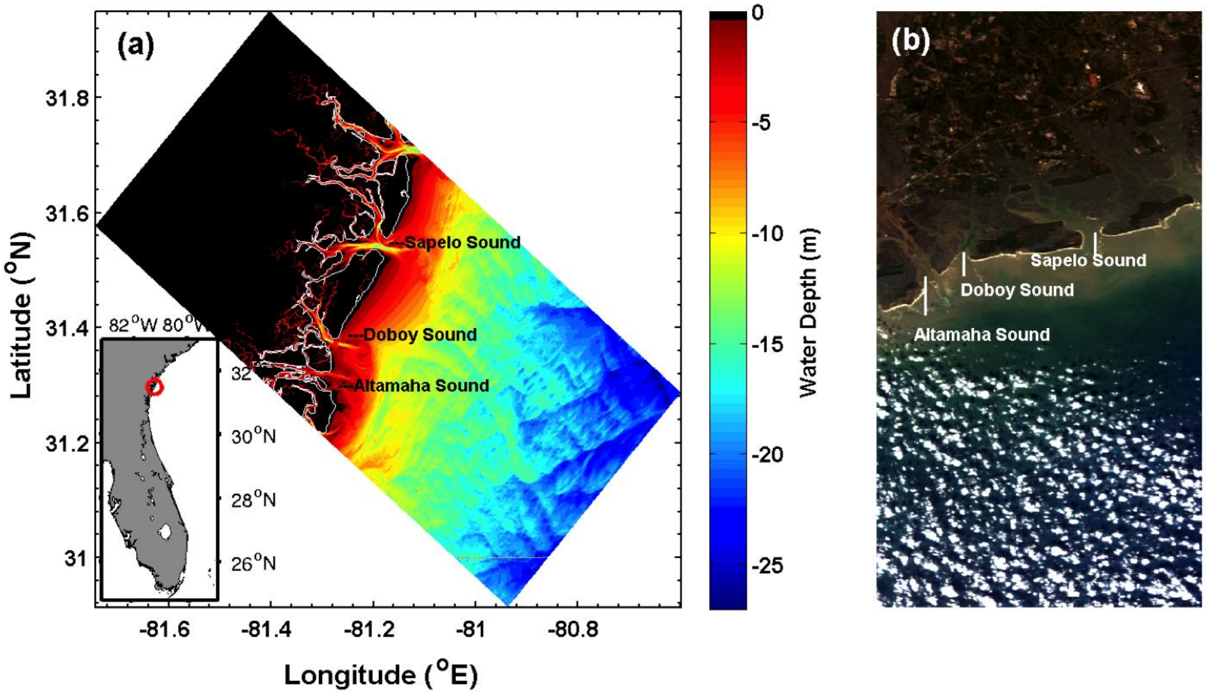

Figure 4.1: (a) Map of coastal Georgia with coastline (white) marked; (b) true color HICO image over coastal Georgia on January 18th, 2013.

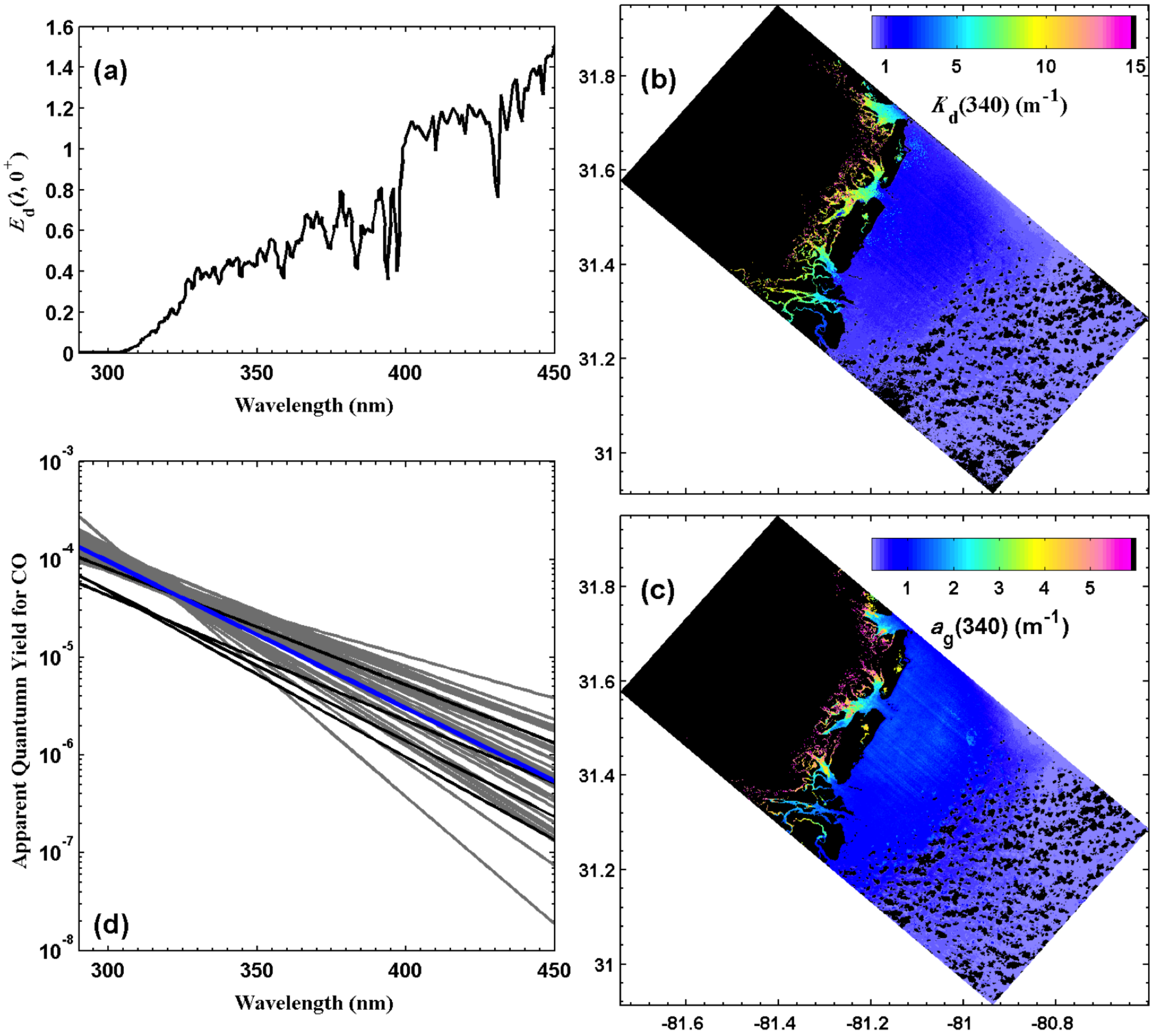

Figure 4.2: Input parameters for the calculation of depth-specific CO photoproduction rate with (a) $E_d(0^+, \lambda)$, with simulation condition as: latitude = 32.31°N, longitude = 81.76 °W, clear sky with ozone concentration of 340 DU on January 18th, 2013; (b) $K_d(340)$ derived from the composite Sea*UV* algorithms; (c) $a_g(340)$ derived from the Sea*CDOM* algorithms; and (d) Apparent quantum yield spectra of CO, with grey background lines denote data published in Reader and Miller (2012) (*N* = 37), black lines represent our data set sampled in year of 2013 (*N* = 4), and blue line stands for the spectra used for modeling in this study by taking average of the total 41 measurements.

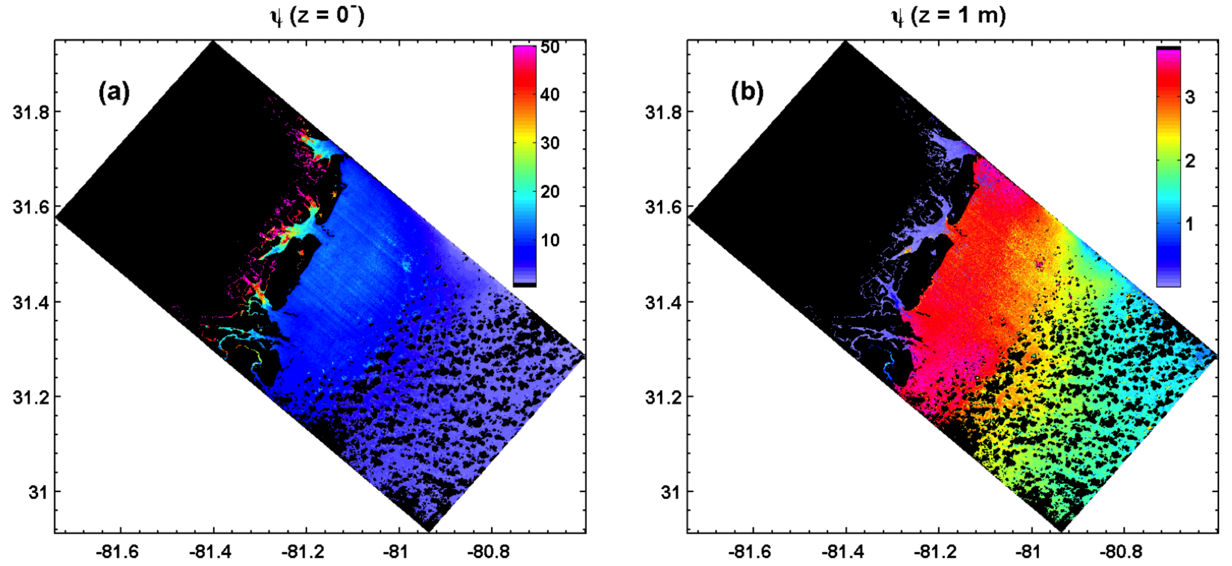

Figure 4.3: Model output of depth-specific CO photoproduction rate ($\Psi_{\mathrm{CO}}(z)$, nmol (CO) $\mathrm{m}^{-3}\,\mathrm{h}^{-1}$) at (a) $z = 0^{-}$ m; and (b) $z = 1$ m isodepths.

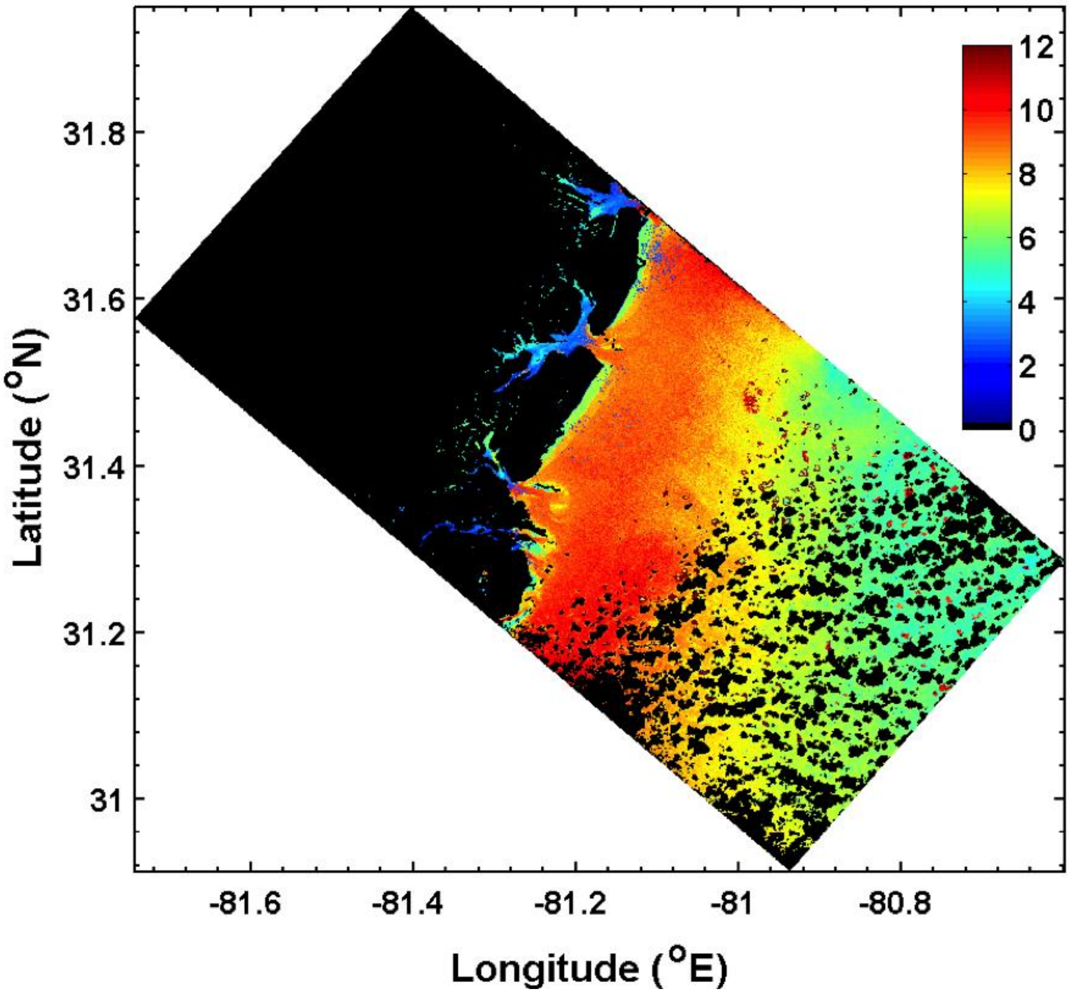

Figure 4.4: Model output of depth-integrated CO photoproduction rate (P_{CO}^{BL}, nmol (CO) m^{-2} h^{-1}).

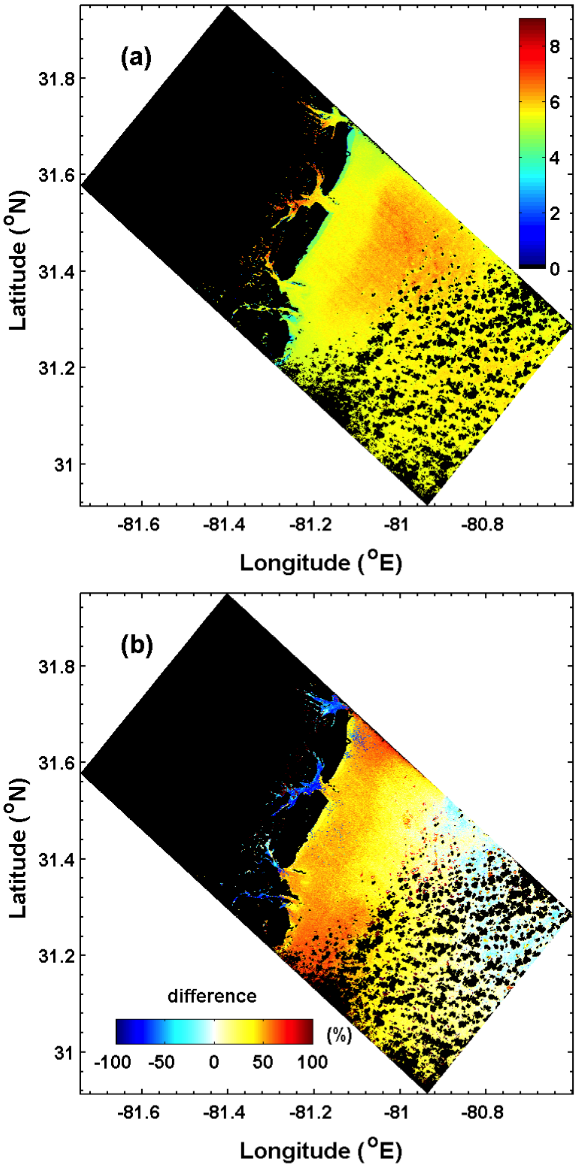

Figure 4.5: (a) Modeled depth-integrated CO photoproduction rate using the approach in Fichot and Miller (2010) (P_{CO}^{FM}); and (b) difference between P_{CO}^{BL} and P_{CO}^{FM}.

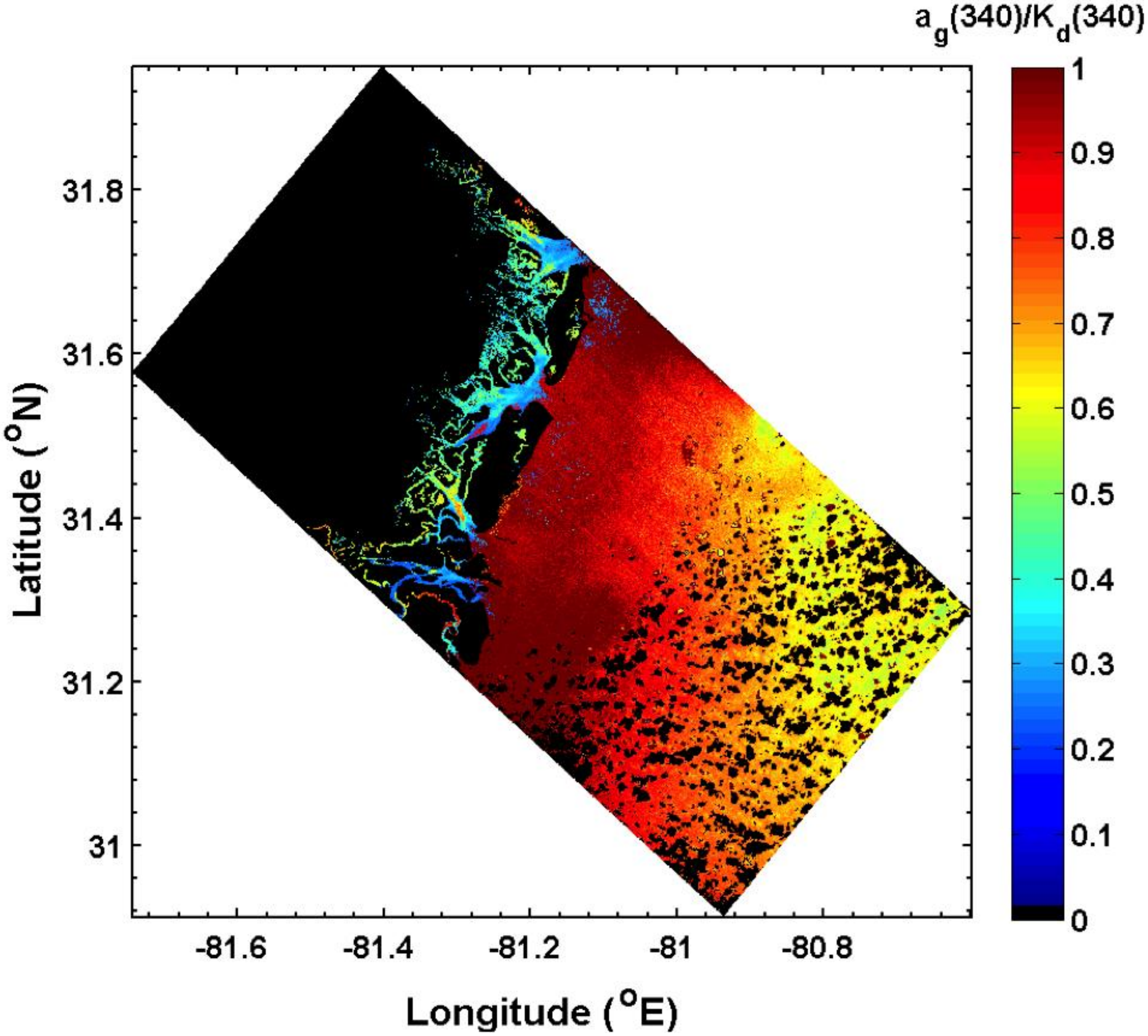

Figure 4.6: Distribution of spectral contribution of CDOM to total light attenuation at 340 nm ($a_g(340)/K_d(340)$).

CHAPTER 5

DISTRIBUTION OF CHROMOPHORIC AND FLUORESCENT DISSOLVED ORGANIC MATTER COMPONENTS IN THE NORTHEASTERN NORTH PACIFIC OCEAN[5]

---

[5] Cao, F., and W. L. Miller. To be submitted to *Deep Sea Research*.

Abstract

This study surveys optical properties of dissolved organic carbon (DOC) in the Gulf of Alaska (GoA) in the Northeastern North Pacific Ocean which contains the oldest carbon in the ocean. High resolution vertical distributions of chromophoric dissolved organic matter (CDOM) and fluorescent DOM (FDOM) were measured using ultraviolet/visible (UV/Vis) absorbance spectra and excitation-emission matrix spectra (EEMs) coupled with parallel factor analysis (PARAFAC). Four humic-like and two protein-like fluorescent components were identified in the GoA and processes responsible for the observed profiles were examined. Humic-like components demonstrated lower abundance in the surface, mainly resulting from photobleaching, and increased in the subsurface and remained constant in the deep. In contrast, protein-like components had higher levels in the surface due to biological production and decrease with depth, implying the consumption of these protein-like substances. Findings suggest vertical profiles of CDOM and protein-like components in the dark ocean (below 200 m) is largely controlled by microbial remineralization while physical mixing in this slowly upwelled water cannot be neglected. In an attempt to trace bulk DOC, especially the refractory DOC in the deep, we further adopt protein-like components as a proxy to formulate a multiple linear regression between observed DOC and two protein-like components. Results show that protein-like fluorescent components are quite promising to trace refractory DOC in the deep ocean.

1. Introduction

Marine dissolved organic carbon (DOC) constitutes one of the most abundant active carbon reservoirs, holding 662±32 Pg C in a global inventory. As a substrate source for heterotrophic bacteria and a sink for autotrophically fixed carbon, DOC plays a significant role in the global ocean carbon cycle (Hansell, 2002; Hansell *et al.*, 2009). It is largely produced in the euphotic zone, exported into ocean interior via mixing into the main thermocline, and eventually transported to the deep North Pacific Ocean via the “global ocean conveyor belt”. As a consequence, the deep waters in the Northeastern North Pacific Ocean contains the most aged deep water, isolating the ocean’s most biologically refractory DOC, a pool that is of paramount importance in terms of long term carbon sequestration over centennial to millennial time scales due to its slow turnover rate. Interestingly, this area of deep water remains under-investigated.

A portion (20-70%) in the bulk DOC pool is optically active, referred to as chromophoric dissolved organic matter (CDOM) (Blough and Del Vecchio, 2002), and plays a critical role in regulating photo-relevant processes via absorption of light and influences the biogeochemistry of DOC. *In situ* production through bacterial transformation of organic matter is thought to be the primary source of CDOM in the open ocean where terrestrial influence is minor (Nelson *et al.*, 2004). CDOM is removed via photochemical degradation when exposed to light (Del Vecchio and Blough, 2002) and via microbial breakdown in the aphotic zone of the ocean (Nelson and Siegel, 2002). A fraction of CDOM fluoresces after absorbing light, and is referred to as fluorescent DOM (FDOM). FDOM is generally grouped into two types, the humic-like and protein-like components, based on the positions of their emission maxima in the excitation-emission matrix spectra (EEMs) (Coble, 1996). Humic-like FDOM is traditionally defined for fluorophores with emission peaks at longer wavelengths (> 400 nm) and protein-like FDOM is considered to be produced by biological processes with emission peaks at wavelengths shorter than 400 nm. By measuring seawater absorbance and fluorescence spectra, optical signatures of CDOM and FDOM can reveal information pertaining to DOM source materials as well as possible transformation processes. Therefore, to better explore the chemical nature of DOM in the Northeastern North Pacific Ocean, we have examined the optical characteristics of these two components of the DOM pool in the Gulf of Alaska (hereafter GoA).

In this work, we present spectrophotometric measurements coupled with parallel factor analysis (PARAFAC) and assess potential biogeochemical and physical processes driving distributions of these optical properties. Moreover, in examining this deep DOC pool, we develop a multi-linear relationship between DOC and protein-like fluorescent components to explore the potential for fluorescent information to trace bulk DOC in the ocean and provide information about the refractory fraction of DOM.

2. Materials and Methods

2.1. Field sampling and Water mass structure in the GoA

As part of the Deep Ocean Refractory Carbon (DORC) field campaign during August 4–21, 2013, high resolution surveys of DOM optical properties were performed onboard the R/V *Melville* in the GoA (Figure 5.1). Full-depth water samples were collected using a rosette equipped with 24 Niskin bottles and a conductivity-temperature-depth profiling sensor (Sea-Bird Electronics). All labware was either acid soaked (polycarbonate) or precombusted (glass, 450 °C), and rinsed thoroughly prior to sampling using Milli-Q water (>18 mΩ; Millipore) freshly produced daily onboard. Seawater samples were gravity filtered inline using a 0.2 μm Whatman Polycap AS 75 nylon cartridge linked directly from Niskin bottles with silicon tubing and analyzed for optical properties within four hours after sampling to avoid any possible storage artifacts (Spencer *et al.*, 2007).

Our study area encompassed four distinct water masses (Figure 5.2). A well mixed, relatively fresh (salinity (S) < 32) and warm (potential temperature (θ) >10 °C) layer extending through a summer mixed layer of ~50 m (Peterson *et al.*, 2005) comprises the North Pacific

Surface Water (NPSW). The NPSW is part of the subarctic gyre and is bound eastward by the northward flowing Alaskan Current. The Pacific Halocline Water (PHW) dominates a layer from roughly 50 to 150 m with a rapid salinity increase from 32 to 33.5 (Steele *et al.*, 2004). Beneath the PHW, the North Pacific Intermediate Water (NPIW) is delineated by water with a potential density anomaly (σ_θ) of 26.6-27.4 kg/m^3 (Hansell *et al.*, 2002), occupying the depth between 200–1000 m. The more saline (salinity > 34) Pacific Common Water (PCW), relative to the other three stratified water masses mentioned above, makes up a fairly uniform, well-mixed physical feature with elevated density (σ_θ of 27~28.1 kg/m^3).

2.3. Optical measurements and calculation of optical proxies

2.3.1. CDOM measurements and derivation of optical indexes

Samples were brought to room temperature before spectral measurements. CDOM absorption spectra were obtained using a single-beam 100 cm liquid waveguide capillary flow cell (World Precision Instruments Inc.), coupled with quartz fiber optics cables to a deuterium-tungsten light source (DT-mini GS; Ocean Optics) and a MAYA2000 PRO spectrophotometer. Milli-Q water was used as a blank reference, accounting for instrument drift. Baseline corrections for CDOM absorbance spectra were made by subtracting an offset value that corrects for scattering and refractive index differences between seawater and the blank. To obtain the offset value, raw absorbance spectra were fit over the wavelength range of 660-700 nm by applying a nonlinear fitting routine ("*nlinfit*" function in Matlab 2014) over the wavelength range of 660-700 nm to equation (1) (Reader and Miller, 2011) :

$$A = Fe^{-s\lambda} + O \qquad (1)$$

where A is the absorbance of CDOM, F is a fitting parameter, S is the spectral slope coefficient, and *O* is the desired offset value.

We calculated a corrected absorbance spectra by subtracting this offset value from the raw absorbance and the Napierian absorption coefficient spectrum was then created according to equation (2):

$$a_g(\lambda) = 2.303 \times A(\lambda)/L, \qquad (2)$$

where $a_{\mathrm{g}}(\lambda)$ (m^{-1}) is the Napierian absorption coefficient of CDOM at wavelength λ, $A(\lambda)$ (unitless) is the offset-corrected CDOM absorbance at λ, and L (m) is the path length.

2.3.2. Fluorescent measurement of DOM and PARAFAC analysis

Fluorescent excitation-emission matrix spectra (EEMs) were obtained for each sample with an Aqualog spectrofluorometer (HORIBA Jobin Yvon Inc., NJ) using a 1-cm quartz cell with Milli-Q as the blank. EEMs fluorescence intensities were measured by scanning across an excitation range of 240–450 nm (5 nm intervals) and capturing emission spectra over a wavelengths range of 280–500 nm (3.2 nm intervals). We optimized data quality by determining the optimal integration time for each sample that maximized emission intensity detection at low excitation wavelength without saturating CCD at high excitation wavelength (Gentry-Shields *et al.*, 2013). Inner filter corrections were not required due to extremely low CDOM absorbance (with $a_{\mathrm{g}}(320)$ at ~ 0.25 m^{-1} typically). Post-processing of EEMs to correct and calibrate the fluorescence spectra following Murphy *et al.* (2010) included three steps: (1) Manufacturer provided spectral correction parameters were applied to each EEM spectra, (2) Spectra were normalized to the daily determined Milli-Q Raman peak area at excitation wavelength 350 nm, and (3)Milli-Q Raman and Rayleigh scatter signals were removed using an interpolation method following protocol developed by Bahram *et al.* (2006). Fluorescence intensities (FI) are herein reported in Raman Units (R.U.).

The PARAFAC model was run for 597 full-depth profile samples using the DOMFluor toolbox in MATLAB (Stedmon and Bro, 2008). Due to the higher fluorescent intensities of surface waters relative to deep samples, EEMs were first scaled to unit intensity by normalizing to individual fluorescence intensity maxima (Murphy *et al.*, 2008) prior to the modeling process. PARAFAC was then applied to these scaled EEMs and the model was constructed and further validated using split-half analysis. Once the modeling process was complete, fluorescence intensities were multiplied by their maximum intensities to obtain real fluorescence intensities of each component in a given sample.

2.4. Auxiliary data

Apparent oxygen utilization (AOU) for each bottle sample was calculated with the difference between the calculated atmospheric equilibrium oxygen concentration following Garcia and Gordon (1992) and measured sample concentrations (Matlab seawater library , version 3.3.1, obtained via http://www.cmar.csiro.au/datacentre/ext_docs/seawater.htm).

3. Results and Discussion

3.1. Optical properties of DOM in the GoA

3.1.1. Spectral characteristics of fluorescent DOM

Six fluorescent components (C1 to C6 hereafter) were identified and validated by PARAFAC modeling (Figure 5.3). C1, C3, and C4 are similar to reported humic-like components having broad emission maxima at wavelengths >400 nm (Jørgensen *et al.*, 2011), typically indicative of a terrestrial humic-like or ubiquitous feature that has been widely observed in aquatic environments, including the open ocean waters (Jørgensen *et al.*, 2011; Kowalczuk *et al.*, 2013; Yamashita *et al.*, 2010). C2 is reported to be produced during organic matter breakdown by bacteria, and assigned as a marine humic-like component. Two protein-like components (C5 and C6) were identified in the GoA that demonstrate maxima at emission wavelengths shorter than 400 nm and are characteristic of autochthonous and bacterially produced amino acids. Consistent with other oceanic surveys, C5 and C6 are assigned as tyrosine (Ex./Em: 255 nm/300 nm) and tryptophan-like (Ex./Em: 280 nm/345 nm) components, respectively (Jørgensen *et al.*, 2011; Yamashita and Tanoue, 2003). In the text that follows, we refer to the humic-like (C1–C4) and protein-like (C5 and C6) components to as “$\mathrm{FDOM_H}$” and “$\mathrm{FDOM_P}$”, respectively.

3.1.2. Vertical profiles of CDOM and FDOM

Distribution of CDOM in the water column exhibits high spatial variability in the surface mixed layer (range 0.13 to 0.49 $\mathrm{m^{-1}}$ for $a_g(320)$), enrichment in the subsurface and upper mesopelagic layer (~ 150-500 m) and is slightly lower with limited variance at depth (mean $a_g(320)$ from 0.24 $\mathrm{m^{-1}}$ at 500 m to 0.18 $\mathrm{m^{-1}}$ at 4500 m) (Figure 5.4(a)). Variability in the surface water is attributable to the balance between CDOM addition (input processes and local production (Nelson *et al.*, 2004)) and removal (photolysis) in the GoA. Elevated $a_g(320)$ in the surface water associated with lower salinity (e.g., at station 15 with $a_g(320) = 0.49\ \mathrm{m^{-1}}$, salinity = 31.5) was occasionally observed in coastal areas and could reflect terrestrial materials discharged from glacial runoff and Alaskan rivers (Hood *et al.*, 2009; Neal *et al.*, 2010). Terrestrial inputs could partly explain the surface layer differences between the vertical variability of $a_g(320)$ at more coastal stations and the uniform CDOM profiles maintained at more remote stations that are considered to be less influenced by coastal runoff as in Yamashita and Tanoue (2009). A smooth $a_g(320)$ increase between ~150 and -500 m is also observed, presumably resulting from CDOM release accompanied with degradation of sinking biogenic particles (Nelson *et al.*, 2010; Swan *et al.*, 2009) and the absence of photodegradation. The slight decrease of CDOM with depth in the deep ocean may, at least in part, result from slower *in situ* CDOM production compared to that in shallower waters.

Vertical profiles of fluorescent components generally follow two distinct patterns (Figure 5.4(b) and (c)). Surface waters have low abundances of $FDOM_H$ (fluorescence intensity (FI) of 0.018, 0.008, 0.012, and 0.003 R. U. for C1, C2, C3, and C4, respectively) which gradually increases with depth exhibiting maximum values at ~ 1000 m for C1, C3, and C4 (FI of 0.033, 0.024, and 0.01 R. U. for C1, C3, and C4, respectively) and at ~ 250 m for C2 (with FI of ~ 0.017 R. U.). Below this depth, $FDOM_H$ remains fairly constant in the deep ocean. Similar to CDOM, the FI of $FDOM_H$ in the sea surface is a net result of production and loss mechanisms (Jørgensen *et al.*, 2011; Mopper and Schultz, 1993), while the increased $FDOM_H$ at depth and constant values in deep waters are attributable to *in situ* production. Profiles of $FDOM_P$, however, contrast markedly with those for $FDOM_H$, having elevated abundance in surface waters resulting from *in situ* biological activity, that decline with depth. This is similar to the profile for bulk DOC in the ocean and suggests a fraction of $FDOM_P$ is labile or semi-labile and could potentially be a proxy for bioavailable material (Mopper and Schultz, 1993). Our depth profiles for the two categories of FDOM are in good agreement with the Northwestern North Pacific data of Yamashita *et al.* (2010) and the extensive open ocean survey of Jørgensen *et al.* (2011) for waters other than the North Pacific. Taken together, the less variable $FDOM_P$ observed at depths in the global ocean may indicate its refractory nature, similar to the majority of DOC in the deep ocean, and therefore less likely to be altered by biogeochemical processes.

3.2. Processes influencing the distribution of DOM optical properties

3.2.1. Correlations between DOM optical properties, AOU, and DOC

To better understand potential oceanic processes that may regulate observed vertical profiles of CDOM and FDOM, we examined the correlations between AOU and DOM optical properties. We found that CDOM and $FDOM_H$ are generally positively correlated with AOU in the ocean interior (r = 0.46 for CDOM and r = 0.62 for C2 to AOU, respectively; e.g., depths>100 m, p=0.00, Figure 5.5(A) and (B)), suggesting that CDOM ($FDOM_H$) is formed *in situ* from microbial oxidation of organic matter. This agrees with previous observations from the Pacific Ocean (Kim and Kim, 2015; Swan *et al.*, 2009; Yamashita *et al.*, 2010; Yamashita and Tanoue, 2009). In addition, Jørgensen *et al.* (2014) found that production of $FDOM_H$ heavily depends on the lability of organic matter with more refractory substrates having larger $FDOM_H$ production relative to oxygen consumption. Considering that refractory carbon is thought to make up the majority of the deep DOM pool contained in our study area, it is not surprising to observe the correlations between $FDOM_H$ and AOU.

AOU and $FDOM_P$ show a weak negative correlation (r = –0.31, p<0.001, depth > 100 m, Figure 5.5(C)), suggesting a loss of $FDOM_P$ as organic matter is respired. In the remineralization zone (depth ~ 200–1000 m) where labile DOM is usually depleted, $FDOM_P$ may be an important substrate for bacteria (Stedmon and Markager, 2005) and can be consumed for bacterial respiration (Cammack *et al.*, 2004). For depths greater than 1000 m, this relationship was missing (r = –0.11, p>0.05), implying $FDOM_P$ cycling processes do not contribute to AOU, potentially due to bacterial anaerobic respiration (Barker, 1981).

3.2.2. Influence of physical processes

We have observed positive linear relations for AOU to both CDOM and $FDOM_H$ in the intermediate and deep layers in the GoA (r = 0.81 for AOU and CDOM, and r = 0.65 between 700 to 5000 m for example, p = 0.00), and can attribute this largely to biological processes that produce CDOM ($FDOM_H$) during organic matter remineralization. This reasoning, however, does not rule out the possibility of other processes (i.e., physical mixing from known sluggish vertical flow) may also contribute to this correlation. We therefore also must examine the potential physical processes such as convection that can contribute to DOM optical distributions. Our high resolution survey in the GoA deep waters allow a two end-member mixing analysis that uses salinity as a conservative tracer on waters from 700 m to the bottom. following the methods in Swan *et al.* (2009) and described below.

Each water sample collected from 700 m (upper end-member) to the deepest (lower end-member) has properties (e.g., AOU, $a_g(320)$, FI for each fluorescent component, etc.) that consist of a preformed conservative component (C_{con}) distributed solely by mixing, thereby independent of biogeochemical modifications. Considering a simple two component model, the fractional contributions of the upper (m_U) and lower (m_L) end-members to the observed property can be obtained as follows (Equation 3 (a) and (b)), if using salinity as the tracer:

$$m_U = (S_{obs} - S_L)/(S_U - S_L) \qquad (3(a))$$

$$m_U + m_L = 1 \qquad (3(b))$$

where S_{obs} stands for observed salinity for the given sample; and S_U and S_L represent salinity of the upper and lower end-members, respectively. Equation 3(b) holds for a mass balance constraint that the two fractional contributions must add up to 1.

Once m_U and m_L are obtained, the preformed component of the desired property due to mixing, using AOU as an example, can be calculated following Equation 4:

$$AOU_{mixing} = m_U \times AOU_U + m_L \times AOU_L \qquad (4)$$

where AOU_{mixing} is the sample AOU that would result solely from mixing. AOU_U and AOU_L are the AOU of the water at the upper and lower end-members, respectively.

Changes in the observed property due to processes other than mixing can then be obtained as in Equation 5,

$$\Delta AOU = AOU_{obs} - AOU_{mixing} \qquad (5)$$

where ΔAOU is the change resulting from non-mixing processes, and AOU_{obs} is the observed AOU of the sample.

We performed this two end-member mixing analysis on AOU, CDOM, and C2. Results show that the correlation noted above between AOU and CDOM is greatly weakened, but remains statistically significant after removing physical mixing (e.g., $r = 0.47$ for AOU and $a_g(320)$ compared to $r = 0.81$, p = 0.00). This implies that physical mixing has a substantial influence on the distribution of AOU and CDOM ($FDOM_H$) in the deep waters in the Northeastern North Pacific Ocean. Our conclusions are similar to those of Swan *et al.* (2009) where correlations between AOU and CDOM were also less strong once values were corrected for lateral isopycnal mixing across the Pacific Basin. This is understandable given that biological respiration is very slow below 1000 m and so contributes less CDOM to the deep water at the North Pacific Ocean than in other places, explaining the smaller variability of CDOM in deep waters.

3.3. Can $FDOM_P$ be a tracer for DOC in the ocean?

It has long been proposed that protein-like fluorescent components could potentially be a tracer for bio-reactive DOC since they are both enriched in the sea surface. In light of similar vertical profiles for DOC and $FDOM_P$ (Figure 5.4c) and the correlations between bulk DOC and $FDOM_P$ (0.71 and 0.76 for C5 and C6, respectively ($p<0.001$)), we attempted to build a simple multiple linear regression using measured bulk DOC and protein-like components C5 and C6 for the waters in the GoA with a resulting relationship (Equation (6)) of

$$ln[DOC] = 0.10932 \times ln[C5] + 0.25826 \times ln[C6] + 5.66238 \qquad (6)$$

Results from multi-linear regression (MLR) indicate that DOC overall can be described with moderate accuracy as a function of C5 and C6, with a slope of ~1.035, an intercept of ~ –1.311 (r = 0.83 (Figure 5.6)). Closer examination shows that for DOC concentrations < 45 µmol/kg which correspond to depths below 200 m (the bottom of halocline), DOC can be estimated more accurately, constrained to within +/– 10%, as a function of $FDOM_P$. This also suggests a strong co-variance of this refractory DOC with $FDOM_P$ which is presumably also largely resistant to bio-degradation given the oldest water that is depleted with labile organic matter, despite their smaller percent contribution to the refractory DOC compared to that of $FDOM_H$. Yamashita and Tanoue (2004) speculate that amino-acid containing materials in the high molecular mass DOM which dominates deep water (Medeiros *et al.*, 2015) result from refractory bacterial membranes and bio-polymers that are bio-resistant in nature, allowing preservation in the deep oceans. Another mechanism that may lead to the co-varying of refractory DOC and $FDOM_P$ could be ascribed to abiotic transformations of labile protein into recalcitrant DOM via complexation with existing DOM (Keil and Kirchman, 1994) during the long dark transport to the deep GoA.

Good estimations of bulk DOC from knowledge of $FDOM_P$ appear only to occur in the deep ocean. Errors are evident for waters above the NPIW and make our estimates less robust. This suggests decoupled processes between bulk DOC dynamics and $FDOM_P$ in waters within and above the halocline. Also, $FDOM_P$ content in the bulk DOC pool appears more variable, or at least different, from that in the deep ocean. $FDOM_p$ above the halocline is assumed to be largely authochthonous and more recently produced, as supported by the elevated abundance in the surface and upper halocline waters observed in this study and in Jørgensen *et al.* (2011). The authochthonous protein-like organic matter, though also usually of low molecular weight (Cuss and Guéguen, 2015), contributes to bulk DOC in a variable fashion in these shallower waters due to the dominance of labile and semi-labile organic matter. This results in a less than satisfactory prediction when using our multiple regression method. $FDOM_P$ may not be a good proxy for bulk DOC in the surface ocean, or at least within our study area, and more work is needed to further clarify contribution of $FDOM_P$ in total DOC pools in shallower waters where $FDOM_P$ and DOC appear to vary independently.

4. Conclusions

We surveyed distributions of optical properties from surface to the deep, mostly refractory DOC pool in the GoA using absorbance measurement and fluorescent component analysis. PARAFAC modeling identified four humic-like, and two protein-like fluorescent components. Variability of CDOM and humic-like components in the surface ocean is a net balance between production (*in situ* and terrestrial inputs) and loss (microbial consumption, photobleaching) processes. Biological remineralization appears to largely control the generation of CDOM and humic-like components in subsurface waters to 1000 m. Physical processes, however, play a substantial role in modulating observed distributions of CDOM and humic-like components. On the other hand, the protein-like FDOM components have higher abundances in surface waters and decrease in deeper layers, in good agreement with previous studies and in fact, match a general profile found for protein-like components on a global scale. Using a multiple linear regression between DOC and protein-like fluorescent components, we suggest that protein-like components might be used as a potential tracer for refractory DOC in the deep ocean. The refractory fraction of $FDOM_P$ in the surface ocean DOC pool appears to be much more variable where multiple addition and loss processes co-exist, and further investigation of these differences is required before similar multi-linear correlations become useful.

Acknowledgements

This study was funded by NSF-Chemical Oceanography Grant (OCE-1234388). We would like to thank the caption and crew of the R/V Melville and personnel in D. Hansell's lab. We are grateful to Y. Zhu and D. Kieber for assistance with fluorescence data collection onboard. We thank D. Hansell, C. Hopkinson, and D. Di Iorio for helpful discussions.

References

Bahram, M., Bro, R., Stedmon, C., Afkhami, A., 2006. Handling of Rayleigh and Raman scatter for PARAFAC modeling of fluorescence data using interpolation. Journal of Chemometrics 20 (3-4), 99-105.

Barker, H.A., 1981. Amino acid degradation by anaerobic bacteria. Annual review of biochemistry 50 (1), 23-40.

Blough, N.V., Del Vecchio, R., 2002. Chromophoric DOM in the coastal environment. Biogeochemistry of Marine Dissolved Organic Matter, 509-546.

Cammack, W., Kalff, J., Prairie, Y.T., Smith, E.M., 2004. Fluorescent dissolved organic matter in lakes: Relationships with heterotrophic metabolism. Limnology and Oceanography 49 (6), 2034-2045.

Coble, P.G., 1996. Characterization of marine and terrestrial DOM in seawater using excitation-emission matrix spectroscopy. Marine Chemistry 51 (4), 325-346.

Cuss, C.W., Guéguen, C., 2015. Relationships between molecular weight and fluorescence properties for size-fractionated dissolved organic matter from fresh and aged sources. Water research 68, 487-497.

Del Vecchio, R., Blough, N.V., 2002. Photobleaching of chromophoric dissolved organic matter in natural waters: kinetics and modeling. Marine Chemistry 78 (4), 231-253.

Garcia, H.E., Gordon, L.I., 1992. Oxygen solubility in seawater: Better fitting equations. Limnology and Oceanography 37 (6), 1307-1312.

Gentry-Shields, J., Wang, A., Cory, R.M., Stewart, J.R., 2013. Determination of specific types and relative levels of QPCR inhibitors in environmental water samples using excitation–emission matrix spectroscopy and PARAFAC. Water research 47 (10), 3467-3476.

Hansell, D.A., 2002. DOC in the global ocean carbon cycle. Biogeochemistry of Marine Dissolved Organic Matter, 685-715.

Hansell, D.A., Carlson, C.A., Repeta, D.J., Schlitzer, R., 2009. Dissolved organic matter in the ocean: a controversy stimulates new insights.

Hansell, D.A., Carlson, C.A., Suzuki, Y., 2002. Dissolved organic carbon export with North Pacific Intermediate Water formation. Global Biogeochemical Cycles 16 (1), 7-1-7-8.

Hood, E., Fellman, J., Spencer, R.G., Hernes, P.J., Edwards, R., D'Amore, D., Scott, D., 2009. Glaciers as a source of ancient and labile organic matter to the marine environment. Nature 462 (7276), 1044-1047.

Jørgensen, L., Stedmon, C.A., Granskog, M.A., Middelboe, M., 2014. Tracing the long-term microbial production of recalcitrant fluorescent dissolved organic matter in seawater. Geophysical Research Letters 41 (7), 2481-2488.

Jørgensen, L., Stedmon, C.A., Kragh, T., Markager, S., Middelboe, M., Søndergaard, M., 2011. Global trends in the fluorescence characteristics and distribution of marine dissolved organic matter. Marine Chemistry 126 (1), 139-148.

Keil, R.G., Kirchman, D.L., 1994. Abiotic transformation of labile protein to refractory protein in sea water. Marine Chemistry 45 (3), 187-196.

Kim, J., Kim, G., 2015. Importance of colored dissolved organic matter (CDOM) inputs from the deep sea to the euphotic zone: Results from the East (Japan) Sea. Marine Chemistry 169, 33-40.

Kowalczuk, P., Tilstone, G.H., Zabłocka, M., Röttgers, R., Thomas, R., 2013. Composition of dissolved organic matter along an Atlantic Meridional Transect from fluorescence spectroscopy and Parallel Factor Analysis. Marine Chemistry 157, 170-184.

Medeiros, P., Seidel, M., Powers, L.C., Dittmar, T., Hansell, D.A., Miller, W.L., 2015. Dissolved organic matter composition and photochemical transformations in the northern North Pacific Ocean. Geophysical Research Letters.

Mopper, K., Schultz, C.A., 1993. Fluorescence as a possible tool for studying the nature and water column distribution of DOC components. Marine Chemistry 41 (1), 229-238.

Murphy, K.R., Butler, K.D., Spencer, R.G., Stedmon, C.A., Boehme, J.R., Aiken, G.R., 2010. Measurement of dissolved organic matter fluorescence in aquatic environments: an interlaboratory comparison. Environmental Science & Technology 44 (24), 9405-9412.
Murphy, K.R., Stedmon, C.A., Waite, T.D., Ruiz, G.M., 2008. Distinguishing between terrestrial and autochthonous organic matter sources in marine environments using fluorescence spectroscopy. Marine Chemistry 108 (1), 40-58.

Neal, E.G., Hood, E., Smikrud, K., 2010. Contribution of glacier runoff to freshwater discharge into the Gulf of Alaska. Geophysical Research Letters 37 (6).

Nelson, N.B., Carlson, C.A., Steinberg, D.K., 2004. Production of chromophoric dissolved organic matter by Sargasso Sea microbes. Marine Chemistry 89 (1), 273-287.

Nelson, N.B., Siegel, D.A., 2002. Chromophoric DOM in the open ocean. Biogeochemistry of Marine Dissolved Organic Matter, 547-578.

Nelson, N.B., Siegel, D.A., Carlson, C.A., Swan, C.M., 2010. Tracing global biogeochemical cycles and meridional overturning circulation using chromophoric dissolved organic matter. Geophysical Research Letters 37 (3).

Peterson, T.D., Whitney, F.A., Harrison, P.J., 2005. Macronutrient dynamics in an anticyclonic mesoscale eddy in the Gulf of Alaska. Deep Sea Research Part II: Topical Studies in Oceanography 52 (7), 909-932.

Reader, H.E., Miller, W.L., 2011. Effect of estimations of ultraviolet absorption spectra of chromophoric dissolved organic matter on the uncertainty of photochemical production calculations. Journal of Geophysical Research: Oceans (1978–2012) 116 (C8).

Spencer, R.G.M., Bolton, L., Baker, A., 2007. Freeze/thaw and pH effects on freshwater dissolved organic matter fluorescence and absorbance properties from a number of UK locations. Water research 41 (13), 2941-2950.

Stedmon, C.A., Bro, R., 2008. Characterizing dissolved organic matter fluorescence with parallel factor analysis: a tutorial. Limnol. Oceanogr. Methods 6, 572-579.

Stedmon, C.A., Markager, S., 2005. Tracing the production and degradation of autochthonous fractions of dissolved organic matter by fluorescence analysis. Limnology and Oceanography 50 (5), 1415-1426.

Steele, M., Morison, J., Ermold, W., Rigor, I., Ortmeyer, M., Shimada, K., 2004. Circulation of summer Pacific halocline water in the Arctic Ocean. Journal of Geophysical Research: Oceans (1978–2012) 109 (C2).

Swan, C.M., Siegel, D.A., Nelson, N.B., Carlson, C.A., Nasir, E., 2009. Biogeochemical and hydrographic controls on chromophoric dissolved organic matter distribution in the Pacific Ocean. Deep Sea Research Part I: Oceanographic Research Papers 56 (12), 2175-2192.

Yamashita, Y., Cory, R.M., Nishioka, J., Kuma, K., Tanoue, E., Jaffé, R., 2010. Fluorescence characteristics of dissolved organic matter in the deep waters of the Okhotsk Sea and the northwestern North Pacific Ocean. Deep Sea Research Part II: Topical Studies in Oceanography 57 (16), 1478-1485.

Yamashita, Y., Tanoue, E., 2003. Chemical characterization of protein-like fluorophores in DOM in relation to aromatic amino acids. Marine Chemistry 82 (3), 255-271.

Yamashita, Y., Tanoue, E., 2004. Chemical characteristics of amino acid-containing dissolved organic matter in seawater. Organic Geochemistry 35 (6), 679-692.

Yamashita, Y., Tanoue, E., 2009. Basin scale distribution of chromophoric dissolved organic matter in the Pacific Ocean. Limnology and Oceanography 54 (2), 598-609.

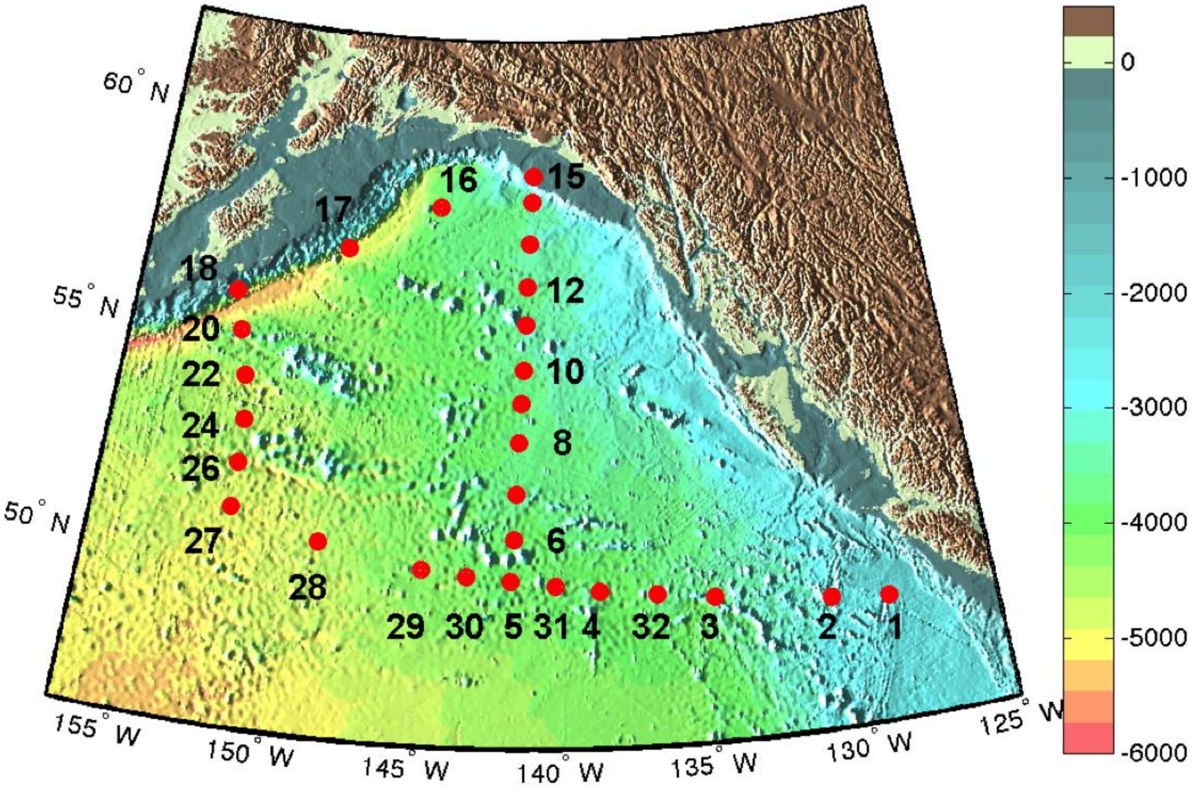

Figure 5.1: Map of study area in the Gulf of Alaska (GoA) with bathymetry denoted with the color bar on the right. Red circles indicate the sampling stations.

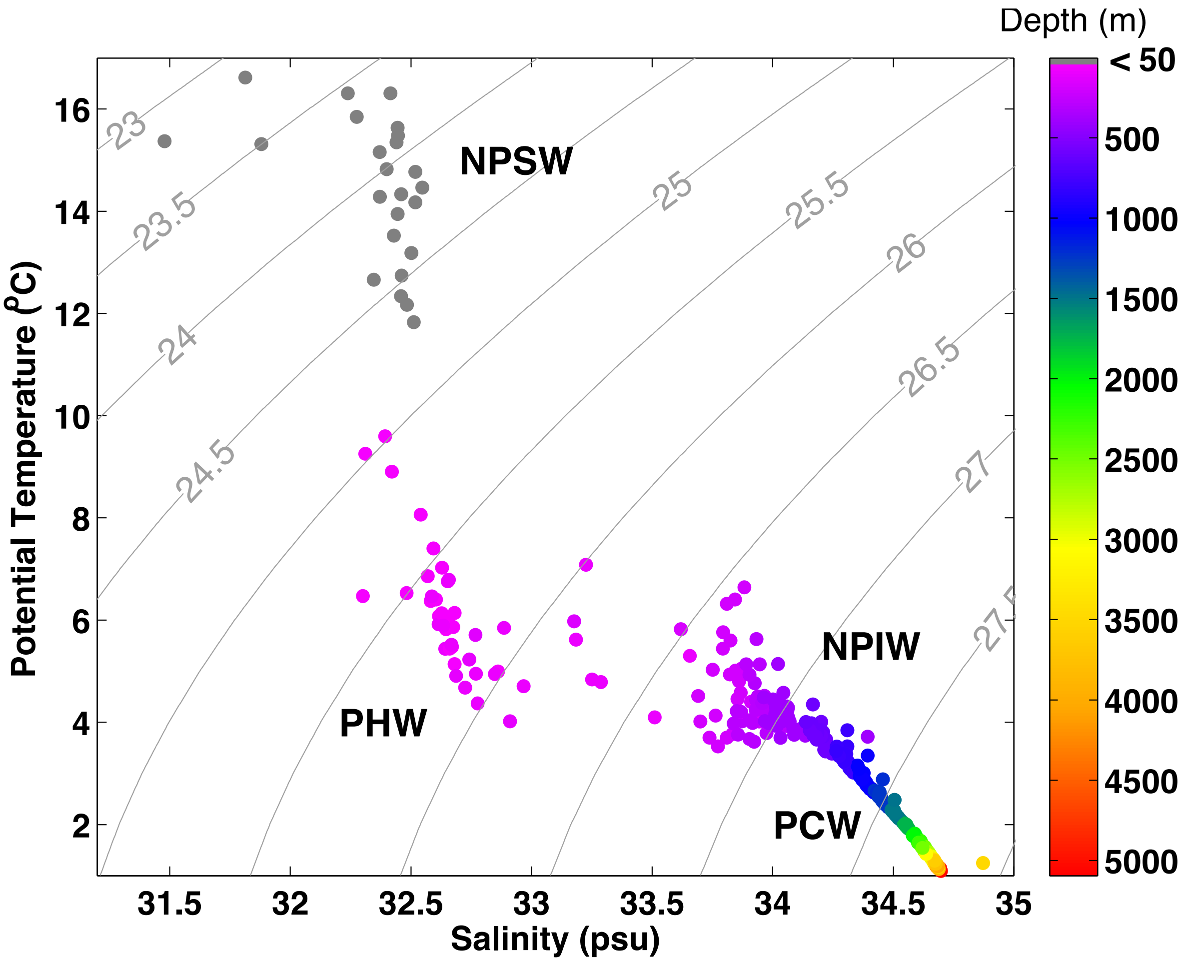

Figure 5.2: Potential temperature-salinity (T-S) diagram of the study area, superimposed with potential density anomaly (σ_θ) contour lines (*isopycnals*) in gray.

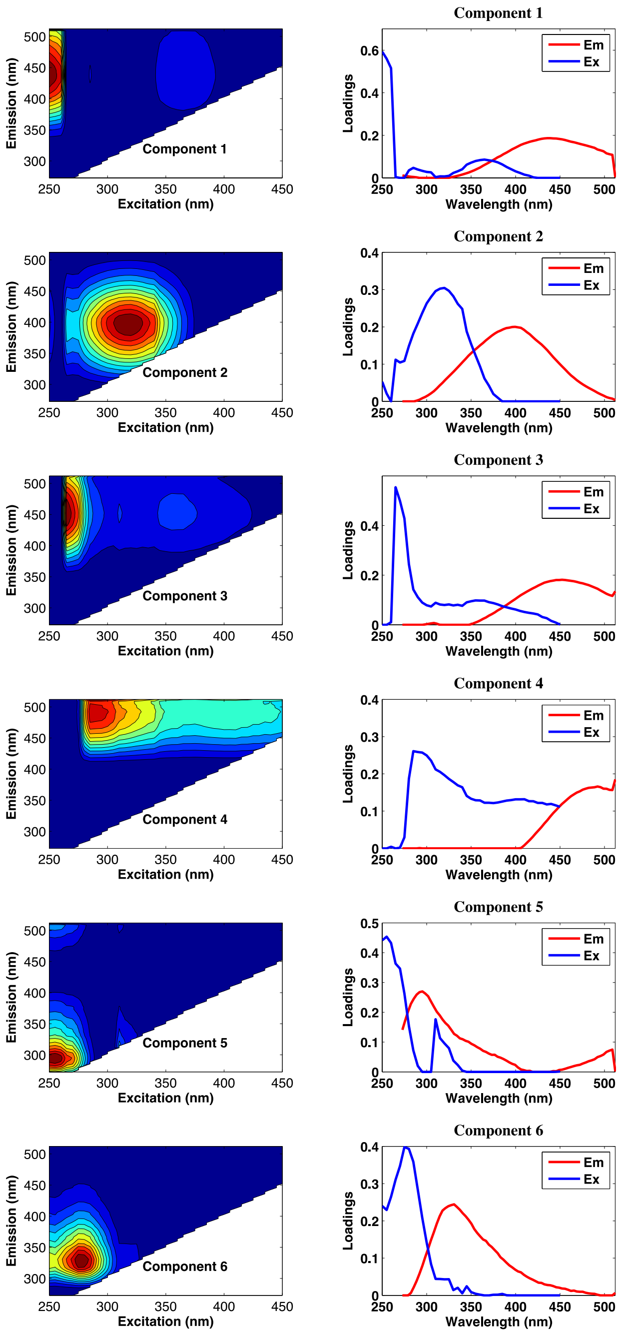

Figure 5.3: Contour plots (left column) and spectral characteristics (right column) for the six fluorescent components revealed and validated using PARAFAC modeling.

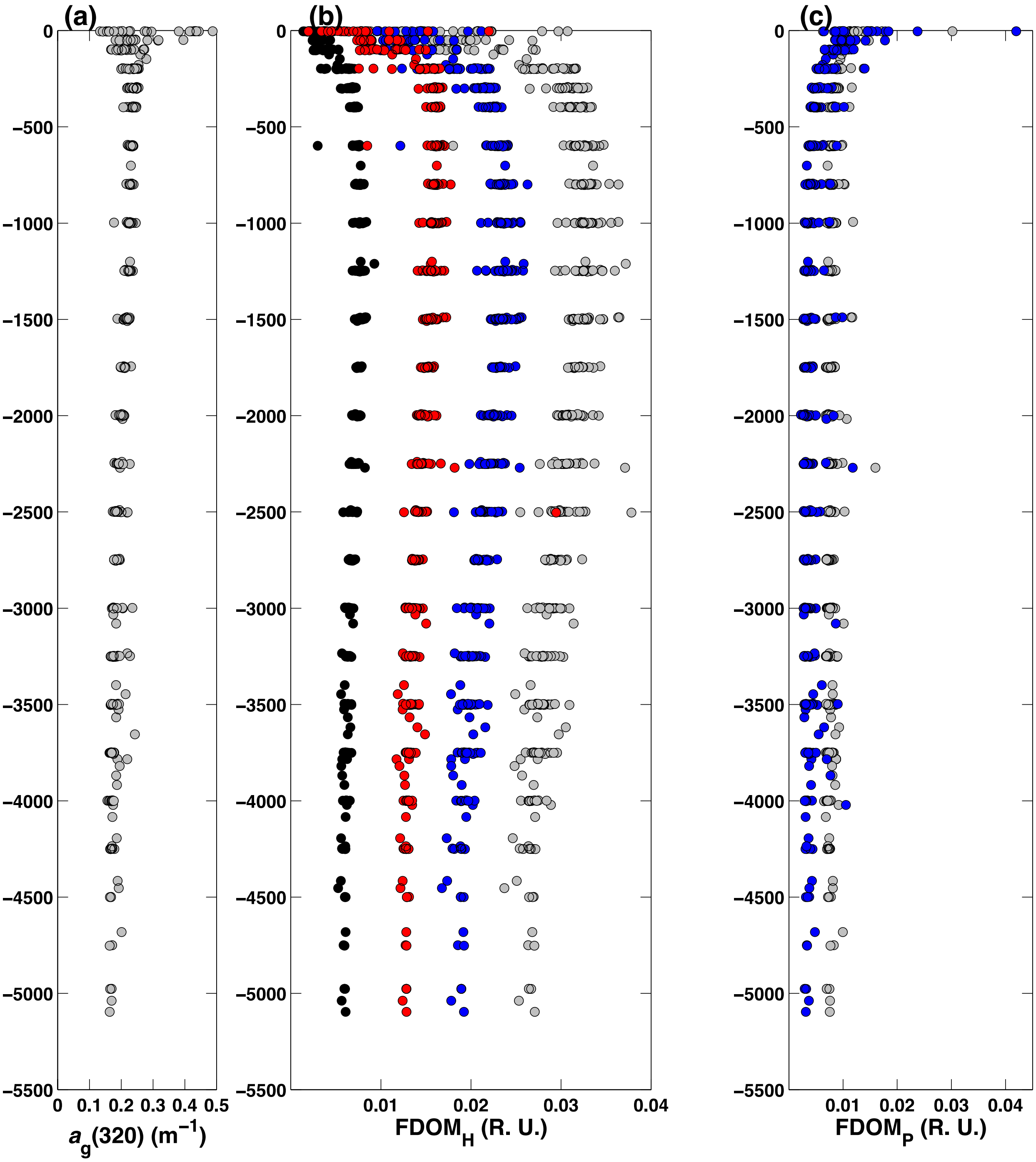

Figure 5.4: Vertical profiles of (a) CDOM (defined using $a_g(320)$); (b) humic-like fluorescent components of C1 (gray), C2 (red), C3 (blue) and C4 (black); and (c) protein-like fluorescent components of C5 (gray) and C6(blue).

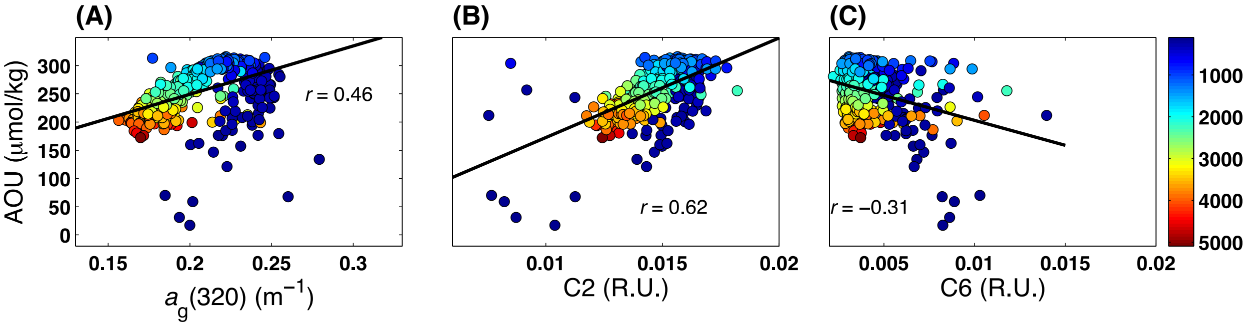

Figure 5.5: Correlations between AOU to (A) CDOM; (B) humic-like component C2; and (C) protein-like component C6. Sampling depth is denoted with color bar on the right. Data within depth < 100 m were not included.

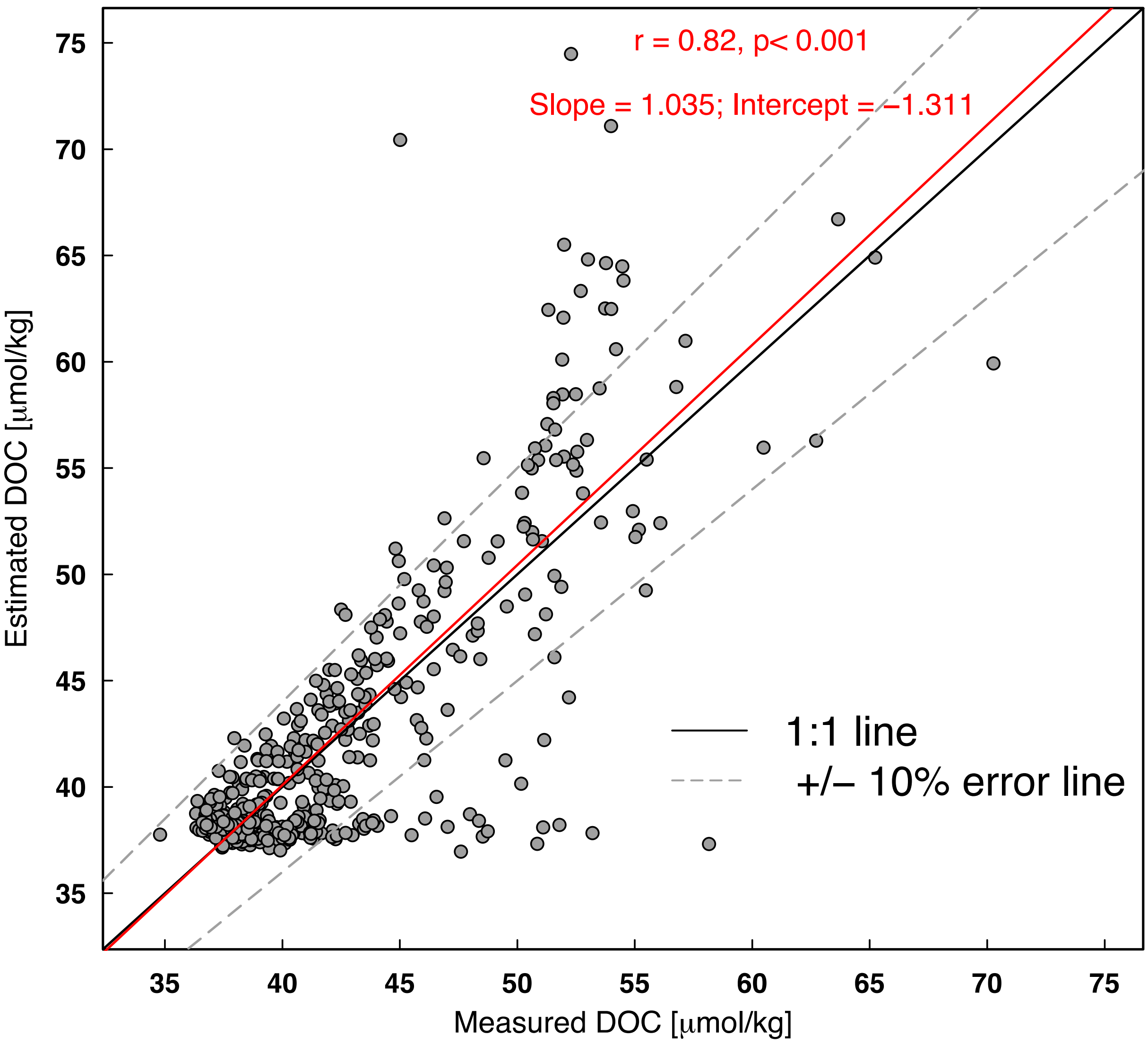

Figure 5.6: Estimating DOC as a function of protein-like fluorescent components. Red line represents the regression relation between estimated DOC and measured DOC.

CHAPTER 6

CONCLUSIONS AND FUTURE WORK

Modeling UV photochemistry from space has been and remains a critical and challenging endeavor. Building upon the work of Fichot et al. (2008) and Fichot and Miller (2010), this dissertation developed new optical techniques and approaches (remote sensing, fluorescence) to explore UV optical properties and fluorescent components in the ocean making several new and unique contributions.

1) I optimized the original Sea*UV*/Sea*UV*c algorithms (Fichot et al., 2008) for inshore, optically complex surface waters and developed a composite set of algorithms that can retrieve the diffuse attenuation coefficient, $K_{d,}$ over the UV spectral range from visible ocean color with good accuracy almost all water types found in the ocean, obtaining a mean relative error of 13% for $K_d(340)$ for example. This composite set of algorithms provide significantly improved accuracy for describing UV penetration into surface waters, a critical element for quantifying the role of solar UV radiation in photo-dependent processes in the ocean.

2) I developed a new optical algorithm (labeled Sea*CDOM*) that accurately resolves the CDOM absorption spectra in the UV and blue visible wavelengths (275-450nm) directly from ocean color, with a mean absolute percent difference for a_g in the UV of ~25% across the spectrum. This is a novel contribution to the oceanographic remote sensing community. One of its advantages is that no a priori assumptions of the CDOM absorption spectral shape is required, making the retrieved spectrum free of the known errors arising from selection of a single exponential slope coefficient for extrapolation from visible wavelengths that have hampered

previous models. My new approach should provide new synoptic insight about the chemical composition (e.g. molecular weight and aromaticity), origins, transformation and cycling pathways of CDOM.

3) I introduced a new approach for retrieving the *in situ* UV radiation field required for calculating photochemical rates by blending our two distinct algorithms (i.e. composite Sea*UV* and Sea*CDOM*) for application to a single high-resolution coastal satellite image and estimating CO photoproduction in a Georgia coastal estuarine setting. I demonstrated the strong spatial variability of depth-specific and depth-integrated photoproduction rates for CO on a small estuarine scale. This new capability for independent retrievals of a_g and K_d allows quantitative partitioning of UV photons between CDOM and other optical constituents, producing greatly improved estimates for photochemistry in complex waters.

4) I investigated the optical properties (absorption and fluorescence) of the waters in the Northeastern North Pacific Ocean where deep ocean circulation has isolated predominantly old and bio-refractory DOM. Four humic-like and two protein-like fluorescent components were identified from synoptic sampling throughout the Gulf of Alaska. Variability of CDOM and humic-like components in the surface ocean result from a balance between production (*in situ* additions, terrestrial input) and loss (microbial consumption, photobleaching) processes. Further, by setting up a multiple linear regression between DOC concentrations and the protein-like component flourescence, I demonstrate that protein-like components may serve as a tracer for refractory DOC in the deep ocean. Further research is needed to fully constrain the variability of this protein-like refractory component within the entire DOC pool, potentially extending the applicability of this correlation to the surface ocean where multiple addition and loss processes co-exist.

Several issues regarding the estimation of oceanic UV properties from satellite platforms are worthy of noting, although they remain beyond the scope of this dissertation work. First, it should be noted that the two ocean color algorithms developed and presented herein rely heavily on statistical approaches and consequently, may give erroneous estimates when applied to waters that were not included in the training processes. Moreover, since a classification method was involved in the algorithm development and accurate estimates are critically dependent on correct classification of ocean color pixels, especially for the Sea*CDOM* algorithm where cluster analysis is an indispensible step, high quality ocean color data is optimal. It is also important to note that our algorithms were developed from *in situ* buoy derived ocean color data, correlation to data obtained from satellite platforms can be fraught with possible errors. The very best validation for retrieving optical properties using satellite ocean color observations cannot reach its full potential until a solid atmospheric correction procedure is established, especially for dynamic coastal waters where an imperfect atmospheric correction is often present. Nevertheless, for open ocean waters where atmospheric correction procedures are mature, a match-up analysis between *in situ* data and matched satellite R_{rs} (satellite overpass within a ± 3 hr time window and a 5×5 pixel size (~5 × 5 km)) (Harding *et al.*, 2005) can be pursued to evaluate the capability of the algorithms in estimating UV properties regarding satellite ocean color.

Another direction of particular interest is the quantification of CO_2 photoproduction fluxes in the surface waters from ocean color. Blending the two independent ocean color algorithms presented in this dissertation, with appropriate photochemical parameters (AQY for CO_2) is currently a work in progress. The ability to better quantify the photochemical production of CO_2 and more fully constrain the role of photochemistry within the global carbon cycle scale using ocean color will be a major advance.

A third promising direction will be to extend the methodology presented in this dissertation to emerging satellite missions, especially hyperspectral remote sensing techniques with enhanced spatial and spectral resolutions. The idea of estimating a_g(UV) properties from visible ocean color is greatly benefited from multivariate statistical methods such as data dimension reduction (i.e., PCA) techniques. With increased interest in coastal waters, the dimension reduction technique presented in this dissertation can potentially be easily adapted to hyperspectral ocean color data by applying an empirical orthogonal function analysis (for example) and provide critical information on the magnitude of the UV effect on dynamic nearshore ecosystems.

References

Fichot, C. G., Sathyendranath, S., & Miller, W. L. (2008). SeaUV and SeaUV C: Algorithms for the retrieval of UV/Visible diffuse attenuation coefficients from ocean color. *Remote Sensing of Environment*, *112*(4), 1584-1602.

Fichot, C. G., & Miller, W. L. (2010). An approach to quantify depth-resolved marine photochemical fluxes using remote sensing: Application to carbon monoxide (CO) photoproduction. *Remote Sensing of Environment*, *114*(7), 1363-1377.

Harding, L. W., Magnuson, A., & Mallonee, M. E. (2005). SeaWiFS retrievals of chlorophyll in Chesapeake Bay and the mid-Atlantic bight. *Estuarine, Coastal and Shelf Science*, *62*(1), 75-94.

APPENDIX A

IMPLEMENTATION SCHEMES FOR COMPOSITE SEAUV/SEAUVC ALGORITHMS[6]

---

[6] Appendix for :
Cao, F., Fichot, C. G., Hooker, S. B., & Miller, W. L. (2014). *Remote Sensing of Environment*, *144*, 11-27, doi:10.1016/j.rse.2014.01.003; Reprinted here with permission of the publisher.

Introduction:

This appendix is to provide a step-by-step implementation tutorial for the composite SeaUV/SeaUVc algorithms presented in Chapter 2. Included are the implementation schemes (Figure A.1) and parameters (Table A.1-A.13)

A.1. Required inputs

The remote-sensing reflectance, R_{rs} (λ,0^+), measured at λ = 412, 443, 490, 510, 555 and 670 nm (SeaWiFS wavebands) is required for initial input to the algorithms. Normalized water-leaving radiance nL_w(λ) can be converted into R_{rs} (λ,0^+) as follows: $R_{rs}(\lambda, 0^+) = nL_W(\lambda)/\overline{F_O}(\lambda)$ where the values for the mean extraterrestrial solar flux, $\overline{F_O}(\lambda)$, are provided in Thuillier et al. (2003).

A.2. Retrieving K_d(490) using the NASA K_d(490) algorithm.

The measured remote-sensing reflectance R_{rs} (λ,0^+) data are first processed through the NASA K_d(490) algorithm (Werdell, 2009) to determine the appropriate set of composite algorithms for use. If the calculated K_d(490) value is lower than 0.32 m^{-1}, the water is classified as “clear” and the first part in the new composite set of Sea*UV* algorithms is used for K_d(λ) retrieval. If the calculated K_d(490) is greater than or equal to 0.32 m^{-1}, the water is classified as optically complex inshore water and the inshore-water optimized Sea*UV* (i.e the second part in the new composite set of Sea*UV* algorithms) is applied for K_d(λ) retrieval.

A.3. Retrieving K_d(λ) using original SeaUV.

For “clear” water, the original Sea*UV*/Sea*UVc* model is implementated on the R_{rs} (λ,0^+) values using the same procedure as described in Appendix *C.1.* and *C. 2.* in Fichot et al. (2008). As stated in the text, we have taken advantage of the empirical nature of the Sea*UV* algorithms and updated all parameters used in the original Sea*UV* algorithm with the exception of the cluster centers coordinates, which proved robust, with relocation giving no significant improvement to the statistical fit for the training data. The values of $\bar{R}(\lambda)$ and $\sigma_R(\lambda)$ calculated for standardization from our largest training data set ($N = 563$) are given in Table A. 1. The resulting standardized log-linearized remote-sensing reflectances, $X(\lambda)$, can then be used in linear combinations to calculate the scores of the first four principal components. The eigenvectors derived from our large training data set through PCA are used as the correlation coefficients for the multi-linear combinations. The PC scores are updated ((Table A.2.) and calculated as in Eq. (1) in Fichot et al. (2008) (e.g. PC score on the first principal component is computed as

$[\mathrm{PC1}]_i = e_{11}X_i(412)+ e_{12}X_i(443)+ e_{13}X_i(490)+ e_{14}X_i(510)+ e_{15}X_i(555)+ e_{16}X_i(670))$,

where

e_{11}= -0.3976, e_{12}= -0.4237, e_{13}= -0.4521, e_{14}= -0.4540, e_{15}= -0.4159, e_{16}= -0.2809. Scores on PC2, PC3 and PC4 are calculated similarly and are then used as the independent variables in the multi-linear regressions to predict K_d. The correlation coefficients (parameters $\alpha, \beta, \gamma, \delta, \varepsilon$) have been updated and are provided in Table A.3. For the clear water Sea*UVc* model, the cluster centers in the updated Sea*UVc* are the same as published in Fichot et al. (2008). The observations are assigned to their optical domains using the first two PC scores and log-linearized $K_\mathrm{d}(\lambda)$ is calculated by using Eq. (4) in Fichot et al. (2008) with the updated parameters corresponding to the identified optical domains provided in here Tables A.4, A.5 and A.6.

A.4. Retrieving $K_d(\lambda)$ using inshore-water optimized SeaUV/SeaUVc.

If the calculated $K_\mathrm{d}(490)$ is greater than or equal to 0.32 m^{-1} and the water is classified as optically complex, inshore water, the new inshore-water optimized Sea*UV*/Sea*UVc* model provides a much more accurate retrieval of $K_\mathrm{d}(\lambda)$. The inshore-water optimized Sea*UV* model is then used with similar logic to that used for implementation of the original Sea*UV* (as described in Fichot et al. (2008)). The parameters for standardization, calculation of PC scores and multi-linear coefficients are provided in Tables A.7, A.8 and A.9. For the inshore-water optimized Sea*UVc* algorithms, four dark water domains (DWDs) are defined for retrieving $K_d(\lambda)$. The coordinates of the four cluster centers in inshore-water optimized *SeaUVc* are provided in Table A.10. Each observation is assigned to the appropriate DWD by using the first two PC scores, allowing the log-linearized $K_d(\lambda)$ value to be calculated using Eq. (4) in Fichot et al. (2008) using the updated parameters for use in corresponding to the dark water domain provided here in Tables A.11, A.12 and A.13.

Table A.1

Updated mean and standard deviations to center and standardize ln(R_{rs} (λ,0^+)) for the original Sea*UV/*Sea*UVc* algorithms.

	λ = 412	λ = 443	λ = 490	λ = 510	λ = 555	λ = 670
	-5.3340	-5.2589	-5.0970	-5.2474	-5.5939	-7.9649
$\bar{R}(\lambda)$	0.8637	0.7808	0.7268	0.7483	0.8208	0.8836
$\sigma_R(\lambda)$						

Table A.2

Updated first four eigenvectors for use in calculating the PC scores for the “original” Sea*UV/*Sea*UVc* algorithms.

	λ = 412	λ = 443	λ = 490	λ = 510	λ = 555	λ = 670
e_1	-0.3976	-0.4237	-0.4521	-0.4540	-0.4159	-0.2809
e_2	0.4481	0.3497	0.1303	-0.0670	-0.3652	-0.7226
e_3	0.3990	0.2370	-0.1326	-0.3724	-0.4920	0.6215
e_4	0.5829	-0.2240	-0.5733	-0.1354	0.5045	-0.0928

Table A.3

Updated parameters for retrieval of $\ln(K_d(\lambda))$ from the PC scores in the original Sea*UV* algorithms.

	α	β	γ	δ	ε
$\ln(K_d(320))$	-0.7327	0.0980	-0.5928	-0.5230	-1.1130
$\ln(K_d(340))$	-1.0625	0.0855	-0.6301	-0.4996	-0.8653
$\ln(K_d(380))$	-1.6508	0.0485	-0.6565	-0.4154	-0.4186
$\ln(K_d(412))$	-1.9638	0.0240	-0.6550	-0.3240	0.1644
$\ln(K_d(443))$	-2.1846	0.0088	-0.6256	-0.2368	0.6171
$\ln(K_d(490))$	-2.4894	-0.0025	-0.5574	-0.0733	0.6902

Table A.4

Updated parameters for retrieval of ln[$K_d(\lambda)$] (λ = 320 and 340 nm) from the PC scores in the original Sea*UVc* algorithms.

	α	β	γ	δ	ε
ln[K_d(320)]					
OCD1	-0.7880	0.0555	-0.6148	-0.3852	-0.7067
OCD2	-0.8138	0.1098	-0.6411	0.6162	-0.9544
OCD3	-0.6073	0.1372	-0.5505	-0.1169	-1.7478
OCD4	-0.7821	0.1357	-0.5775	-0.4700	-0.5023
OCD5	-0.4816	-0.0044	-0.5721	-0.6300	-1.1761
OCD6	-0.8359	0.1386	-0.4460	-0.6736	-0.9057
OCD7	-0.7764	0.1411	-0.5378	-0.6900	-0.8205
ln[K_d(340)]					
OCD1	-1.0733	0.0588	-0.6328	-0.3243	-0.6286
OCD2	-1.1055	0.0981	-0.6514	-0.5232	-0.7947
OCD3	-0.8734	0.1260	-0.5453	-0.1725	-1.7031
OCD4	-1.1280	0.1202	-0.6284	-0.5058	-0.4116
OCD5	-0.9525	0.0376	-0.6103	-0.5717	-1.0074
OCD6	-1.1507	0.1015	-0.5148	-0.5969	-0.6982
OCD7	-1.0968	0.1140	-0.5800	-0.7075	-0.6110

Table A.5

Updated parameters for retrieval of ln[$K_d(\lambda)$] (λ = 380 and 412 nm) from the PC scores in the original Sea*UVc* algorithms.

	α	β	γ	δ	ε
ln[K_d(380)]					
OCD1	-1.6649	0.0356	-0.6626	-0.1942	-0.2820
OCD2	-1.6453	0.0542	-0.6710	-0.3232	-0.5304
OCD3	-1.2807	0.1287	-0.5558	-0.2712	-1.9238
OCD4	-1.8815	0.0860	-0.7529	-0.4659	0.4369
OCD5	-1.5699	0.0055	-0.5469	-0.6102	-0.7134
OCD6	-1.7408	0.0601	-0.5786	-0.6292	-0.2607
OCD7	-1.7133	0.0770	-0.5789	-0.6661	-0.2665
ln[K_d(412)]					
OCD1	-2.066	-0.0117	-0.5788	-0.0081	0.1561
OCD2	-1.9402	0.0273	-0.6691	-0.1097	-0.0423
OCD3	-1.5982	0.1176	-0.5712	-0.0780	-1.3923
OCD4	-2.1512	0.0492	-0.7311	-0.2785	0.4277
OCD5	-1.9057	-0.0093	-0.5560	-0.6052	-0.1428
OCD6	-2.0421	0.0255	-0.6314	-0.5377	0.4598
OCD7	-2.0247	0.0667	-0.5683	-0.6719	0.0959

Table A.6

Updated parameters for retrieval of $\ln[K_d(\lambda)]$ (λ = 443 and 490 nm) from the PC scores in the original Sea*UVc* algorithms.

	α	β	γ	δ	ε
$\ln[K_d(443)]$					
OCD1	-2.4117	-0.0551	-0.5317	0.0673	0.6669
OCD2	-2.1752	0.0009	-0.6672	0.0970	0.2309
OCD3	-1.7932	0.1273	-0.5862	0.0473	-1.0485
OCD4	-2.4883	0.1158	-0.6174	-0.3085	0.9051
OCD5	-2.1744	-0.0030	-0.5205	-0.5934	0.4998
OCD6	-2.2708	-0.0002	-0.6345	-0.4557	1.0245
OCD7	-2.2943	0.0654	-0.4923	-0.6039	0.4254
$\ln[K_d(490)]$					
OCD1	-3.0337	-0.1438	-0.5119	0.0357	1.7743
OCD2	-2.5423	-0.0575	-0.6011	0.3010	0.3775
OCD3	-2.1348	0.1232	-0.5911	0.2175	-1.0509
OCD4	-2.6192	0.0104	-0.5910	-0.3303	0.8374
OCD5	-2.5263	0.0150	-0.3711	-0.4385	0.8056
OCD6	-2.5759	-0.0115	-0.6348	-0.2714	1.0642
OCD7	-2.6486	0.0952	-0.3854	-0.4047	0.5484

Table A.7

Updated mean and standard deviations to center and standardize $\ln(R_{rs}(\lambda,0^+))$ for the inshore-water optimized Sea*UV/*Sea*UVc* algorithms.

	$\lambda = 412$	$\lambda = 443$	$\lambda = 490$	$\lambda = 510$	$\lambda = 555$	$\lambda = 670$
$\bar{R}(\lambda)$	-6.8156	-6.3098	-5.6367	-5.4596	-5.0692	-5.9379
$\sigma_R(\lambda)$	1.0703	0.9956	0.8839	0.8599	0.7490	0.7485

Table A.8

Updated first four eigenvectors for use in calculating the PC scores for the inshore-water optimized Sea*UV/*Sea*UVc* algorithms.

	$\lambda = 412$	$\lambda = 443$	$\lambda = 490$	$\lambda = 510$	$\lambda = 555$	$\lambda = 670$
e_1	-0.4019	-0.4224	-0.4295	-0.4297	-0.4240	-0.3333
e_2	-0.4536	-0.2541	-0.0825	-0.0403	0.1504	0.8358
e_3	0.5303	0.2160	-0.1431	-0.3003	-0.6103	0.4337
e_4	-0.4941	0.2907	0.4526	0.3252	-0.6005	-0.0113

Table A.9

Updated parameters for retrieval of ln($K_d(\lambda)$) from the PC scores in the inshore-water optimized Sea*UV* algorithm.

	α	β	γ	δ	ε
ln(K_d(320))	1.7574	0.1253	1.0342	-0.3073	0.8648
ln(K_d(340))	1.4696	0.1181	0.9701	-0.1030	0.6973
ln(K_d(380))	0.9983	0.1117	0.9816	0.1098	0.5601
ln(K_d(412))	0.6930	0.1200	0.9512	0.3410	0.0220
ln(K_d(443))	0.4314	0.1130	0.9268	0.4504	-0.2891
ln(K_d(490))	0.0530	0.0927	0.9158	0.5754	-0.3118

Table A.10

Coordinates of the cluster centers corresponding to the four dark water domains defined in this study for the inshore-water optimized Sea*UVc* algorithms.

n	X_n (PC1)	Y_n (PC2)
DWD1	-4.4836	-0.2043
DWD2	0.8671	-0.3379
DWD3	2.2617	-0.0836
DWD4	-0.0862	0.6324

Table A.11

Updated parameters for retrieval of ln[$K_d(\lambda)$] (λ = 320 and 340 nm) from the PC scores in the inshore-water optimized Sea*UVc* algorithms.

	α	β	γ	δ	ε
ln[K_d(320)]					
DWD1	1.8181	0.1394	0.9296	0.0974	0.1340
DWD2	1.4925	0.4003	1.1138	-0.5654	0.9708
DWD3	1.8445	0.0797	0.8835	-0.9424	0.9792
DWD4	1.8433	0.2955	0.9879	0.0173	0.4808
ln[K_d(340)]					
DWD1	1.4029	0.0950	0.9244	0.2621	-0.1177
DWD2	1.2840	0.3588	1.0551	-0.2270	0.9539
DWD3	1.4194	0.1288	0.8501	-0.6873	0.7522
DWD4	1.5157	0.2423	0.9216	0.1778	0.2762

Table A.12

Updated parameters for retrieval of ln[$K_d(\lambda)$] (λ = 380 and 412 nm) from the PC scores in the inshore-water optimized Sea*UVc* algorithms.

	α	β	γ	δ	ε
ln[K_d(380)]					
DWD1	0.8770	0.0888	0.8222	0.5918	-0.7150
DWD2	0.9102	0.2414	1.0345	-0.0173	0.7401
DWD3	0.8756	0.1416	0.8838	-0.5368	0.6536
DWD4	1.0861	0.2472	0.8983	0.5389	0.3796
ln[K_d(412)]					
DWD1	0.8069	0.1642	0.7620	0.5546	-1.2081
DWD2	0.6699	0.1845	0.9643	0.2231	0.2031
DWD3	0.6022	0.1261	0.8923	-0.1241	0.1357
DWD4	0.8078	0.2412	0.8606	0.8385	-0.0013

Table A.13

Updated parameters for retrieval of ln[$K_d(\lambda)$] (λ = 443 and 490 nm) from the PC scores in the inshore-water optimized Sea*UVc* algorithms

	α	β	γ	δ	ε
ln[K_d(443)]					
DWD1	0.5266	0.1574	0.6767	0.6478	-1.5230
DWD2	0.4115	0.1525	0.9055	0.3685	-0.1893
DWD3	0.3490	0.1162	0.8966	0.0601	-0.1541
DWD4	0.5585	0.2460	0.8400	0.9705	-0.1524
ln[K_d(490)]					
DWD1	0.0891	0.1175	0.6923	0.5053	-1.6898
DWD2	0.0144	0.1224	0.8882	0.4612	-0.2901
DWD3	-0.0369	0.1051	0.8915	0.1950	-0.1502
DWD4	0.1827	0.2437	0.8325	1.1980	-0.1505

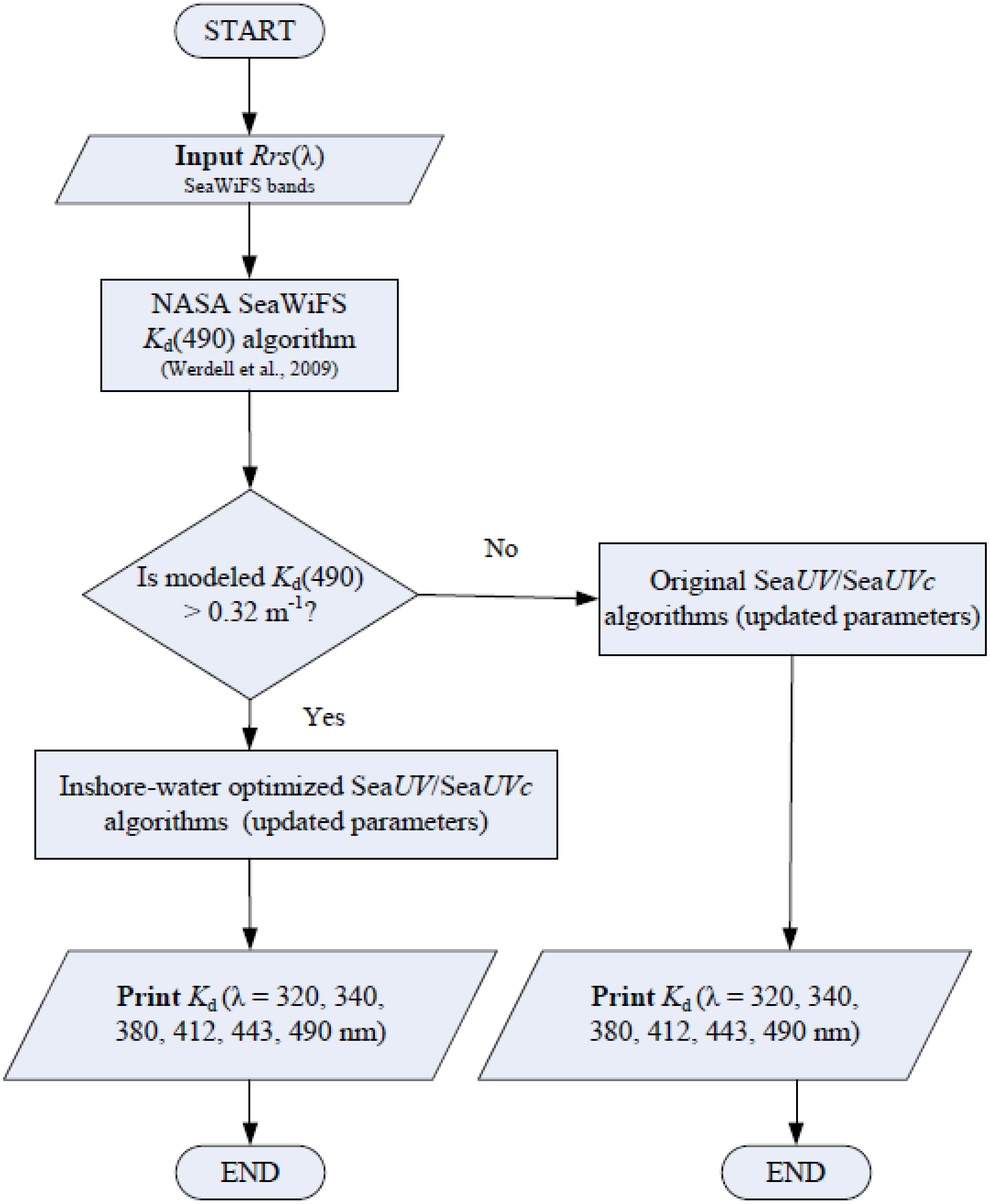

Figure A.1: Flow chart diagram for implementation of optimized composite Sea*UV*/Sea*UVc* algorithms.

APPENDIX B

ONLINE SUPPLEMENTARY MATERIAL FOR CHAPTER 2[7]

---

[7] Online supporting material for:
Cao, F., Fichot, C. G., Hooker, S. B., & Miller, W. L. (2014). *Remote Sensing of Environment*, *144*, 11-27, doi:10.1016/j.rse.2014.01.003; Reprinted here with permission of the publisher.

Introduction:

This appendix includes performances and fitting parameters of re-parameterization of the original algorithms through retraining the complete data set (N = 438), as briefly described in section 3.2 in Chapter 2 (Table S 2.1-S 2.6, Figure S 2.1); and dark-water optimized Sea*UV*/Sea*UVc* algorithms (derived from N = 119, Table S 2.7-S 2.13, Figure S 2.2) as intermediate step toward the final "optimized composite SeaUV/SeaUVc algorithm" product.

Fitting parameters for reparameterized original Sea*UV*/Sea*UVc* algorithms:

Table S 2.1: Mean and standard deviations to center and standardize ln(Rrs (λ,0+)) for reparameterized original Sea*UV*/Sea*UVc* algorithms.

	λ = 412	λ = 443	λ = 490	λ = 510	λ = 555	λ = 670
$\bar{R}(\lambda)$	-5.6342	-5.4550	-5.1500	-5.2036	-5.3490	-7.3595
$\sigma_R(\lambda)$	1.1652	0.9852	0.8143	0.7850	0.8208	1.2517

Table S 2.2: First four eigenvectors to use to calculate the PC scores for reparameterized original Sea*UV*/Sea*UVc* algorithms.

	λ = 412	λ = 443	λ = 490	λ = 510	λ = 555	λ = 670
e_1	-0.4253	-0.4586	-0.4866	-0.4801	-0.3688	-0.0740
e_2	0.3630	0.2566	0.0485	-0.1282	-0.4863	-0.7397
e_3	0.3471	0.2999	-0.0111	-0.2879	-0.5166	0.6632
e_4	0.6297	-0.1125	-0.5318	-0.2755	0.4806	-0.0329

Table S 2.3: Parameters for retrieval of $\ln(K_d(\lambda))$ from the PC scores in reparameterized original Sea*UV*.

	α	β	γ	δ	ε
$\ln(K_d(320))$	-0.1077	0.3010	-0.9269	-0.1557	-1.7915
$\ln(K_d(340))$	-0.4201	0.2916	-0.9466	-0.1340	-1.4141
$\ln(K_d(380))$	-0.9657	0.2740	-0.9984	-0.0338	-0.9991
$\ln(K_d(412))$	-1.2548	0.2677	-0.9988	0.0520	-0.3960
$\ln(K_d(443))$	-1.4712	0.2576	-0.9785	0.1465	-0.0371
$\ln(K_d(490))$	-1.7921	0.2398	-0.9439	0.3222	0.0048

Table S 2.4: Parameters for retrieval of ln[$K_d(\lambda)$] (λ = 320 and 340 nm) from the PC scores in reparameterized original Sea*UV*.

	α	β	γ	δ	ε
ln[K_d(320)]					
OCD1	-0.4139	0.1800	-0.6818	-0.2689	-0.7837
OCD2	-0.7492	0.1748	-1.3012	-0.2106	-1.6625
OCD3	-0.1983	0.3699	-1.0110	0.5994	-2.7084
OCD4	-0.6510	0.3051	-1.3179	0.2447	-1.2746
OCD5	-0.2953	0.2593	-0.7103	-0.3203	-0.7047
OCD6	-0.4899	0.1902	-0.6711	-0.6677	-1.0340
OCD7	-0.3242	0.2879	-0.6657	-0.6365	-1.1154
ln[K_d(340)]					
OCD1	-0.6746	0.1947	-0.7221	-0.2158	-0.6928
OCD2	-0.8730	0.2088	-1.2149	-0.0134	-1.5260
OCD3	-0.4912	0.3369	-0.9705	0.7341	-2.7229
OCD4	-0.6572	0.2988	-0.1402	0.4399	-0.9804
OCD5	-0.6413	0.2890	-0.7820	-0.1532	-0.5271
OCD6	-0.7158	0.2082	-0.7492	-0.5438	-0.8674
OCD7	-0.6465	0.2549	-0.6947	-0.6968	-0.9075

Table S 2.5: Parameters for retrieval of ln[$K_d(\lambda)$] (λ = 380 and 412 nm) from the PC scores in reparameterized original Sea*UV*.

	α	β	γ	δ	ε
ln[K_d(380)]					
OCD1	-1.2217	0.1858	-0.7745	-0.0879	-0.2971
OCD2	-1.2272	0.2098	-1.1446	0.4063	-1.3060
OCD3	-0.8579	0.2760	-0.7948	0.7782	-2.4234
OCD4	-1.1403	0.2938	-1.1530	0.8470	-0.9017
OCD5	-1.2114	0.2458	-0.7891	-0.1177	0.3527
OCD6	-1.2455	0.1809	-0.8251	-0.5554	-0.4262
OCD7	-1.2534	0.2360	-0.6872	-0.6994	-0.4918
ln[K_d(412)]					
OCD1	-1.7876	0.0866	-0.6636	0.0985	0.3059
OCD2	-1.4196	0.2304	-1.1086	0.6681	-0.8136
OCD3	-1.1186	0.2532	-0.7298	0.5602	-1.5218
OCD4	-1.5585	0.3150	-1.2024	1.2585	-0.2797
OCD5	-1.4739	0.2170	-0.8403	-0.1140	0.6014
OCD6	-1.4788	0.2059	-0.8218	-0.4645	0.2365
OCD7	-1.5979	0.2452	-0.6370	-0.6863	0.1409

Table S 2.6: Parameters for retrieval of ln[$K_d(\lambda)$] (λ = 443 and 490 nm) from the PC scores in reparameterized original Sea*UV*.

	α	β	γ	δ	ε
ln[K_d(443)]					
OCD1	-2.2066	0.0156	-0.5784	0.1859	0.9119
OCD2	-1.6014	0.2229	-1.0648	0.8079	-0.4814
OCD3	-1.3676	0.2321	-0.7068	0.5759	-1.1212
OCD4	-2.1060	0.3407	-1.3342	1.5197	0.1379
OCD5	-1.8612	0.2556	-0.8031	-0.2636	0.8703
OCD6	-1.6684	0.2229	-0.7812	-0.3578	0.6685
OCD7	-1.8911	0.2447	-0.5521	-0.6241	0.6845
ln[K_d(490)]					
OCD1	-2.9844	-0.1219	-0.4842	0.0640	2.2329
OCD2	-2.0572	0.1255	-1.0791	1.1181	-0.4627
OCD3	-1.9996	0.1680	-0.8.64	0.4028	-0.8511
OCD4	-2.3101	0.3096	-1.2606	1.5211	-0.0667
OCD5	-2.1861	0.2000	-0.6518	-0.2999	1.3206
OCD6	-1.9753	0.2339	-0.7334	-0.1401	0.7013
OCD7	-2.3296	0.2713	-0.4165	-0.4974	0.8936

Fitting parameters for inshore-water optimized Sea*UV*/Sea*UVc* algorithms:

Table S 2.7: Mean and standard deviations to center and standardize ln(R_{rs} (λ,0^{+})) for inshore-water optimized Sea*UV*/Sea*UVc* algorithms (derived from *N* = 119).

	λ = 412	λ = 443	λ = 490	λ = 510	λ = 555	λ = 670
$\bar{R}(\lambda)$	-6.8047	-6.2909	-5.5858	-5.4039	-4.9791	-5.8109
$\sigma_R(\lambda)$	1.0950	1.0015	0.8633	0.8364	0.6710	0.5895

Table S 2.8: First four eigenvectors to use to calculate the PC scores for inshore-water optimized Sea*UV*/Sea*UVc* algorithms (derived from *N* = 119).

	λ = 412	λ = 443	λ = 490	λ = 510	λ = 555	λ = 670
e_1	-0.4072	-0.4254	-0.4301	-0.4300	-0.4271	-0.3175
e_2	-0.4035	-0.2074	-0.0739	-0.0438	0.0515	0.8855
e_3	0.5864	0.2300	-0.1026	-0.3096	-0.6211	0.3333
e_4	-0.4438	0.2288	0.5091	0.3342	-0.6139	-0.0538

Table S 2.9: Parameters for retrieval of ln(K_d(λ)) from the PC scores in inshore-water optimized Sea*UV* (derived from *N* = 119).

	α	β	γ	δ	ε
ln(K_d(320))	1.8559	0.1969	0.9903	-0.6901	0.7626
ln(K_d(340))	1.5603	0.1841	0.9034	-0.4325	0.5640
ln(K_d(380))	1.1009	0.1831	0.8973	-0.1392	0.5266
ln(K_d(412))	0.8116	0.2003	0.8309	0.2024	0.0954
ln(K_d(443))	0.5629	0.1962	0.7945	0.3406	-0.1626
ln(K_d(490))	0.1920	0.1743	0.7932	0.4087	-0.1901

Table S 2.10: Coordinates of the cluster centers corresponding to the four dark water domains defined in this study for inshore-water optimized Sea*UVc* (derived from *N* = 119).

n	X_n (PC1)	Y_n (PC2)
DWD1	-4.4836	-0.2043
DWD2	0.8671	-0.3379
DWD3	2.2617	-0.0836
DWD4	-0.0862	0.6324

Table S 2.11: Parameters for retrieval of ln[$K_d(\lambda)$] (λ = 320 and 340 nm) from the PC scores using inshore-water optimized Sea*UVc* algorithm (derived from N = 119).

	α	β	γ	δ	ε
ln[K_d(320)]					
DWD1	1.6813	0.1537	0.8013	0.1765	-0.4176
DWD2	1.9161	0.2134	1.2361	-1.0752	1.2954
DWD3	1.9194	0.1246	0.7697	-1.5190	0.6293
DWD4	1.9259	0.4115	0.9184	-0.3809	0.4606
ln[K_d(340)]					
DWD1	1.1870	0.0931	0.7546	0.4312	-0.7157
DWD2	1.5810	0.2470	1.0965	-0.7010	0.9912
DWD3	1.6333	0.1236	0.7547	-1.0086	0.4981
DWD4	1.5987	0.3839	0.8347	-0.0937	0.1138

Table S 2.12: Parameters for retrieval of ln[$K_d(\lambda)$] (λ = 380 and 412 nm) from the PC scores using inshore-water optimized Sea*UVc* algorithm (derived from N = 119).

	α	β	γ	δ	ε
ln[K_d(380)]					
DWD1	0.2522	0.0047	0.5273	0.7247	-1.0622
DWD2	1.1497	0.2126	1.0661	-0.4476	0.9243
DWD3	1.0783	0.1477	0.7622	-0.8242	0.3563
DWD4	1.1999	0.3897	0.7742	0.3241	0.2196
ln[K_d(412)]					
DWD1	0.0281	0.0550	0.3835	0.5027	-1.1103

DWD2	0.8867	0.1701	0.9254	-0.2316	0.3261
DWD3	0.8200	0.1507	0.7696	-0.1859	-0.1658
DWD4	0.9300	0.3779	0.7224	0.6709	-0.2136

Table S 2.13: Parameters for retrieval of ln[K_d(λ)] (λ = 443 and 490 nm) from the PC scores using inshore-water optimized Sea*UVc* algorithm (derived from *N* = 119).

	α	β	γ	δ	ε
ln[K_d(443)]					
DWD1	-0.3852	0.0202	0.2538	0.6002	-1.2899
DWD2	0.6433	0.1286	0.8554	-0.1522	-0.0429
DWD3	0.5321	0.1655	0.7410	-0.0221	-0.4114
DWD4	0.6953	0.4021	0.6909	0.8319	-0.4765
ln[K_d(490)]					
DWD1	-0.9983	-0.0533	0.2249	0.5128	-1.5672
DWD2	0.2955	0.0618	0.8647	-0.1419	-0.0014
DWD3	0.0834	0.1809	0.7113	-0.0268	-0.3008
DWD4	0.3143	0.4160	0.6970	1.0661	-0.6296

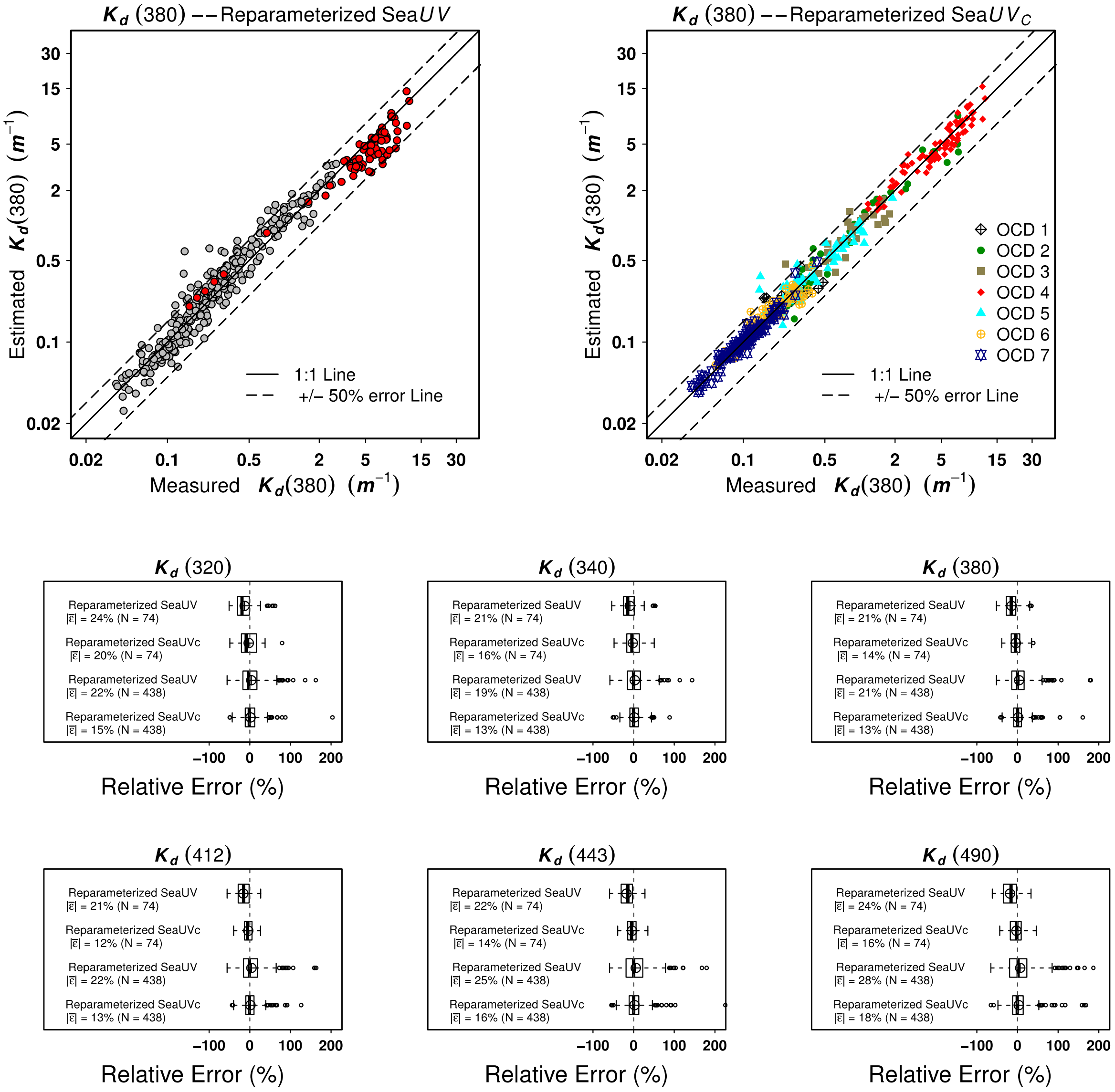

Figure S 2.1: Performances of re-parameterization of the original algorithms through retraining the complete data set (N = 438)

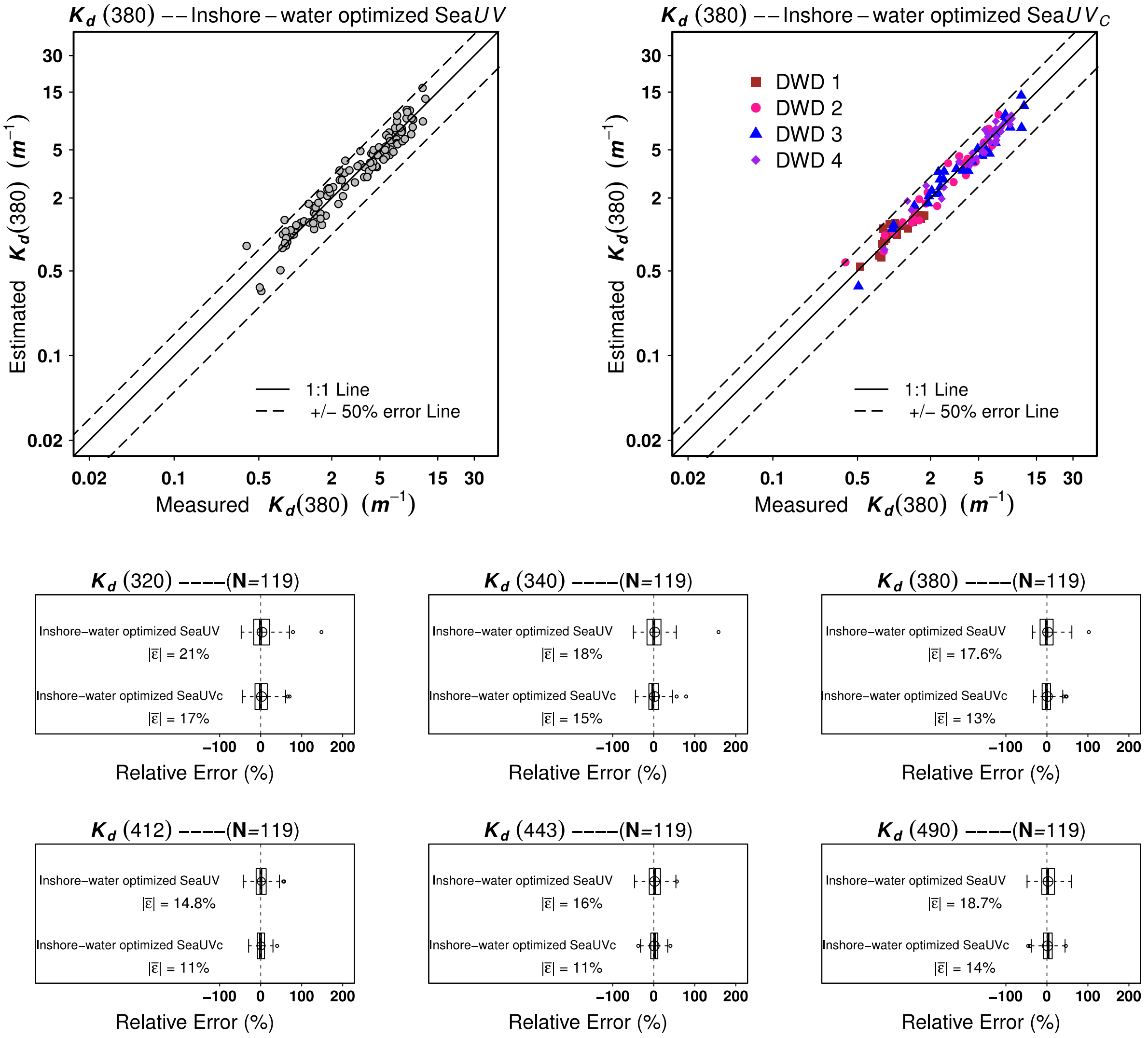

Figure S 2.2: Performances of dark-water optimized Sea*UV*/Sea*UVc* algorithms (derived from *N* = 119)

APPENDIX C

IMPLEMENTATION SCHEMES FOR SEACDOM ALGORITHM[8]

---

[8] Appendix for
Cao, F., and W. L. Miller (2014), *Journal of Geophysical Research: Oceans*, 120, 496–516, doi:10.1002/2014JC010241; Reprinted here with the permission of the publisher.

Introduction:

This appendix contains a flow chart of step-by-step implementation schemes for the SeaCDOM algorithm presented in Chapter 3. All the parameters needed for retrieving spectrally resolved CDOM spectra are provided via online resources.

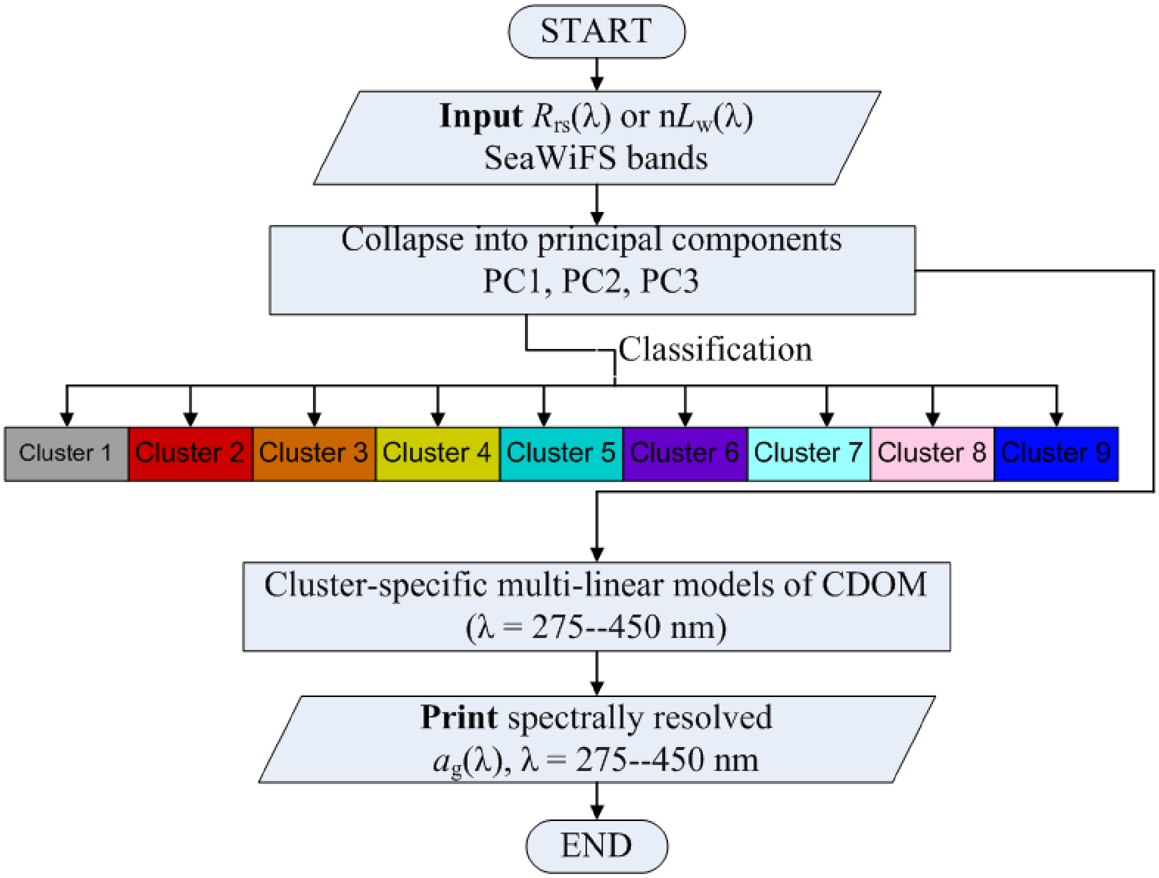

Figure C. 1: Flow chart diagram for implementation of the Sea*CDOM* algorithm.

APPENDIX D

SUPPLEMENTARY INFORMATION FOR CHAPTER 3[9]

---

[9] Online supplementary material for
Cao, F., and W. L. Miller (2014), Journal *of Geophysical Research: Oceans*, 120, 496–516, doi:10.1002/2014JC010241; Reprinted here with the permission of the publisher.

Introduction:

This appendix contains supplementary information for Chapter 3. Figure S 3.1 shows why the Sea*CDOM* algorithms failed in giving good estimates of a_g for the waters in the Gulf of Maine and the upwelling Chile area in BIOSOPE data set.

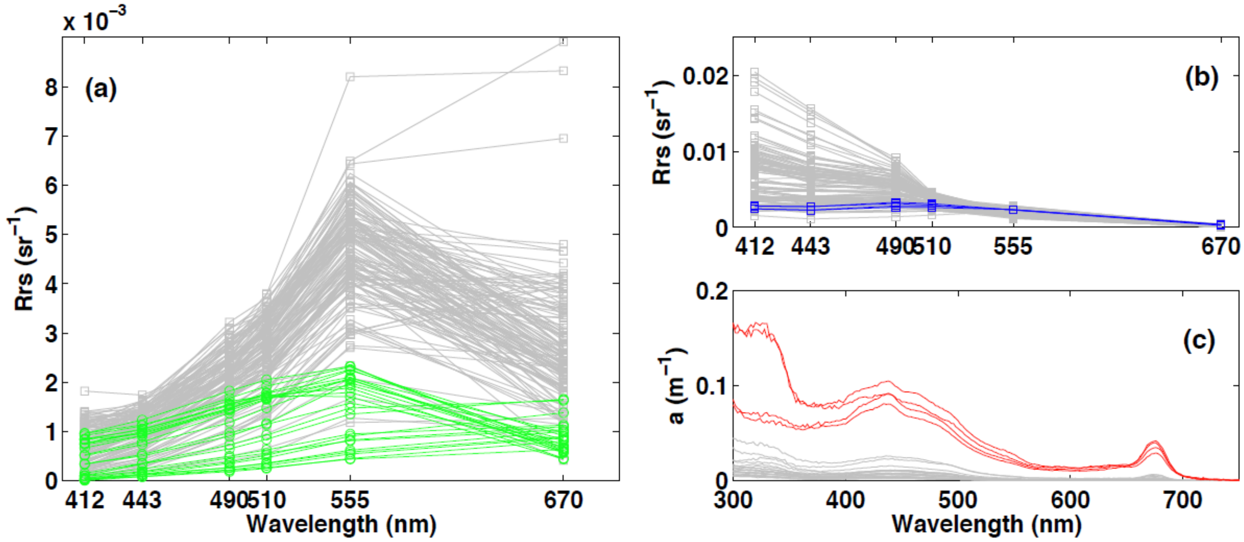

Figure S 3.1: (a) R_{rs} spectrum of cluster 4 and 5 in the training data set (grey) and R_{rs} of waters in the Gulf of Maine (green) (N = 25). Note that neither the magnitude nor the spectral shape of reflectance in the Gulf of Maine was captured by our algorithm, while performing the algorithm on this data set, the Sea*CDOM* mistakenly classified them into clusters 4 and 5 defined by the training exercise. (b) R_{rs} spectrum for clusters 8 and 9 in the training data set (grey) and the four outlier samples (blue) in the BIOSOPE data set collected from the Peru-Chile upwelling zone. Note that our algorithm succeeds in capturing the spectral shape and magnitude of R_r in this first step. (c) Absorption coefficients of particles in the BIOSOPE data set. Note that the four outlier samples (red) that collected from upwelling area are considerably higher than those sampled from more offshore region (gray) which were associated with good a_g estimates.